Anti-Icing Coatings Manufactured by Cold Gas Dynamic Spray and Icephobic Performance Evaluation

uOttawa

by

Zachary Leclerc

Thesis submitted to the Department of Mechanical Engineering in partial fulfillment of the requirements for the degree of

MASTER OF APPLIED SCIENCE

Faculty of Engineering - Department of Mechanical Engineering

University of Ottawa

Ottawa, Ontario, Canada

February 2023

Abstract

Ice accumulation is a recurring issue in various industries exposed to atmospheric icing, often causing severe damage, disruptions of continuous operation and substantial efficiency losses. Current mitigation methods require complex engineering considerations and intensive energy requirements. Alternative solutions are being explored, including ice release coatings (icephobic coatings) which use their surface and chemical properties to protect a structure from ice accretion. Several materials are naturally icephobic in a bulk material state however, to be useful in real-world applications, they are required to be in coating form. Current processes used to apply these materials as coatings can deter icephobic properties if not executed properly. Cold gas dynamic spray (CS), a green additive manufacturing method, is considered as an alternative process as it does not melt its feedstock material, thus preserving initial material properties. Two icephobic materials are investigated in this work, including their CS deposition and icephobic performance.

Firstly, studies focusing on the cold spray deposition of polymers remains poorly understood and inefficiently executed in the field. The use of a supersonic flow produced by commercial CS nozzles remains the standard and often include complex nozzle alterations to accommodate the polymer feedstock. As a result, this work presents a new nozzle, designed using numerical simulations, and experimental results are used to characterize its deposition behavior. The new nozzle demonstrates that CS can efficiently produce polymer coatings on metallic substrates without the use of a complex flow and using commercially available components. The icephobic performance of coatings produced with the new nozzle are then characterized using the three components that make up atmospheric icing: the ability to 1) shed water droplets through hydrophobicity, 2) delay the ice nucleation and growth process, and 3) reduce overall ice adhesion properties. The as-sprayed polymer coating demonstrated a superhydrophobic behavior at room temperature, however its beneficial complex surface hierarchy led to degrading icephobicity at low temperatures. Under various frosting conditions, the coating's wetting state became compromised prior to solidification, which demonstrated that other studies claiming superhydrophobic surfaces can also be icephobic are in fact incomplete.

Secondly, literature has shown that bulk complex metallic alloys, such as quasicrystals (QC), have unique icephobic properties, in addition to being very durable materials. However, the intrinsic brittleness and hardness of these materials render their application as a coating very challenging. The use of the CS process for this material is especially difficult as it relies heavily on plastic deformation for the bonding of particles with the substrate. This work investigates the deposition of QCs through process parameter mapping, intensive particle pre-heating to thermally soften the feedstock, and through the addition of a softer metallic phase for the creation of a ceramic-metal matrix composite (cermet) coating. The work shows that QCs require further investigation if they are to be cold sprayed without the use of feedstock pre-heating. However, when subjected to intensive pre-heating, they have shown to be a promising first step in the deposition of full QC coatings. In addition, their use as the ceramic phase in a cermet coating has shown to be a successful alternative, despite having minor retention of the QC phase in the final coating.

Acknowledgements

Firstly, I would like to thank my thesis supervisor, Professor Bertrand Jodoin, for always pushing me to dig deeper and allowing me to reach levels I never thought I would. It has been an honor to learn and work alongside him throughout the past few years.

I would also like to thank all the technicians working at the University of Ottawa machine shop including Stan, Jaques, James and especially Paul for their help in bringing to life all the various experiments used in this work. I am also very grateful and appreciative of all the help, guidance and support I received from Leo. He has played an enormous role in the creation of my climatic ice adhesion test chamber, and in all the troubleshooting steps that came with it.

Thank you to all the members of the University of Ottawa Cold Spray Laboratory including Daniel MacDonald, Aleksandra Nastic, Leon Guo, Maryam Razavipour and Roberto Fernandez for showing me the ropes at the lab and for all the advice given along the way.

I also wish to thank my friends and family for their love and support throughout this journey. Lastly, I want to thank Micaela for all her love and encouragement without whom this would not have been possible.

Table of Contents

ABSTRACT ..... **II**

ACKNOWLEDGEMENTS ..... **IV**

LIST OF FIGURES ..... **VII**

LIST OF TABLES ..... **X**

1 INTRODUCTION **1**

1.1 BACKGROUND 1
1.2 RESEARCH OBJECTIVES 3
1.3 THESIS OUTLINE 3

2 LITERATURE REVIEW **5**

2.1 ATMOSPHERIC ICING 5
2.1.1 Characterization of the Icing Environment *5*
2.1.2 Ice Nucleation Mechanisms *8*
2.2 ICEPHOBICITY 9
2.2.1 Hydrophobic Behavior *10*
2.2.2 Ice Nucleation Development *13*
2.2.3 Ice Adhesion Characteristics *14*
2.3 ICE MITIGATION SYSTEMS 15
2.3.1 De-Icing Systems *16*
2.3.2 Anti-Icing Systems *20*
2.3.3 Hybrid Systems *23*
2.4 THERMAL SPRAYING 24
2.4.1 Flame Spray *25*
2.4.2 Plasma Spray *26*
2.4.3 High Velocity Oxygen Fuel Spray *27*
2.4.4 Cold Gas Dynamic Spray *28*
2.5 QUASICRYSTALS 29
2.5.1 Properties *30*
2.5.2 Production of QC Powders *31*
2.5.3 Cold Spray of QC and Ceramic Deposition *32*
2.6 ICE ADHESION TESTING METHODS 33
2.6.1 Centrifuge Adhesion Test *33*
2.6.2 Calculated Centrifuge Adhesion Test *34*
2.6.3 Instrumented Centrifuge Adhesion Test *37*
2.6.4 Pusher Test *38*
2.6.5 Shear Test *39*

3 RESEARCH OBJECTIVES **42**

3.1 GENERAL OBJECTIVES 42
3.2 NOZZLE DESIGN FOR POLYMER COLD SPRAY 42
3.3 PRODUCTION OF POLYMER COATING ON METALLIC SUBSTRATE 43
3.4 HYDROPHOBIC PERFORMANCE OF POLYMER COATING 43
3.5 ICE NUCLEATION AND GROWTH CHARACTERIZATION OF POLYMER COATING 43

3.6 ICE ADHESION BEHAVIOR OF POLYMER COATING 44
3.7 PRODUCTION OF ALUMINUM-RICH QUASICRYSTAL COATINGS 44

4 EXPERIMENTAL PROCEDURES 45

4.1 POWDER MATERIALS AND SUBSTRATES 45
4.2 COLD SPRAY SYSTEM 47
4.2.1 Gas Heater and Control Unit 47
4.2.2 Powder Pre-heater 47
4.2.3 Nozzle Assemblies 50
4.2.4 Robotic Traverse System 53
4.2.5 Powder Feeding Equipment 54
4.2.6 Spray Chamber 54
4.2.7 Strip Heater 55
4.3 CHARACTERIZATION PROCEDURES AND ANALYSIS EQUIPMENT 56
4.3.1 Sample Post-Processing 56
4.3.2 Scanning Electron and Optical Microscope 56
4.3.3 Surface Roughness Measurements 57
4.3.4 Goniometer System 57
4.3.5 Ice Growth and Droplet Pusher System 58
4.3.6 Climatic Ice Adhesion Test Chamber 60

5 RESULTS 71

5.1 POLYMER SOLUTION 71
5.2 METALLIC SOLUTION 130
5.2.1 Parameter Matrix 130
5.2.2 Powder Pre-Heating 133
5.2.3 Cermet Deposition 138

6 CONCLUSIONS AND FUTURE WORK 142

6.1 CONCLUSIONS 142
6.2 FUTURE WORK 144

REFERENCES 146

APPENDIX – A 155

APPENDIX – B 156

List of Figures

Figure 1. Three stages of the icing process [8], [15] 1
Figure 2. Rime ice*: air bubble formation (*left*)*, visible accumulation only on leading edge of airfoil (right) [2], [55] 7
Figure 3. Glaze and mixed ice formation (left), mixed ice formation showing ice accretion along top and bottom of airfoil (middle), and complex glaze ice structure displaying vertical ice growth (right) [54], [55] 7
Figure 4. Atmospheric ice types based on altitude [4] 8
Figure 5. Icephobic surface characteristics such as liquid extent (wet or dry surface), topography (rough or smooth surface), and elasticity (soft or hard surface) [57] 10
Figure 6. Wetting behavior based on water contact angles [58] 10
Figure 7. Contact angle hysteresis [59] 11
Figure 8. Roll-off angle [4] 11
Figure 9. Cassie-Baxter and Wenzel wetting states [57] 12
Figure 10. Wenzel ice infiltrating surface asperities [57] 12
Figure 11. Cassie ice remaining above surface asperities [57] 12
Figure 12. Molecular view of water prior to the initiation of ice nucleation [8] 13
Figure 13. Molecular view of ice once ice nucleation has completed [8] 13
Figure 14. ADIS categories based on general function, system operation, mitigation mechanism, and surface/material property [63] 16
Figure 15. Inflatable boot system [64] 17
Figure 16. EIDI system [6] 18
Figure 17. EESS system [6] 19
Figure 18. Heating panel examples: carbon filament (left), woven carbon fabric (right) [65] 20
Figure 19. Microwave heating system [5] 21
Figure 20. SLIPS system [4] 22
Figure 21. Hot air injection system for wind turbine blade. Hot air is distributed throughout the inner blade structure to heat blade and melt accreted ice on the outside of the blade [66] 23
Figure 22. Gas temperature and velocity for different thermal spray processes [73] 25
Figure 23. Flame Spraying equipment: (1) gases inlet (fuel and oxygen); (2) powder inlet; (3) torch; (4) sprayed coating; (5) particle stream; (6) combustion flame [71] 26
Figure 24. Plasma spraying schematic [75] 27
Figure 25. Axial powder injection in HVOF spray gun [73] 27
Figure 26. Cold Gas Dynamic Spray System [48] 29
Figure 27. Icosahedral structure, using selected area electron diffraction. Taken along a) 5-fold symmetry axis; b) 3-fold symmetry axis and c) 2-fold symmetry axis; d) all three types of symmetry axes found in the icosahedral structure [80] 30
Figure 28. CAT configuration [89] 34
Figure 29. CCAT model [90] 35
Figure 30. AERTS system [88] 38

Figure 31. Rotor Force Transducer [88] 38
Figure 32. Pusher Test [92] 39
Figure 33. Rotational ST; cylindrical (left) and annular (right) [88] 40
Figure 34. Lap-Joint ST 40
Figure 35. 0° cone test [16] 41
Figure 36. Power morphology of a) Perfluoroalkoxy alkane, b) Aluminum, and c) Quasicrystal 46
Figure 37. SST control cabinet (left) and gas heater (right) 47
Figure 38. Powder preheating coil (left), system schematic in reference to cold spray nozzle (right) 48
Figure 39. Steel nozzle 51
Figure 40. New nozzle design 51
Figure 41. New nozzle powder injection assembly 52
Figure 42. Tungsten carbide nozzle 53
Figure 43. Robotic traverse system 53
Figure 44. Powder feeding canister (left) and feeding wheel (right) 54
Figure 45. Cold spraying chamber 55
Figure 46. Strip heater beneath (top) and conducting side (bottom) 55
Figure 47. Sample cutting machine 56
Figure 48. Sample polishing machine 56
Figure 49. Scanning electron microscope 57
Figure 50. Optical microscope 57
Figure 51, Goniometer system for sessile drop method 58
Figure 52. Cryostage experimental equipment 59
Figure 53. Droplet pusher: a) Overall assembly, b) Push rod and load cell image, and c) System schematic 60
Figure 54. Mounted rotor for CAT 61
Figure 55. Ice production assembly 62
Figure 56. Ice cube dimensions 62
Figure 57. Mounting brackets for chest freezer 63
Figure 58. Securing straps for chest freezer 63
Figure 59. Wooden lid asssembly of CIATC 64
Figure 60. Access door temperature sensor 65
Figure 61. Controlling thermocouple 65
Figure 62. Vibration sensor mounted on the flanged bearing unit 66
Figure 63. Emergency stop button 67
Figure 64. Magnetic safety for CAT 67
Figure 65. Motor and belt guard with access door open (left) and closed (right) 68
Figure 66. Steel plating inside CAT assembly 68
Figure 67. Electric motor and adjustable motor base for belt tensioning 69
Figure 68. Variable frequency drive unit 69
Figure 69. Arduino control board for CAT 70
Figure 70. Power source for vibration sensor 70

Figure 71. Deposition of room-temperature QC feedstock at 500 °C and 3450 kPa on aluminum (1) and stainless-steel (2) substrates at 250X (a) and 1000X (b) magnification 132
Figure 72. Cross-sectional view of deposited QC feedstock at 500 °C and 3450 kPa on aluminum (1) and stainless-steel (2) substrates, with feedstock preheated to 600 °C (a) and 700 °C (b) 136
Figure 73. Aluminum substrate top view (a) edge of spray path, (b) magnified view of multiple craters 137
Figure 74. Overview of single particle indentation, showing jetting of the stainless-steel substrate 138
Figure 75. Cross-sectional view of QC-Al cermet coatings with (a) 90 wt.% QC and (b) 75 wt.% QC (red arrow represents substrate-coating interface) 141

List of Tables

Table 1. Icosahedral QC properties compared to other materials 31
Table 2. Alloying elements of QC powder Cristome A1 45
Table 3. Spray parameter matrix for QC feedstock 130
Table 4. Constant spray parameters for QC feedstock 131
Table 5. Powder pre-heating temperatures (T) in [°C], and feed rate (FR) in standard cubic feet per hour [SCFH] 134
Table 6. Constant spray parameters for pre-heated QC feedstock 134
Table 7. Spray parameters for cermet QC-Al feedstock 139

1 INTRODUCTION

1.1 Background

The accumulation of atmospheric ice can cause many disruptions, such as flow separation over aircraft wings and subsequent loss of lift [1], overweighing power networks leading to large scale outages [2], and unbalance wind turbine blades causing complete system shutdowns and resulting in long term energy losses [3], to name a few. Ice accretion is currently mitigated by active de-icing and anti-icing systems such as electro-expulsion, inflatable boots, electrical heating, ultrasound debonding, shape memory alloys, hot air injection, and others [4]–[7]. Despite their effectiveness, the use of these systems greatly depends on the accurate detection of ice during operation, using complex sensory systems, and most methods also require large amounts of energy to function [7]. Passive ice removal methods however, such as icephobic coatings, offer a more sustainable solution to atmospheric icing. Passive solutions do not require any external energy to function and rely exclusively on the material's physical and chemical properties to minimize ice accumulation by encouraging natural ice shedding. An icephobic surface, as illustrated schematically in Figure 1, can address a single stage in the icing process or multiples stages at once, such as preventing impacting supercooled water droplets from freezing, slowing down the ice nucleation process to delay solidification, and reducing the overall ice adhesion [4], [8]–[14].

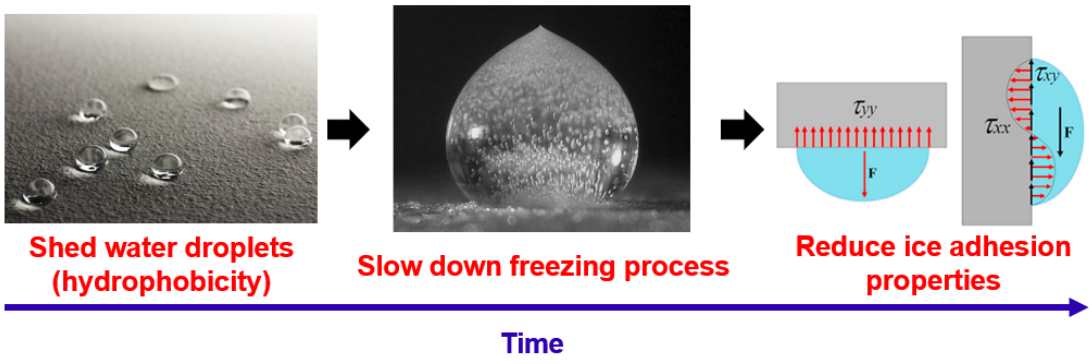

Figure 1. Three stages of the icing process [8], [15]

Various materials can be used as icephobic surfaces, although certain material properties are typically sought. Materials exhibiting low surface energy are often considered for icephobic surfaces because of their non-stick properties [8], [9], [16], [17]. Current icephobic materials include various elastomers [18]–[20], low energy polymers [21]–[26], complex metallic alloys such as QCs [17], [27], and multiple oil/polymer-matrix combinations used as slippery liquid infused porous surfaces (SLIPS) [14], [28]–[35].

Depositing polymer-based coatings on metallic surfaces has commonly been done using conventional methods like dipping or electrostatic spraying, however thermal spray (TS) has increasingly been used [36]–[41]. TS is also being used to produce metal-based icephobic coatings as it encompasses many established metallic coating manufacturing methods [17], [27], [42]–[47], one of which is CS.

The CS process offers many advantages as opposed to other TS methods, such as its solid-state feedstock deposition and portability for easy field repairs. CS uses compressed inert gases (nitrogen or helium) to accelerate feedstock powder through a De Laval nozzle up to supersonic velocities [48]. Unlike other TS processes, the processing temperatures used in CS are much lower than the melting temperature of the feedstock powder, thus preserving initial material properties [48], [49]. This can largely influence final coating properties, especially when low melting point materials (polymers) or materials with temperature sensitive crystalline structures are being deposited. Despite the many advantages, the CS process is not yet established in depositing polymer feedstock on metallic substrates or in the deposition of complex metallic alloys like QCs. Namely, the converging-diverging nozzle design geometry currently used in commercial CS systems was not conceived for soft and low melting point materials. The current nozzle geometry uses gas dynamics to accelerate feedstock to high velocities and keeps processing temperatures low, however further investigation is required to determine if this is also beneficial to polymer feedstock due to potential differences in particle bonding mechanisms. Moreover, the deposition of QC materials has yet to be investigated as a sole-material coating using CS [50], [51]. The deposition of very hard and brittle materials with CS has been investigated in the past; however, limited work exists on the deposition of complex metallic alloys for icephobic applications.

1.2 Research Objectives

This work aims at investigating two icephobic solutions, a polymer and metallic solution, using the CS process. The goal is to produce a thin and dense coating capable of a) repelling water droplets, b) delaying ice nucleation and solidification, and c) reducing overall ice adhesion for its practical application on surfaces exposed to atmospheric icing. To achieve this goal, the following steps were taken:

1. The cold spray nozzle geometry and powder injection were redesigned to accommodate polymer feedstock
2. Polymer coatings were manufactured using CS with the new nozzle design for deposition onto metallic substrates
3. The hydrophobic performance of the as-deposited coating was assessed for its water repelling abilities and compared to other materials
4. The ice nucleation and growth of water droplets on the as-deposited coating was assessed and compared to other materials
5. The ice adhesion of large surfaces and single droplets was assessed for the as-deposited coating and compared to other materials
6. The CS deposition of QC feedstock material was explored using an array of processing parameters, elevated powder pre-heating, and by introducing a ductile phase to create a ceramic metal matrix composite coating

1.3 Thesis Outline

The thesis is organized in 6 chapters. Chapter 1 consists of an introduction to the research question along with a brief overview of the methodology employed to achieve the research goals.

Chapter 2 provides an updated summary of the supporting literature relevant to this study. Firstly, atmospheric icing is characterized by the various ice types that can form in the atmosphere, followed by the ice nucleation mechanisms causing the solidification of the ice. Secondly, icephobicity is broken down into three phases of protection against the accretion of ice. Thirdly, a brief overview of the current ice mitigation systems is provided. Fourthly, several thermal spraying methods are summarized along with cold gas dynamic spray. Fifthly, quasicrystalline materials are defined as a function of their material

properties, powder manufacturing methods, and ability to be cold sprayed. Lastly, various testing methods used in laboratories are explored to assess a surface's ice adhesion properties.

Chapter 3 defines the individual research objectives of this work, along with the in-depth methodology used to accomplish each step.

Chapter 4 lists the experimental equipment used and explains their purpose in the research. The list includes processing materials, cold spray system equipment, and sample characterization equipment.

Chapter 5 presents the results and discussions of both icephobic coating solutions, namely the manufacturing of polymer coatings and its icephobic properties, and the production of quasicrystalline coatings using cold spray.

The final chapter of the thesis summarizes the conclusions of both icephobic coating solutions and proposes recommendations for any future work. The following sections include the complete reference list and appendices.

2 LITERATURE REVIEW

2.1 Atmospheric Icing

Ice formation in atmospheric environments is dependant on many conditions such as altitude, surface temperature, impact velocity and ambient conditions [52]. Ice accretion occurs when precipitation in the form of freezing rain, snow or supercooled water droplets, impacts a cold surface repeatedly [9]. Environmental conditions, as listed above, dictate the properties and geometry of the ice accreted on aircrafts and wind turbines. Understanding the icing conditions and nucleation mechanisms allows for proper mitigation methods to be developed.

2.1.1 Characterization of the Icing Environment

All forms of precipitation can create some form of ice accretion, but high velocity impacting supercooled water droplets are considered the most critical form [9]. At high altitude, supercooled water droplets are found in cloud formations. As such, the droplets can impact moving aerodynamic surfaces such as aircraft wings, wind turbine blades or helicopter rotors [4]. Natural icing cloud formations have a wide range of droplet sizes, although for testing and identifying icing severity, the mean volume diameter (MVD) is often used to simplify models [53]. Typical supercooled water droplets have a MVD of 50 microns, however larger supercooled droplets (SLD), in the order of 250 microns, can also be present in cloud formations [54]. For aircrafts moving through cloud formations, containing supercooled water droplets, ice begins by forming on geometries perpendicular to the air flow and accumulation occurs in two ways; instant freezing or partial freezing [54]. Instant freezing is when the droplets freeze immediately upon impact, whereas partial freezing is when part of the droplet freezes and the rest runs back along the surface until it freezes completely [54]. Upon droplet impact, the latent heat of fusion is released from the liquid, which allows it to freeze, and in turn this warms the underlying surface [54]. The surface being warmed is then cooled due to the convective heat transfer from the passing air [54]. This can be explained with the principle of liquid water content (LWC), which is a major factor in determining if water droplets will freeze upon impact or not. LWC is defined as the amount of liquid water present in a cloud and is represented by grams of water per cubic meter of cloud. When temperatures are slightly below freezing and there

are more liquid water droplets than frozen droplets, LWC is high. When temperatures are very cold, LWC is low because there are mostly ice particles in the cloud.

For temperatures well below freezing, or low LWC, there is a balance between the latent heat release and the convective heat transfer of the passing air, therefore the droplets would freeze immediately on impact [54]. On the other hand, with high LWC, or temperatures slightly below freezing, there is too much latent heat being released and not enough being transferred by convection [54]. This allows the droplet to remain partially liquid and trail along the surface until the heat transfer balance leads to freezing the droplet [54]. An increasing concern has grown with the accretion of SLD's, because even with a low LWC, for large size droplets the same imbalance of heat transfer causes partial freezing on the surface [54]. These two types of droplet-freezing methods tend to create very different ice shapes and microstructures, known as rime ice and glaze ice.

2.1.1.1 Rime Ice

When the freezing fraction, or the percentage of the impacting droplet that froze upon impact, is equal to one, rime ice will form [54]. Rime ice is more common in upper atmospheric icing conditions, as such, LWC and temperature are low and instant freezing occurs [54]. As illustrated on the left image of Figure 2, during the instant freezing of droplets, very small air bubbles will form which causes rime ice to have an opaque and milky appearance [54]. Shown on the right image of Figure 2, the accumulation of rime ice is contained to leading edges of blades and airfoils since droplets freeze instantly, as a result the ice geometry tends to be very simple and remains in a single area [54].

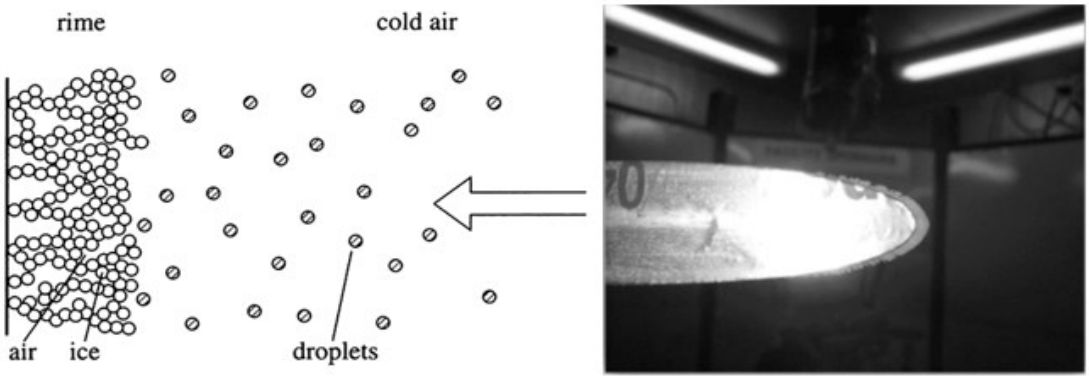

Figure 2. Rime ice*: air bubble formation (*left*)*, visible accumulation only on leading edge of airfoil (right) [2], [55]

2.1.1.2 Glaze Ice

The second ice type forms when the freezing fraction is below one, which means partial freezing occurred [54]. Glaze ice is commonly found in high LWC clouds and at lower altitudes. Ice accumulation in the shape of horns are not uncommon for glaze ice, as seen in Figure 3, meaning there is potential for vertical ice accumulation which can cause severe flow disruption [54].

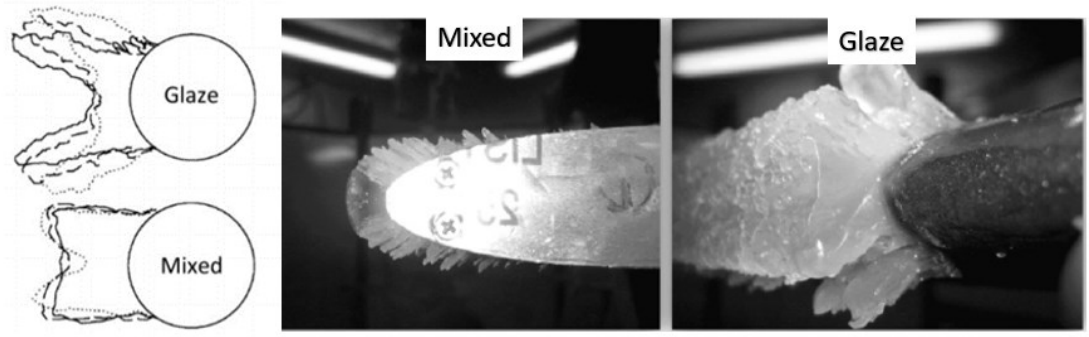

Figure 3. Glaze and mixed ice formation (left), mixed ice formation showing ice accretion along top and bottom of airfoil (middle), and complex glaze ice structure displaying vertical ice growth (right) [54], [55]

Since the liquid part of partially frozen droplets run along trailing surfaces, odd geometries tend to form and become a threat to the delicate aerodynamics of blades, wings and rotors. Glaze ice is usually very transparent, as no air bubbles are trapped, meaning it is usually denser and has more area in contact with the surface. For those reasons, the mechanical strength of glaze ice is much stronger than rime ice making it more difficult to remove during operation [54]. Therefore, there is a greater risk when operating aircrafts at lower

altitudes since glaze icing conditions will prevail [4]. There is also the possibility of having a mix of both ice types, although a purely glaze ice is considered to be a larger threat and is the focus most ice adhesion studies [54]. As seen Figure 4, an approximation of the scale for the temperatures and altitudes are demonstrated in relation to glaze and rime icing conditions [54].

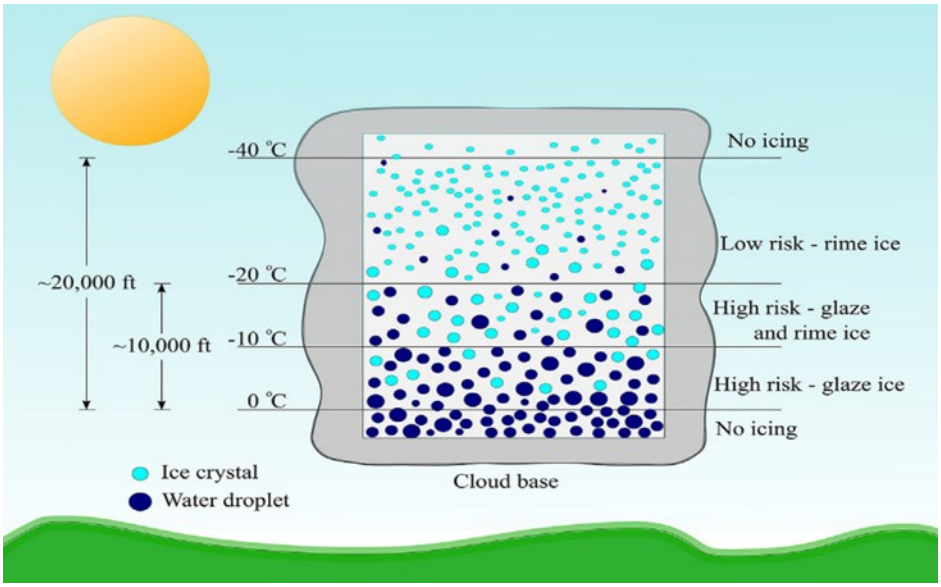

Figure 4. Atmospheric ice types based on altitude [4]

2.1.2 Ice Nucleation Mechanisms

The solidification of supercooled droplets occurs at the molecular scale and therefore can be a challenge in determining if the process has begun [9]. The nucleation of ice can usually be observed visually by a change in clarity within the droplet, which indicates the phase change [9]. Freezing of supercooled water droplets in icing clouds can occur with two types of nucleation mechanisms; heterogeneous and homogeneous nucleation [9]. Homogenous nucleation is very arbitrary in nuclei locations, since it occurs primarily in water without impurities or foreign nucleation sites [9]. A foreign nucleation site is defined as either a surface contacting the droplet or an impurity in the air. For this reason, homogeneous nucleation occurs very rapidly and at very cold temperatures because of the purity of the supercooled water droplets, and since there is no foreign influence on the droplet [9]. Contrarily, heterogeneous ice nucleation occurs when a nucleation site presents itself due to impurities in the water or because of foreign morphology acting on the droplet such as

a surface [9]. In other words, heterogeneous nucleation prevails when supercooled droplets contact aircraft wings, turbines blades, vehicle windshields or any other cold surface [9].

It is concluded that nucleation works as a function of surface roughness, as such, surface topography can act as seeding locations and promote heterogeneous nucleation sites on the droplets surface [9]. In the case of aircraft wings, turbine blades or helicopter rotors, heterogeneous ice nucleation is the greatest concern for ice formation and accretion. Furthermore, there are four main parameters influencing heterogeneous ice nucleation; the purity of the water, ambient/substrate temperature, the surface roughness acting on the supercooled droplet and the free energy barrier with the surface [56]. Since water purity and temperature aren't controllable factors, the governing factors for heterogeneous ice nucleation are surface roughness and the free energy barrier of the surface in contact [56].

2.2 Icephobicity

A clear definition over which characteristics a surface must possess in order to be labelled icephobic, also called pagophobic (*pagos* meaning ice in Greek), has been a debate for quite some time [57]. Anti-icing surfaces, otherwise called icephobic surfaces, should display three functional aspects; minimizing surface wetting from water droplets, delaying ice nucleation in wet/humid environments, and reducing ice adhesion [8]. These three aspects can also be labelled as the lines of defense a coating should have in order to protect the surface [8]. Attempts at resolving each line of defense has led to very different solutions to anti-icing such as micro-textured superhydrophobic surfaces, slippery liquid infused surfaces, as well as smooth low surface energy surfaces [8]. As seen in Figure 5, there exists many characteristics in which pagophobic surfaces can be classified such as surface topography, liquid extent, surface elasticity, and others [57]. The following sub-sections will discuss each solution in reference to which role it plays in the lines of defense of an icephobic surface.

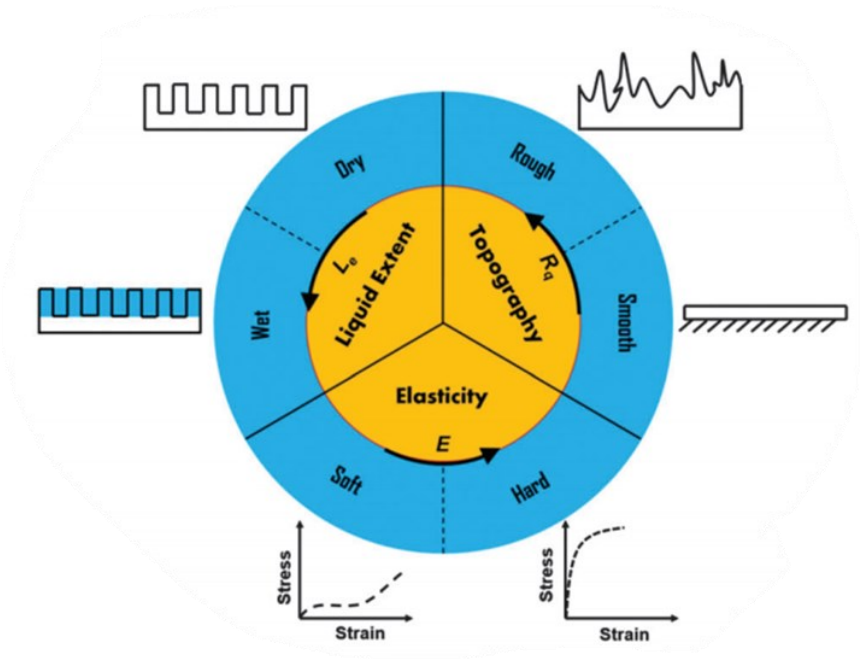

Figure 5. Icephobic surface characteristics such as liquid extent (wet or dry surface), topography (rough or smooth surface), and elasticity (soft or hard surface) [57]

2.2.1 Hydrophobic Behavior

Initial research of icephobic surfaces began with using superhydrophobic surfaces in icing conditions. The hypothesis was that since water and ice have such similar surface tension/energy, the superhydrophobic properties seen with water may also prevent the adhesion of ice [4]. Classification of hydrophobic surfaces use the concept of static contact angle (SCA). A seen in Figure 6, the SCA is the angle made by the surface and the tangent of the water droplet [4]. Surfaces can be divided in three classes; hydrophilic (SCA < 90°), hydrophobic (90° < SCA < 150°), and superhydrophobic (SCA > 150°) [4]. .

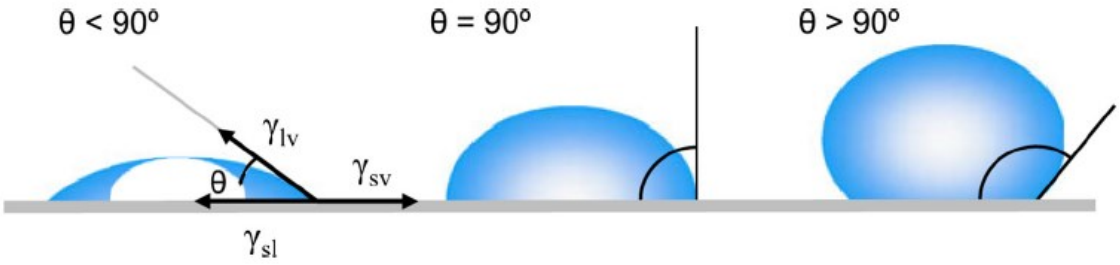

Figure 6. Wetting behavior based on water contact angles [58]

The SCA can be calculated with the surface free energies of a surface, as the Young's equation demonstrates

$$\gamma_{sl} + \gamma_{lv}\cos(SCA) = \gamma_{sv} \quad (1)$$

where γ_{sl}, γ_{lv} and γ_{sv} are the surface free energies of the solid/liquid, liquid/vapour and solid/vapour states [8]. The Young's equation is an idealized model for flat surfaces which is not representative of surfaces with a given roughness. Therefore, the apparent contact angle (ACA) gives a more accurate result since it introduces a surface roughness factor, as the following equation demonstrates

$$\cos(ACA) = r * \cos(SCA) \quad (2)$$

where *r* is the surface roughness factor given by

$$\mathrm{r} = \frac{\frac{solid}{liquid}\, contact\ area}{nominal\ interface\ contact\ area} \geq 1 \quad (3)$$

In aerospace or high speed applications, the ACA does not provide as useful information as the contact angle hysterisis (CAH) [4]. The CAH, as seen in Figure 7, is the difference between the advancing CA and the recending CA when a droplet is in movement [4]. Superhydrophobic surfaces typically have CAH < 10° [4]. Since calculating a CAH from an impacting water droplet is very difficult, the roll-off angle (ROA) is used in conjunction with the CAH. The ROA is the minimum angle a surface needs to be inclined in order for the droplet to roll-off, as seen in Figure 8. Such values are used to characterize hydrophobicity, in place of ACA, because of the relevancy of angled surfaces in real world applications.

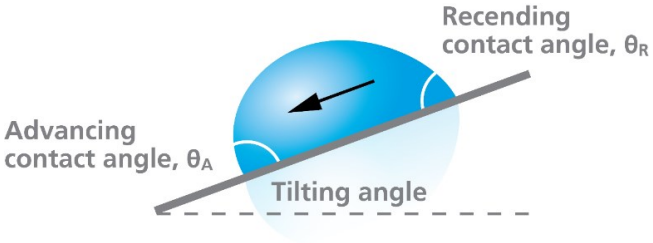

Figure 7. Contact angle hysteresis [59]

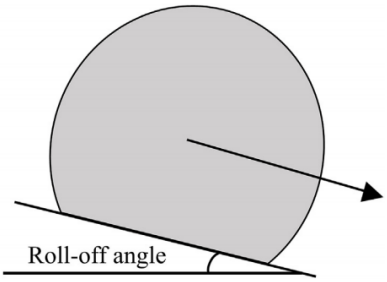

Figure 8. Roll-off angle [4]

Superhydrophobic surfaces have been inspired by nature's designs, more specifically the Lotus plant leaves [57]. The Lotus effect, more commonly known as the Cassie or Cassie-

Baxter state, is when a liquid layer or droplet is suspended on a surface due to micro-textures with entrapped air passages [57]. A seen in Figure 9, this state can result in droplets to be suspended on the surface due to surface tension, thus avoiding wetting the surface [57].

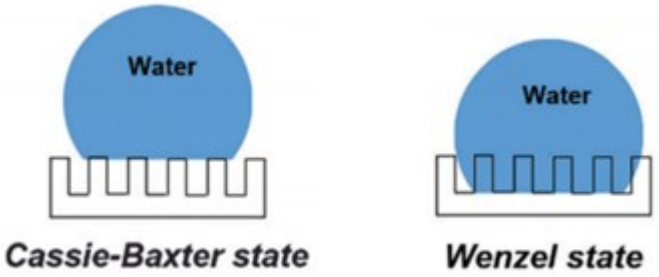

Figure 9. Cassie-Baxter and Wenzel wetting states [57]

Also seen in Figure 9, exists the Wenzel state caused by the same micro-textures on the surface [57]. The Wenzel state occurs when the liquid droplets displace the entrapped air and causes the substrate to be in a fully wetted state [57]. In aerospace applications, where high-speed impacts with water droplets occur, the air within the micro-textures no longer support the droplets and superhydrophobicity is lost. Contrarily, if the surface is being iced in a static form, then the Cassie-Baxter state can remain intact, meaning the surface does prevent ice formation [60]. With practical applications in mind, such as aircrafts or helicopters, superhydrophobicity can often be lost which can cause induced Wenzel ice formation [57]. As demonstrated in Figure 10 and Figure 11, due to the increased contact area between the surface and ice, Wenzel ice causes a mechanical interlock with the substrate resulting in an increase in ice adhesion compared to Cassie ice.

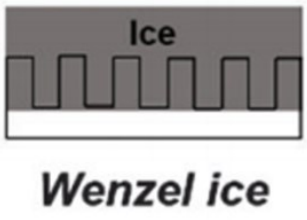

Figure 10. Wenzel ice infiltrating surface asperities [57]

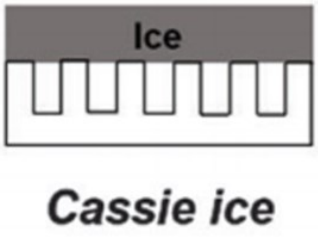

Figure 11. Cassie ice remaining above surface asperities [57]

Based on the facts presented, hydrophobicity is a required quality for a candidate icephobic surface, however if the surface is textured and superhydrophobic, maintaining the Cassie-Baxter state in harsh operating conditions could prove to be challenging.

2.2.2 Ice Nucleation Development

The second line of defense icephobic surfaces should have is the ability to delay ice nucleation and hinder the solidification process. Since the icing process can be viewed simply as nucleation and ice growth development on a surface, it is paramount to try and control the nucleation as much as possible [8]. In aerospace or wind turbine applications, delaying the freezing process increases the chances that supercooled droplets will be forcibly removed prior to freezing or adhesion. In homogeneous nucleation, when there aren't any surfaces or foreign influences, hydrogen bonds (Figure 12) within the water molecules begin to form rings and continually break until they are stable [8]. At this point the system is still in a disordered state, until the hydrogen rings form a polyhedral structure comprised of "long-lived" hydrogen bonds [8]. This structure is called the initial nucleus, and once it has the required shape and structure, rapid expansion commences, bringing the water molecule to a stable state [8]. As seen in Figure 13, all that remains are strong polyhedral hydrogen bonds which is more commonly known as ice [8].

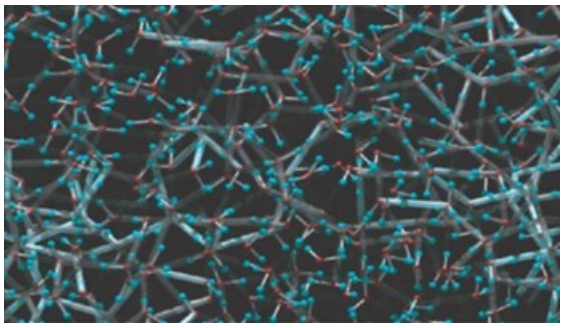

Figure 12. Molecular view of water prior to the initiation of ice nucleation [8]

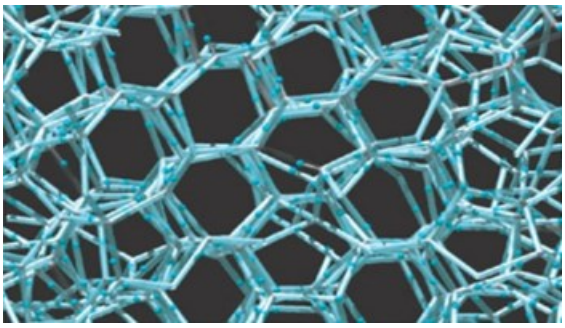

Figure 13. Molecular view of ice once ice nucleation has completed [8]

Homogeneous nucleation only occurs in suspended air with minimal impurities. However, in the development of anti-icing surfaces, ice is formed using heterogeneous nucleation. Due to the vast number of potential factors that may initiate heterogeneous nucleation, mitigation methods are challenging to develop.

Decreasing the solid/liquid interface is a potential deterrence to ice nucleation and can be done by using micro/nano-textured superhydrophobic surfaces [8]. When in a Cassie wetting state, caused by the surface roughness, the result is less contact area between the droplet and surface leading to less heat transfer during the cooling process [8]. By reducing the heat transferred to the surface, nucleation and solidification can be delayed [8]. The opposite effect can occur when a Wenzel state is present resulting in more heat being transferred resulting in an accelerated heat transfer. On the other hand, the use of low surface free energy materials can also serve as a nucleation and solidification deterrence solution [8]. When water droplets impact a surface, a decrease of the system's free energy is observed thus easing the phase change required to form ice. Therefore, introducing a low surface free energy material increases the total amount of energy required for the water to transform into ice, hindering the overall process [8].

2.2.3 Ice Adhesion Characteristics

The final line of defense, required in an icephobic surface, is the reduction in ice adhesion. Due to the inevitable occurrence of surface wetting and ice nucleation, minimizing the adhesion with ice is the final factor for the control of ice accumulation on a surface. Although water and ice share similar properties, like surface energy/tension, their adhesion characteristics have notable differences due to the influence of the phase transformation [60]. Ice adhesion can be broken down into four coexisting adhesion mechanisms; covalent or chemical bonds, electromagnetic interactions (van der Waals forces), electrostatic interactions, and mechanical bonds [60].

The first bonding category, covalent bonds, are the driving force which binds atoms together and makes up molecules [61]. Covalent interactions are considered short range and as the bonding distance increases, the bonding strength decreases [61]. With a range of 0.1-0.2 nm, covalent bonding is not considered a main influence on solid/ice adhesion, although it remains present [61]. Secondly, the van der Waals forces act on a greater range, although they start decaying when the dispersion is greater than 5 nm [62]. The van der Waals forces tend to be independent to experimental conditions because they are typically defined by macroscopic characteristics of two bodies, such as frequency varying dielectric

properties [60]. As such, the latter two bonding forces are not considered to a great degree in ice adhesion analysis.

A very well-known adhesion mechanism between two dissimilar solid materials is electrostatic forces [61]. When two materials have an imbalance of either ions or electrons there is an electrostatic force and in certain cases this force can have a range in the order of centimeters [61]. With a range of this magnitude, electrostatic forces can be considered the largest influencing force compared to other adhesion forces. Electrostatic forces are created when the surface charges found on ice induces mirror charges in the contacting surface, which creates adhesion by attraction. This phenomenon is most prominent in metallic materials because of their inability to act as an electrical insulator. For this reason, the use of dielectrics can reduce the electrostatic forces and resulting ice adhesion [9]. Since electrostatic forces are inversely proportional to the dielectric constant, a material with a very low dielectric constant is needed to reduce ice adhesion, such as polytetrafluoroethylene (PTFE or Teflon®).

The final mechanism is called mechanical bonding, although it is considered more of an obstacle than a bonding force. When surface roughness interlocks with a substance such as ice, it causes physical and geometrical entanglement rendering high adhesion [4]. Since surface roughness greatly affects this mechanism, obtaining a smooth surface finish can reduce the degree of mechanical interlocking. In the quest to develop an icephobic surface, obtaining the lowest surface roughness will generally improve the surface's ice releasing ability.

2.3 Ice Mitigation Systems

Ice mitigation systems are divided in two main categories: anti-icing and de-icing systems, as seen in Figure 14. These ice mitigation systems are referred to as ADIS; Anti-Icing and De-Icing Systems [7]. Anti-icing is the ability to prevent ice adhesion on the surface whereas de-icing is the removal of ice that has accreted to a surface [7]. Within these systems are two types of methods, active and passive. An active method is a consistent effort in repelling the accretion of ice to the surface using an external system that requires a power source. Alternatively, passive methods use the geometrical properties of the contact surface and material properties in order to prevent the ice from adhering [7]. Many

of the ADIS systems found on aircrafts, as listed in the following sections, can be applied on helicopter rotors or wind turbines, however certain adjustments and material limitations can limit their use [7]. [63]

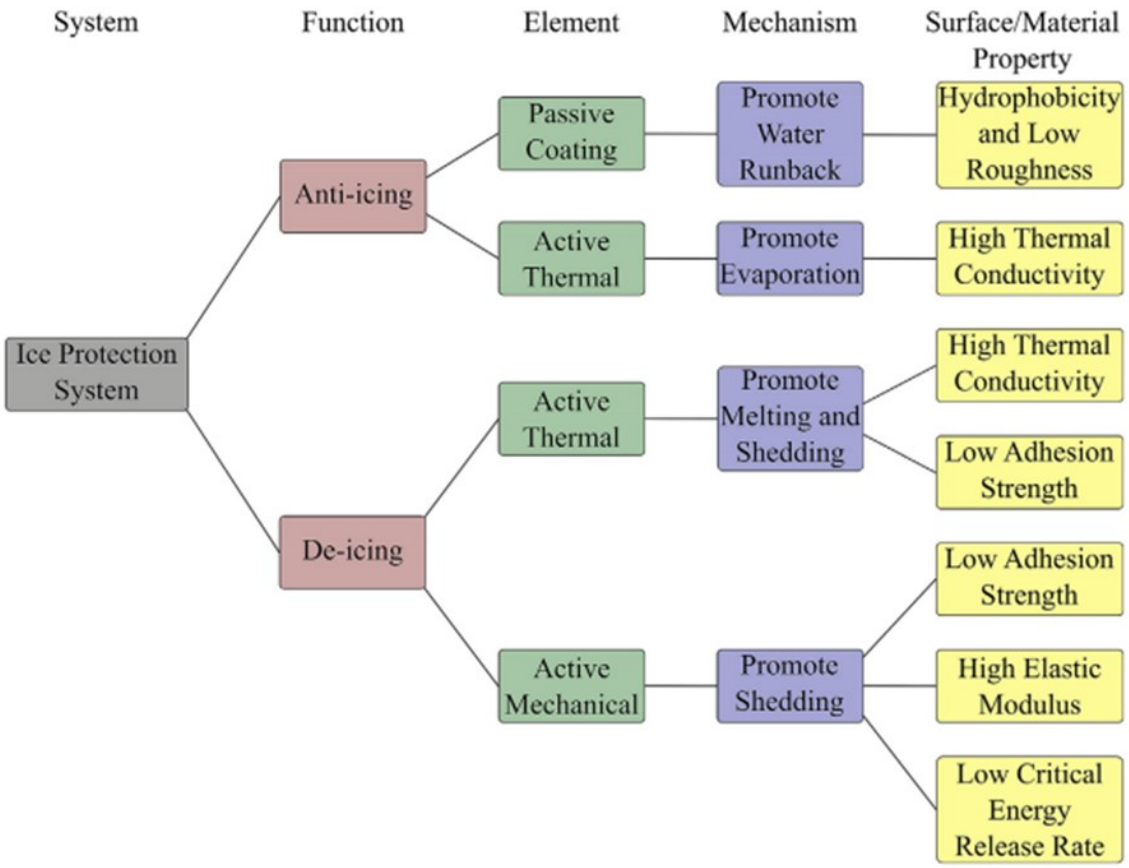

Figure 14. ADIS categories based on general function, system operation, mitigation mechanism, and surface/material property [63]

2.3.1 De-Icing Systems

2.3.1.1 Inflatable Boots

One of the most commonly used de-icing systems are inflatable rubber boots. This active mechanical solution, as seen in Figure 15, is comprised of rubber pockets located on the leading edge of the wing or propeller integrated within the structure, and are activated by an onboard compressor (piston powered aircrafts) or by the bleed air system (turbine powered aircrafts) [64].

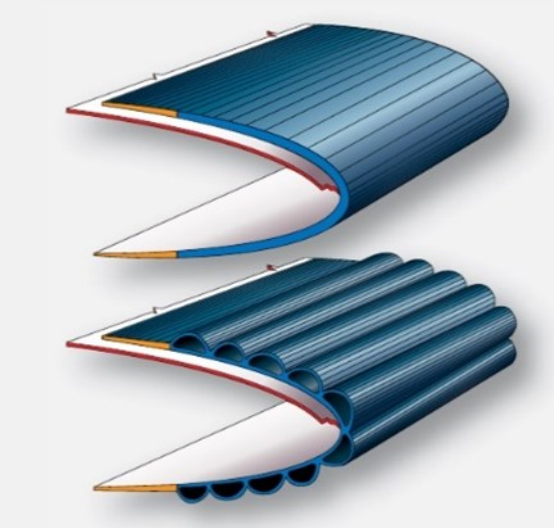

Figure 15. Inflatable boot system [64]

The inflation of the boots physically expands the surface allowing ice to break and be removed by the flowing air. Ice build up from 6 to 13 mm needs to be accreted on the wing before activation of the boots, and the inflation cycle only lasts a few seconds [7]. Deflation is conducted under vacuum to reposition the rubber panels and conform them to the aircraft's wing [7]. Activation of rubber boots, for aircrafts, is done visually at the pilot's discretion, although for wind turbines it is controlled by onboard sensors detecting ice build up [7]. In the aerospace world, controversy has surrounded this de-icing solution because of the undefined moment to activate the boots in the icing process. Many pilots choose to activate the boots when major ice build up occurs, meanwhile the Federal Aviation Administration (FAA) has suggested otherwise with their thorough ice accretion studies and tests [64]. In addition, in the event of a puncture to the rubber boot, ice accretion will accumulate in different weighted amounts causing a structural imbalance which can be especially detrimental on dynamic structures like aircrafts or wind turbines [64]. The use of inflatable boots is very common but arguably not the most efficient method to remove ice.

2.3.1.2 Electro-Impulsive De-icing System

The electro-impulsive de-icing system (EIDI) has been around since 1937 and has been tested on numerous aircrafts [6]. As seen in Figure 16, actuators are installed inside the surface of the leading edge [6]. The actuators are made up of high-voltage capacitors that discharge very quickly, resulting in an electromagnetic repulsive force in the direction of

the ice [6]. This system has proven to be very efficient, although the electromagnetic interference can cause issues for the aircraft controls [6]. Moreover, the activation of the system has proven to be acoustically disturbing for passengers onboard, therefore it could only be applied on vertical and horizontal stabilizers at the rear of the aircraft [6]. A final disadvantage of this system is the potential increase in structural fatigue applied on the wings, which increases maintenance intervals and reduces the life of the materials [6].

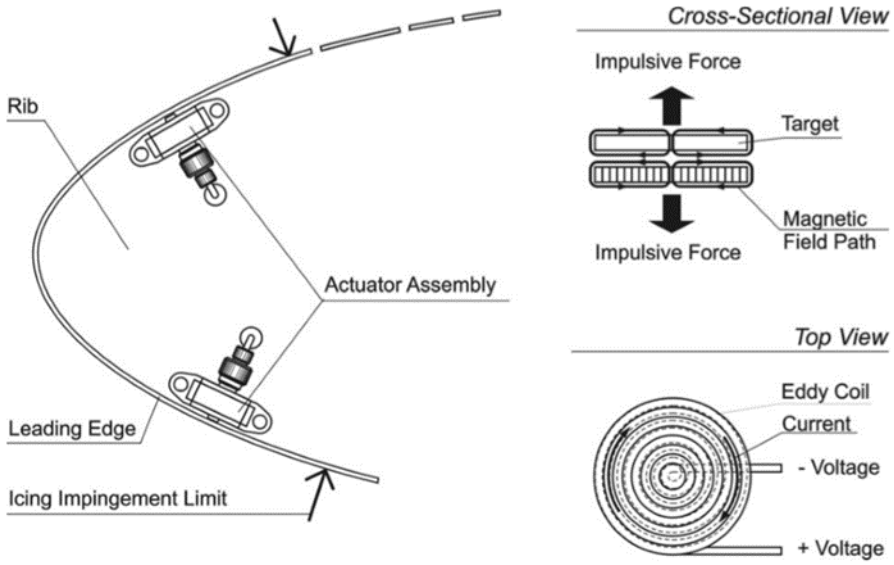

Figure 16. EIDI system [6]

2.3.1.3 Sonic Pulse Electro-Expulsive Deicer

The Sonic Pulse Electro-Expulsive Deicer (SPEED) is an improved version of the EIDI system [6]. Developed in collaboration with the National Aeronautics and Space Administration (NASA), this system uses the same impulsive loads applied on the inner leading edge of the aircraft, although with greater actuator acceleration [6]. The SPEED system can repulse ice layers 12 mm thick and, with the use of icing sensors, can be autonomously activated during flight [6]. SPEED's various ice detecting sensors can automatically determine if a shedding cycle is required, thus removing the human error aspect [6].

2.3.1.4 Electro-Expulsive Separation System

The Electro-Expulsive Separation System (EESS) is comprised of two systems working together; a controller and an expulsive boot [6]. The boot system is made of conductors

which, when supplied with an electrical current, are repulsed by their magnetic fields [6]. This repulsive force expands the boot, which breaks the ice on the leading edge of the wing, as seen in Figure 17. This system works in a similar fashion as inflatable boots but does not require large pneumatic tubing, rather much smaller electrical wiring. The electrical current passing through the conductors occurs within a millisecond, as a result the repulsive movement expands around half a millimeter [6]. According to Z. Goraj, EESS's only require one-thousandth the power and are one-tenth the weight of electro-thermal de-icing systems [6].

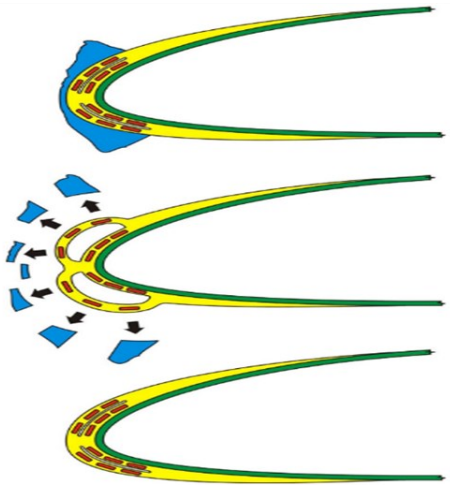

Figure 17. EESS system [6]

2.3.1.5 Resistive Heaters

Resistive heater systems consist of embedding heating elements slightly below the aircrafts leading edge surface or they may also be laminated on the surface itself [7]. The electrically heated foils are typically made of heating wires or carbon fibres [7]. Two heating panel examples are shown in Figure 18. The main objective for this type of system is to melt a small part of the accreted ice to create a thin water film [7]. Once that film is created, centrifugal or aerodynamic forces will shed the water from the surface [7]. Efficiency for heating resistance is very high due to direct heating, although there are two main concerns [7]. For wind turbines or aircrafts, if a heating element does not function properly on one side of the device, uneven ice accretion will occur, and this can lead to a weight imbalance [7]. Furthermore, heating element systems on aircrafts create water runback [7]. Water runback is when the liquid layer on the edges of the heating elements gets pushed back by

aerodynamic forces and encounter a cold part of the wing which results in refreezing. This process can occur continuously, and ice can build up in these areas as they are not impacted by the heating elements [7].

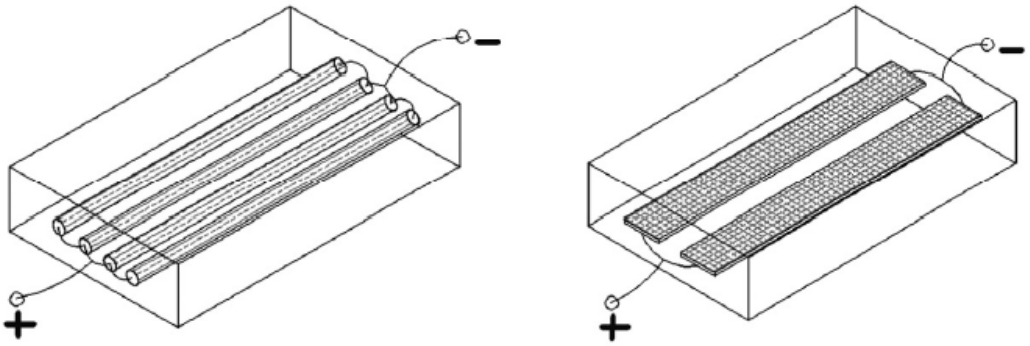

Figure 18. Heating panel examples: carbon filament (left), woven carbon fabric (right) [65]

2.3.2 Anti-Icing Systems

2.3.2.1 Microwave Heating

Microwave heating is an active anti-icing system and consists of keeping the blade or wing surface at a temperature at, or above, 0 ℃. As seen in Figure 19, the microwave emitter (2) is in the leading edge (6) of the aircraft wing (1). The microwaves are emitted by a conventional oscillator, a Klystron tube, and then are absorbed by a thermal propagation tube (3) thanks to a highly absorptive paint within the tube [5]. The highly absorptive paint converts the microwave energy into thermal energy which is then conducted through aluminum thermal transfer vanes (4) [5]. The thermal energy in the transfer vanes then heats the leading-edge surface (7) to prevent ice formation. This system also utilizes a microwave reflecting panel (5) to contain all microwave energy within the leading edge of the wing [5]. If designed efficiently, this system can successfully prevent ice accretion, although it has yet to be implemented in functional aircrafts [7].

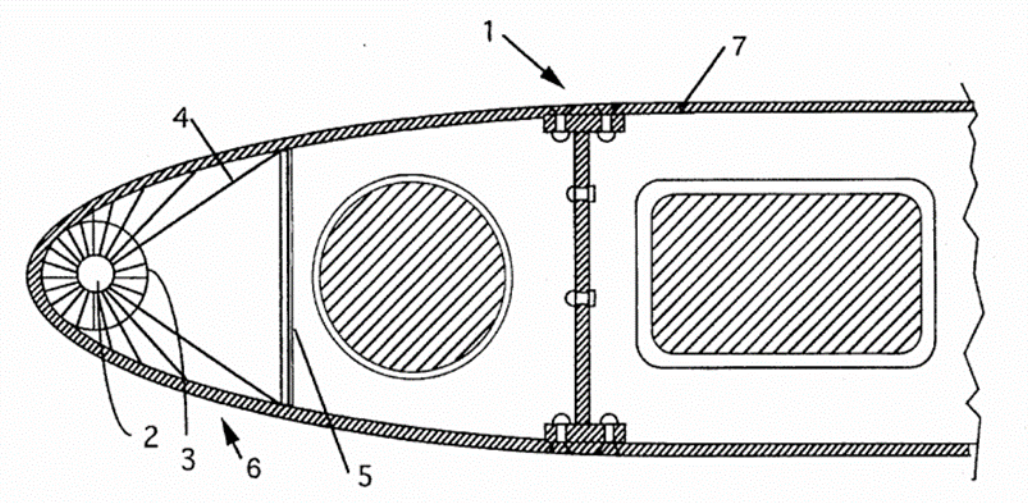

Figure 19. Microwave heating system [5]

2.3.2.2 Slippery Liquid-Infused Porous Surfaces

Ice accretion can occur when accumulations of liquid water droplets freeze upon impact on a surface, although air moisture can also induce ice nucleation on surfaces seen as frost [4]. Slippery Liquid-Infused Porous Surfaces (SLIPS) are a different approach to mitigating ice accretion on surfaces, focusing primarily on preventing ice nucleation or frost formation [4]. This type of anti-icing solution was derived from the *Nepenthes* pitcher plant, as opposed to following the very common hydrophobic Lotus effect [4]. The Lotus effect capitalizes on micro-textured surfaces and trapped air to roll-off water droplets from the surface [29]. This approach is effective in environments when hydrophobicity is required, although limitations restrict its application in icing conditions [29]. On the other hand, SLIPS also use micro-textured surfaces but introduces a liquid as the repelling agent rather than air [29]. This passive anti-icing system, as show in Figure 20, consists of a combination of a nano-porous structure infused with a low freezing point liquid [4]. The liquid trapped within the structure takes on the name “slippery”, since liquids have the smoothest of surfaces, this allows foreign liquids like water droplets to roll off and prevents heterogenous nucleation [4]. SLIPS function well in icing conditions thanks to their low freezing point liquid, although depletion of the lubricant is a common issue over time [4]. In addition, there has yet to be high-speed impacting water droplet testing on these types of surfaces at this time.

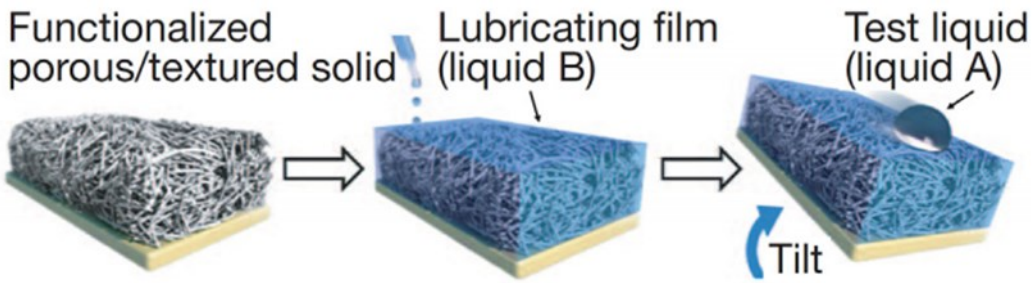

Figure 20. SLIPS system [4]

2.3.2.3 Hot Air Injection

This active anti-icing system utilizes thermal energy already being produced by aircrafts. Hot air injection systems consist of rerouting the hot bleed air from the turbines and distributing it across the wing through ducts [66]. This method uses forced convection through the ducts and relies on heat conduction to the leading edge's surface in order to melt the ice [66]. This system is very common on larger aircrafts since thermal energy is already being produced by gas turbines, and it is also convenient as the turbine is near the middle of the wing, therefore long spans of air distribution are not required [66]. This technique can also be implemented in wind turbines, although the fan pushing the air is usually near the rotation axis of the blades, as seen in Figure 21 [66]. As such, uneven heat gradients throughout the wing's span will occur.

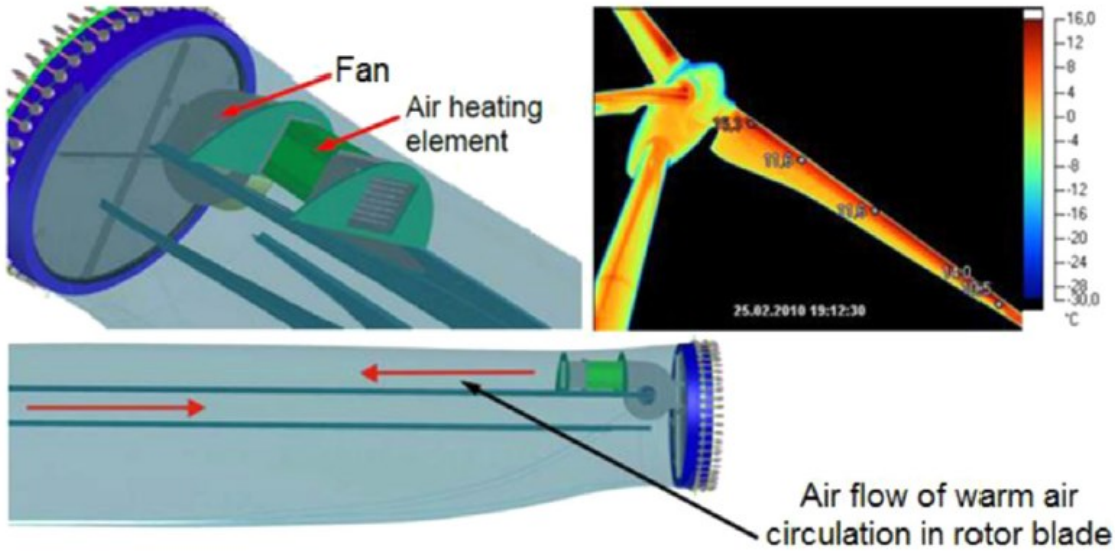

Figure 21. Hot air injection system for wind turbine blade. Hot air is distributed throughout the inner blade structure to heat blade and melt accreted ice on the outside of the blade [66]

2.3.3 Hybrid Systems

2.3.3.1 Coatings as Heating Elements

Recent aircrafts and wind turbines have wings/blades designed with carbon or glass fiber-reinforced polymer composites (FRPC) because of their high toughness and high strength to weight ratios [67]. Many of the ADIS systems listed above pose an issue for FRPC structures because of their sensitivity to heat. As such, resistive heating is often implemented in FRPC's as the most effective method due to material property constraints [67]. A more recent resistive heating design utilizes thermal spraying to deposit conductive material on the FRPC surface as a coating [67]. Applying a coating ensures even distribution as well as complete protection of the surface subject to ice accretion. Electrical current is injected in the coating and is heated by Joule heating (or resistive heating), allowing the surface temperature to remain above water freezing point [67]. Certain TS processes with elevated process temperatures, like flame spraying (FS), have proven to be detrimental to FRPC substrates causing degradation and burning [67]. As Lopera-Valle and McDonald [67] have demonstrated, garnet sand was placed on the substrate as it was curing in order to create a thermal barrier from their FS process [68]. As an added advantage, the surface roughness from the sand promoted adhesion of the metal alloy coating [68]. It has also been reported that depositing alumina can serve as a thermal barrier

coating [68]. Furthermore, alumina not only has unique thermal properties, but its electrical properties can also make it a great electrical insulator to prevent short circuits caused by the resistive heating [68]. Although FS has its advantages, other methods shown by Robitaille et al. [69], present similar results without the downfalls. Their work showed the deposition of metallic coatings on FRPC substrates, but with the pulsed-gas dynamic spraying (PGDS) method. Similar to the conventional CS process, the PGDS method is considered a solid-state process, meaning process temperatures are much lower than the melting temperature of the sprayed material [69]. As a result, with the pulsating flow of particles and lower process temperatures experienced by the substrate, FRPC burning and degrading is avoided. Heating elements in the form of coatings are considered hybrid systems for their complete coverage of the substrate's surface resulting in both de-icing and anti-icing capabilities, however they remain a work in progress.

2.3.3.2 Electromechanical and Icephobic Coatings

The elevated power consumption related with the operation of active ADIS systems, as listed previously, remains an outstanding issue in the field. For this reason, active systems have attempted to couple the efficacy of certain active solutions, like electromechanical systems, with the passiveness of icephobic coatings. Pommier-Budinger et al. [70] suggested the use of piezoelectric systems coupled with icephocic coatings; namely plasma sprayed polymer and commercially available silicone-based coating. The high resonance frequencies produced by the piezoelectric system enabled lower ice adhesion with minimal voltage requirements. The layering of this system with an icephobic coating also capable of reducing ice adhesion, suggests a higher efficiency than either system used on their own.

2.4 Thermal Spraying

Industrial coatings have a wide range of purposes based on their application, such as thermal barriers to increase working temperatures, erosion protection in harsh environments, ice adhesion protection for atmospheric icing, and so on. The deposition of such coatings requires careful considerations to obtain the required coating thickness, microstructure, surface finish, etc. TS is a class of deposition methods that involves accelerating particles that are molten, semi-molten or solid towards a substrate [71]. As demonstrated in Figure 22, various TS processes exist leveraging either a high temperature

and/or high velocity gas stream to propel feedstock particles towards a substrate. The creation of coatings is achieved when particles impact and bond with the surface [71]. With particles accumulating on the substrate, the result is a coating of a given thickness. Many different TS processes exist, although they are generally categorized by the source of energy utilized [72]. The categories are split into four groups; plasma spraying, electric arc spraying, combustion spraying and kinetic spraying [72].

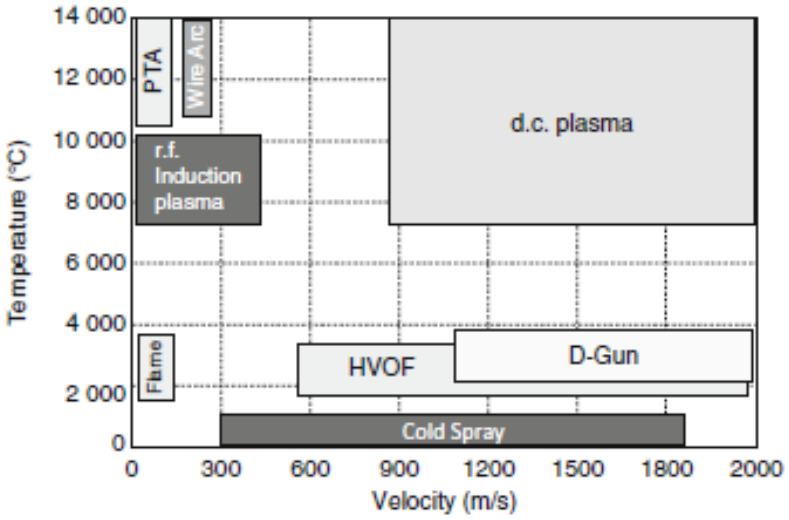

Figure 22. Gas temperature and velocity for different thermal spray processes [73]

2.4.1 Flame Spray

Flame spray, or FS, is classified as a combustion spraying process because of the use of a flame as the source of thermal energy [72]. FS consists of using the combustion of a flame in the form of a torch, paired with the injection of particles that consequently become molten and accelerated by the flow towards a substrate, as seen in Figure 23 [71]. The molten particles then impact the substrate and solidify to create a coating [74]. FS is a common technique to produce thermoplastic polymer coatings due to their relatively low melting temperature. This results in easily melted particles in the flow that will bond together once they encounter the substrate [74]. Although FS has been used for the manufacturing of polymer coatings, it does have drawbacks for the quality of the results. The use of a flame to heat the particles above their melting temperature results in possible polymer degradation if the parameters are not perfectly optimized [74]. Polymer

degradation can result in poor coating properties such as chain scissions, loss in mechanical properties, and a brittle coating [74].

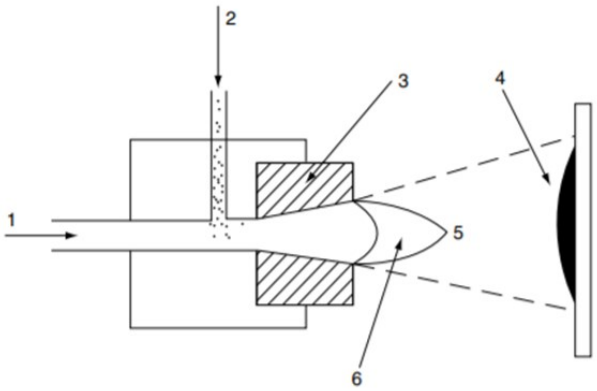

Figure 23. Flame Spraying equipment: (1) gases inlet (fuel and oxygen); (2) powder inlet; (3) torch; (4) sprayed coating; (5) particle stream; (6) combustion flame [71]

2.4.2 Plasma Spray

Direct current (d.c.) plasma spraying, or plasma spray (PS), uses a non-transferred arc to heat a propellant gas, creating a plume of plasma at the nozzle exit [73]. Feedstock material, typically as a powder, can be injected radially, as seen in Figure 24, or axially, and is then accelerated and melted in the plasma towards a substrate. PS can be operated in atmospheric conditions or under a vacuum when oxidation needs to be avoided, such as the deposition of superalloy feedstock in the creation of thermal barrier coatings [73]. Plasma forming gases typically consist of argon or a mixture of argon and other gases, and temperatures reached in the jet can range from 8,000-14,000 K [73]. As a result of such high jet temperatures, PS is capable of depositing ceramic feedstock onto metallic substrates [71]. Conversely, the high temperatures seen in PS disqualifies this process as a potential deposition method for polymer feedstock or any other temperature sensitive materials.

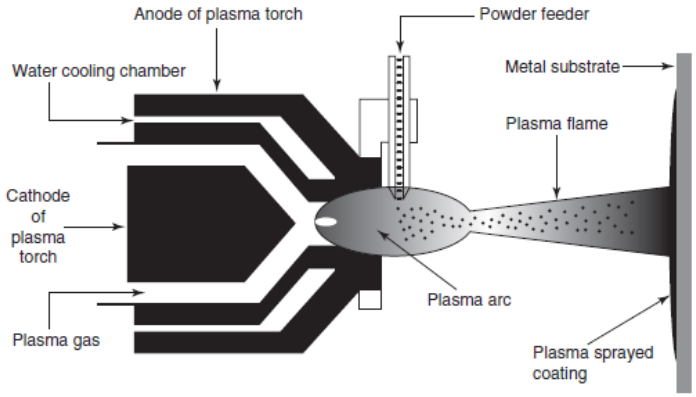

Figure 24. Plasma spraying schematic [75]

2.4.3 High Velocity Oxygen Fuel Spray

Similarly to FS, a high temperature combustion is involved with high velocity oxygen fuel (HVOF) spraying, however the process occurs at higher velocities [73]. The propellant gas in HVOF consists of the exhaust gas of a pressurized combustion, pushed through a de Laval nozzle [71]. The nozzle allows the gas to expand and reach supersonic velocities which then propels feedstock particles towards a substrate. Powder injection is either done upstream and axially with a pressurized powder feeder, as shown in Figure 25, or downstream and radially with a conventional powder feeder [73]. HVOF is typically limited to metals, alloys and cermet feedstock because of the high operating temperatures [73]. However, the process typically yields high quality coatings with less than 1% porosity, low-oxide content, and is usually comparable to PS [71], [73].

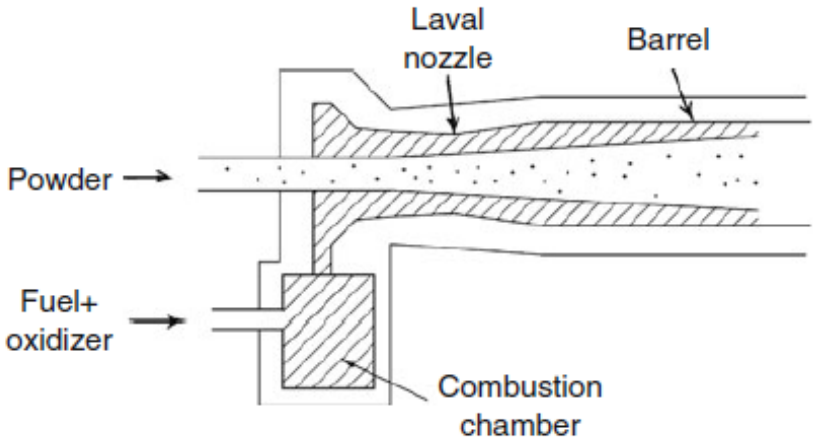

Figure 25. Axial powder injection in HVOF spray gun [73]

2.4.4 Cold Gas Dynamic Spray

Cold Gas Dynamic Spray, or CS, is a deposition technique categorized as kinetic spraying, most commonly used to create coatings or recently in the manufacturing of components as an additive manufacturing process [76]. As seen in Figure 26, the CS process begins with pressurized inert gases accelerated through a de Laval nozzle (converging-diverging) to reach supersonic velocities and accelerate powder particles towards a substrate [76]. The gases are heated to temperatures up to 1000 ℃ in order to reach greater velocities [48]. When the gas flow is accelerated, the thermal energy is converted to kinetic energy causing a considerable drop in temperature, giving it the name “cold” spray. Particles can be injected into the gas stream prior to the converging-diverging nozzle section or after the nozzle throat, depending on the system. Throughout the process, feedstock particles remain well below their melting temperature resulting in a solid-state deposition onto the substrate. The solid-state deposition prevents the microstructure from being altered and preserves the material mechanical properties. Upon impact, particles plastically deform at high strain rates which causes localized deformation and adhesion [48].

The advantages of material property preservation suggest the potential of using CS to deposit polymer feedstock, however the high velocity flows used in the process could be a challenge when dealing with such delicate materials. Many recent studies have looked into the deposition behavior of polymers using CS because current knowledge on subjects like particle bonding mechanisms are associated with the more conventional metallic particle deposition [37], [38], [41], [77]. As such, current best practices used in the field such as parameter selection, substrate preparation, or nozzle geometry, will not always yield the most optimal polymer coatings, presenting the need for further investigation into polymer CS.

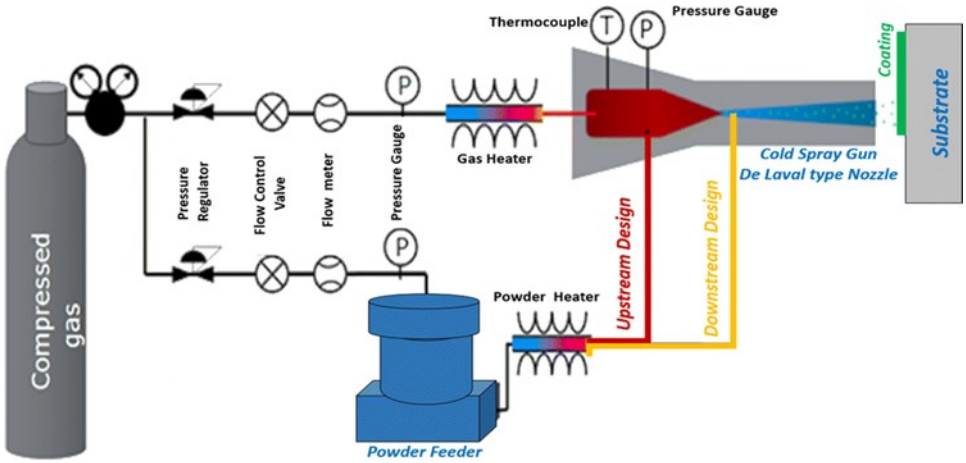

Figure 26. Cold Gas Dynamic Spray System [48]

2.5 Quasicrystals

Quasicrystals (QC), or quasiperiodic crystals, are complex metallic alloys with very different properties than conventional crystalline metals. A QC is defined as an ordered but aperiodic crystalline material with a rotational symmetry that is impossible in conventional crystallography [78]. Solid materials are either ordered, such as metals, or disordered, such as amorphous plastics [79]. Ordered solids were said to come in two-, three-, four- or six-fold symmetries, but not five or anything higher than six, as it is impossible to fill a space periodically with these symmetries [79]. An example of a 5-fold symmetry can be seen in Figure 27, displaying an icosahedral QC, meaning its crystalline structure is composed of polyhedrons having 20 faces. A transmission electron microscopy image of a QC, shown in Figure 27, was obtained by simply tilting the specimen, revealing the various symmetry axes [80]. Many icosahedral QCs such as Al-Cu-Fe or Al-Pd-Mn are metastable and they offer interesting surface properties for materials engineering applications [78]. While it is of great interest to utilize these properties, its weaknesses, such as high hardness and brittleness at room temperature, have prevented its use in bulk form [17].

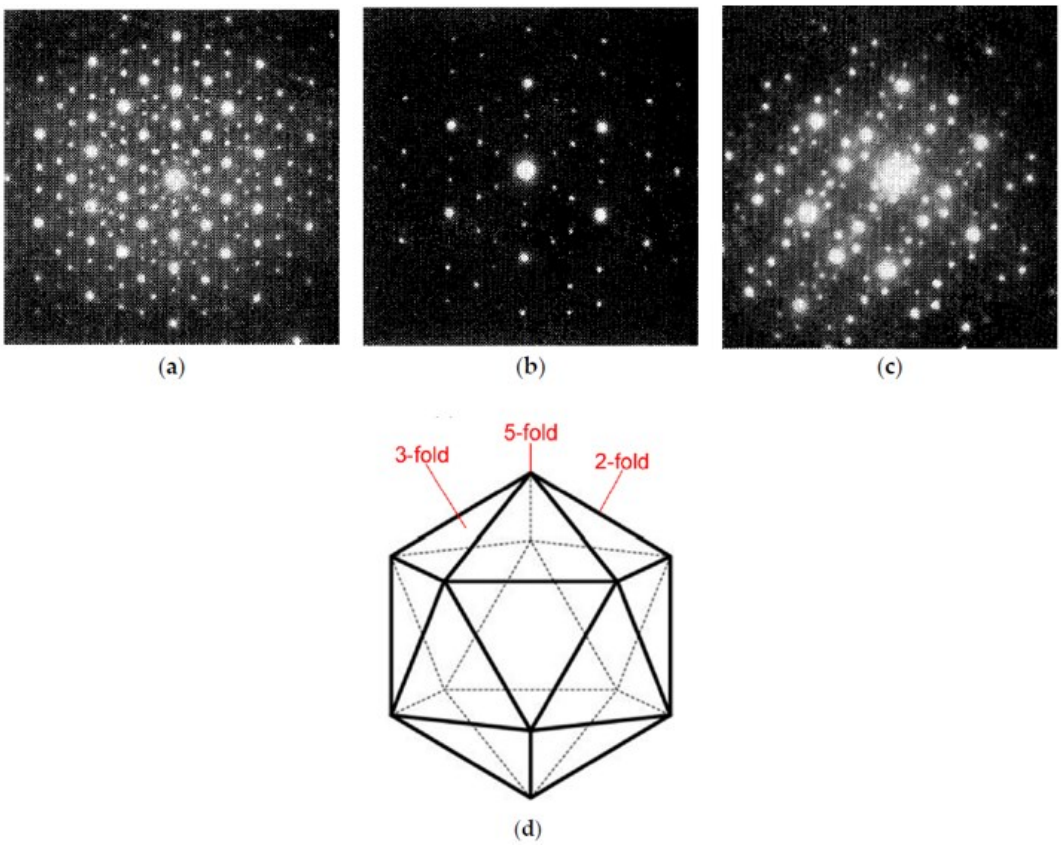

Figure 27. Icosahedral structure, using selected area electron diffraction. Taken along a) 5-fold symmetry axis; b) 3-fold symmetry axis and c) 2-fold symmetry axis; d) all three types of symmetry axes found in the icosahedral structure [80]

2.5.1 Properties

The interest in QCs boils down to their unique properties compared to crystalline metals [81]. The main drawback for bulk QCs is their brittleness at room temperature, although it has been established that when above 600 ℃, QC's dislocations are quite mobile [82]. Since QCs have non periodic structures, dislocations can not simply slide through atomic planes like they would in ordered materials [17]. The dislocation movement in QCs creates a cloud behind it, called the phason fault [82]. The fault makes it difficult for a dislocation movement and the material appears brittle as a result [82]. A notable property in QCs is hardness, such as icosahedral Al-Cu-Fe (i-Al-Cu-Fe) which has a higher hardness (4-6 times) than each of its individual elements, as can be seen in Table 1 [81]. Friction coefficients of QC materials are also smaller, some being an order of magnitude, than metal alloys [81]. This surface property along with high hardness can make QCs suitable for

wear-resistant coatings, and it has been said that brittleness can be mitigated if applied in coating form [17], [83].

Table 1. Icosahedral QC properties compared to other materials

Property	Material	Value
Hardness (H_v) [17], [81]	Diamond	6000-10000
	Silica	750-1200
	i-Al-Cu-Fe	800-1000
	Copper	40-105
	Aluminum	25-45
Coefficient of Friction (unlubricated with diamond pin) [81]	Copper	0.42
	Aluminum Alloy	0.37
	Low-carbon steel	0.32
	i-Al-Cu-Fe	0.05-0.2
Surface Energy (mJ/m^2) [17], [81]	Iron (clean)	2480
	Copper (clean)	1830
	Alumina	50
	i-Al-Cu-Fe	24-25
	Polytetrafluoroethylene	17-18

Pure metals or metallic alloys do not have low surface energy [81]. Metals with a clean surface have surface energies of one or two orders of magnitude larger than QCs or certain polymers like polytetrafluoroethylene (Teflon) [81]. QCs have low surface energy because of a “pseudo-gap” creating a lack of space for electronic interactions with liquids, such as water, and other surfaces [17]. For that reason, QCs have been used as coatings on non-stick frying pans and are also considered for other water repelling applications [81].

2.5.2 Production of QC Powders

Producing QC materials is not widespread commercially, at this time. More specifically, the production of i-Al-Cu-Fe is quite difficult as the QC phase is only stable within a very small window [83]. Metallic powders can be manufactured in a number of ways such as mechanical alloying, vaporization by laser beam, crushing of ingots, centrifugal

atomization, gas atomization, water atomization, etc [78]. Despite having various established powder manufacturing methods, the creation of QC phases lies in the heat treatment and therefore special considerations must be made depending on the desired crystalline structure [78].

2.5.3 Cold Spray of QC and Ceramic Deposition

Literature on the cold spray deposition of QC feedstock is limited at this time [50], [51]. In one study, aluminum-rich QCs were deposited on aluminum substrates, however deposition only occurred when the low pressure system used helium as the propellant fluid [50]. The use of helium allowed particles to reach their critical velocity resulting in plastic deformation and subsequent deposition, whereas nitrogen resulted in no deposition. Despite QCs being metallic alloys, their inherent brittleness suggests that their deformation mechanisms may also resemble that of ceramic materials. The deposition of ceramic particles using the cold spray process has been explored in previous studies, mostly using TiO_2 for photocatalytic applications [84], [85]. One method that has proven successful in depositing ceramic feedstock is to use polyvinyl alcohol to serve as a binder during deposition through the formation of nano-agglomerates on the TiO_2 particles [86]. Although particle adhesion to the substrate increased because of the binding material, the resulting coating was very porous and the impurities from the organic binder decreased overall photocatalytic properties. Other work demonstrated that ceramic particles could be deposited onto metallic substrates in a low-pressure environment, i.e. vacuum [84]. Spraying of ceramic particles in a vacuum prevented a bow shock from forming over the substrate and slowing down particles. Although effective, deposited coatings only used nano-sized particles as opposed to the micron sized particles typically used in the CS process. Other deposition methods include the embedment of ceramic particles into the substrate to create a thin layer acting as a coating [87]. This method relies on the plastic deformation of the substrate material, rather than the more brittle feedstock particles. However, the final coating thickness is typically only made up of a single layer of particles as poor particle cohesion prevents the accumulation after the first layer.

2.6 Ice Adhesion Testing Methods

The study of ice adhesion involves many factors that all need to be accounted for. Many methods use statically produced ice in their tests, meaning the ice is not produced with high-speed impacting supercooled water droplets [88]. Results using statically produced ice does not adequately represent operating conditions when it comes to aircraft, helicopters, or wind turbine applications, however it is the most simple and cost-effective method [88]. In addition, since ice is a temperature sensitive material, testing reproducibility and repeatability is difficult to achieve as different labs may produce ice with different properties [88]. As such, the results from these tests are to be used in a qualitative comparison with the bare substrate being tested [88]. The adhesion reduction factor (ARF) is typically the desired value when testing ice adhesion because it uses both the icephobic candidate and substrate making it a comparable value with other studies. The ARF is simply a ratio of the adhesion strength of the bare substrate or reference material and the adhesion strength of the icephobic coating itself.

2.6.1 Centrifuge Adhesion Test

The Centrifuge Adhesion Test (CAT) dates back to 1946 and many variations of the CAT now exist. The test uses a rectangular bar, or rotor, mounted symmetrically on a rotating shaft [88]. As seen in Figure 28, on one end of the rotor is the icephobic coating with the ice sample adhered on top. To account for the ice sample's mass and to achieve a dynamically balanced rotation of the bar, a counterweight is added on the opposing side [88]. The test begins with an angular velocity of zero and constantly increases until the ice detaches from the coating [88]. A vibration sensitive sensor is mounted on the rotating shaft in order to determine when the rotations begin to be unstable [89]. At the moment when the instability occurs and shaft vibrations are sensed, the angular velocity is recorded and used to determine the centrifugal force [89].

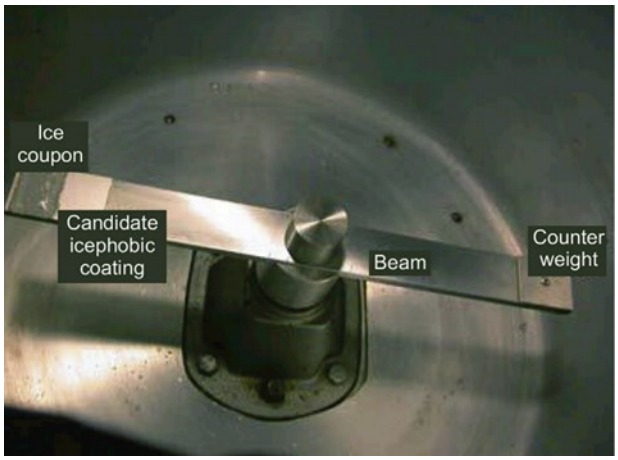

Figure 28. CAT configuration [89]

The centrifugal force at that instant is given by the equation

$$F = m * r * \omega^2 \tag{4}$$

where F is the centrifugal force (in N), m is the ice mass (in kg), r is the rotation radius (in m), and ω is the angular velocity (in rad/s). Determining the adhesion strength of the coating is dependent on the area of the piece of ice that has detached. For that reason, an ideal test would be when the ice sample has completely detached from the coating since the area is known. Otherwise, if ice has broken from itself, cohesive bonds have broken and the test results do not directly reflect the coating's icephobic performance [89]. The coating adhesive strength is given by the equation

$$A_s = \frac{F}{A} \tag{5}$$

where A_s is the coating's adhesive strength (in Pa), F is the centrifugal force (in N), and A is the area of detached ice (in m^2). The CAT can use both ice accretion methods: statically produced ice or high-speed impact ice [89].

2.6.2 Calculated Centrifuge Adhesion Test

The Calculated Centrifuge Adhesion Test (CCAT) is very similar to the original CAT although it involves more theoretical calculations [88]. This method, used by Itagaki, consists of calculating the shear and tensile adhesion strengths of the coating based on a shed piece of ice that is subject to a centrifugal movement [90]. Once the piece of ice has shed from the rotor, the height and length of the ice piece is recorded. The values for the shear and tensile adhesion strengths are derived from the model found in Figure 29 [90].

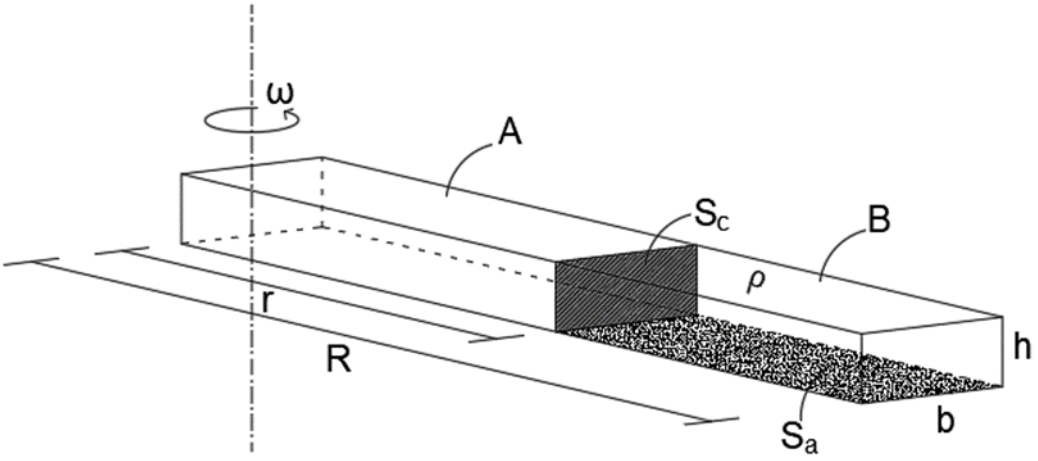

Figure 29. CCAT model [90]

The model shown above demonstrates two rectangular components, *A* and *B*, bonded at S_c. The centrifugal force acting on S_c is given by the equation

$$F_t = \int_{l=r}^{R} l * \omega^2 * \rho * S_c \, dl \tag{6}$$

where F_t is the centrifugal force (in N), *r* is the distance from the axis to S_c (in m), *R* is the radius of the total component (in m), ρ is the material density (in kg/m^3), S_c is the component's cross-section (in m^2), and ω is the angular velocity (in rad/s). From equation (6), it is concluded that component B will break off if

$$F_t > A_t * S_c \tag{7}$$

where A_t is the adhesive tensile strength (in Pa). Considering that component A and B are made of ice, with thickness *h* and a width *b* (in m), equation (6) and (7) are simplified to

$$F_t = \frac{\omega^2 * \rho * b * h}{2}(R^2 - r^2)$$

$$\frac{\omega^2 * \rho * b * h}{2}(R^2 - r^2) > A_t * S_c \tag{8}$$

Now considering component B is bonded at S_a on a rotor, an adhesive shearing force is applied along with the adhesive tensile force calculated previously. The adhesive shearing force is given by the equation

$$F_a = A_s * S_a \tag{9}$$

where F_a is the adhesive shearing force (in N), A_s is the adhesive shearing strength (in Pa), and S_a is the area adhered to the rotor (in m^2). For the piece of ice to break off the rotor, the centrifugal force needs to outweigh both shear and tensile forces. The difference between the two is called the supporting force margin, and is given by the equation

$$M = (Tensile + Shear) - Centrifugal$$

$$M = (A_t * S_c + A_s * S_a) - F_t$$

$$M = (A_t * S_c + A_s * S_a) - \left(\frac{\omega^2 * \rho * b * h}{2}(R^2 - r^2)\right) \tag{10}$$

where M is the supporting force margin (in N). From equation (10), if the supporting force margin (M) becomes negative, this means the ice has de-bonded from the rotor. If the supporting force margin is equal to zero, equation (10) becomes

$$r = \frac{A_s \pm \sqrt{{A_s}^2 - 2 * h * \omega^2 * \rho \left[A_s * R - h * \left(\frac{R^2 * \omega^2 * \rho}{2} - A_t\right)\right]}}{h * \omega^2 * \rho} \tag{11}$$

The solution to equation (11) becomes real when the root is equal to zero

$$0 = {A_s}^2 - 2 * h * \omega^2 * \rho \left[A_s * R - h * \left(\frac{R^2 * \omega^2 * \rho}{2} - A_t\right)\right] \tag{12}$$

Isolating for the ice sample's height (h), equation (12) becomes

$$h = \left[\frac{\omega * \rho * R \pm \sqrt{2 * \rho * A_t}}{2 * \rho * \omega \left(\frac{R^2 * \omega^2 * \rho}{2} - A_t\right)}\right] * A_s \tag{13}$$

Substituting equation (13) into equation (11), the equation for the radius (r) becomes

$$r = \frac{R * \omega * \rho \pm \sqrt{2 * \rho * A_t}}{\omega * \rho} \tag{14}$$

The adhesive tensile strength can be isolated from equation (14) and becomes

$$\boldsymbol{A_t = \frac{\omega^2 * \rho[R - r]^2}{2}} \tag{15}$$

The adhesive shearing strength can now be isolated using equation (15) and (13) and becomes

$$\boldsymbol{A_s = \frac{h * \omega * \rho[R^2 * \omega^2 * \rho - 2 * A_t]}{\omega * \rho * R + \sqrt{2 * \rho * A_t}}} \tag{16}$$

The equations derived for the adhesive shearing and tensile strengths provide an insight on the adhesive capabilities a coating could provide when applied to a rotor in icing conditions. The CCAT test also implements vibration sensors on its rotating shaft to determine the angular velocity at the moment the ice piece has been shed [90]. The standing issue with this test is since the shed ice can vary widely in sizes, the values obtained in a CCAT should be used as a qualitative comparison with other coatings and not their true values [88].

2.6.3 Instrumented Centrifuge Adhesion Test

The final CAT variation is called the Instrumented CAT (ICAT). In 2009, the Pennsylvania State University (PSU) introduced their ICAT called the Adverse Environment Rotor Test Stand (AERTS). The system consists of a large span rotor in the shape of an airfoil with a built-in force transducer mounted on its tip, as seen in Figure 30 and Figure 31 [91]. The 2.75 meter rotor span coupled with the right size motor allowed an exact representation of helicopter tip speeds [91]. A built-in strain gauge allows for the force to be tracked in real time, as such, a plot of the force as a function of time can accompany the results [88]. This test, contrarily to the other CATs, sets a steady angular velocity throughout the test while introducing supercooled water droplets, and proceeds until shedding occurs [91]. The

instant shedding takes place, the centrifugal force is recorded and, since the radius and angular velocity are known, the mass of the shed ice is computed [91]. The interfacial area of the shed ice is then calculated by superposing graphic paper on the rotor, where the ice was adhered [88]. These values allow for computation of the adhesive strength of the coating being tested.

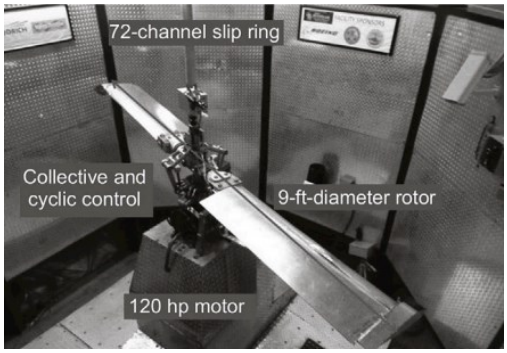

Figure 30. AERTS system [88]

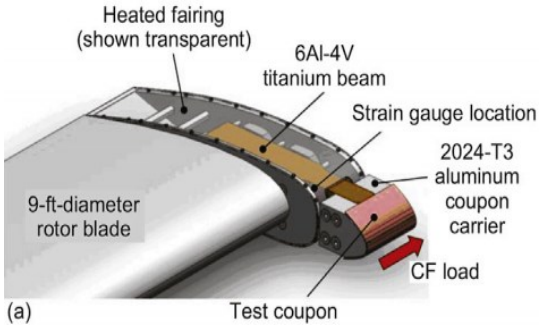

Figure 31. Rotor Force Transducer [88]

The biggest advantage the ICAT offers, is the realistic icing conditions it can create [91]. A series of standard icing nozzles are mounted on the cold chamber's ceiling to recreate accurate icing clouds [91]. Varying water pressure and air content allows for the atomisation of the water droplets within the cooled testing chamber [91]. Many factors have to be considered when recreating a valid icing test facility such as; the chamber temperature, droplet size distributions, relative humidity, icing time, water temperature, and the water purity [91]. Controlling these parameters will provide the most accurate representation of the operating conditions for aircrafts, helicopters and wind turbines. The controlled parameters at the AERTS facility were temperature, droplet size distribution and relative humidity [91]. Consequently, the AERTS facility designed at PSU remains a CAT method but delivers the most accurate icing cloud conditions of all the CATs [91].

2.6.4 Pusher Test

The Pusher Test (PT) is considered simple ice adhesion test when compared to CAT methods. A version of the PT is used at the Technical Research Institute of Finland [16]. The sample preparation uses thin rectangular substrates, coated with the potential icephobic material, paired with a removable cylinder mold placed on its surface [16]. The removable mold is filled with water and the assembly is placed in a cooled environment for a sufficient solidification period [16]. The mold is then removed, leaving an ice cylinder with one of

its faces adhered to the coating's surface. The testing begins by securing the substrate to a base and placing a belt horizontally along the cylinder's circumference which will be pulling on the ice sample, as demonstrated by the arrow in Figure 32 [16]. The ice sample is then sheared from the substrate by slowly pulling the belt away from the testing surface [16]. The shearing force is registered by a load cell at the time of shedding which allows the adhesive shearing strength to be computed using equation (5). The PT is simple and inexpensive, although it uses statically produced ice. Accordingly, its major flaw is that it does not accurately represent operating conditions for aircrafts, helicopters or wind turbines [88].

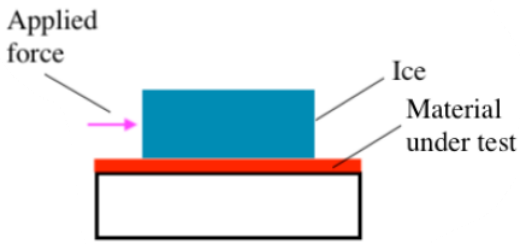

Figure 32. Pusher Test [92]

2.6.5 Shear Test

Shear tests (ST) are less common than CAT and PT, although they were the very first method to test ice adhesion [88]. There are three categories of ST; rotational shear, lap-joint shear and the 0° cone test [88]. Similar to PT, the ST uses statically produced ice, and for the same reasons as PT, is not recommended to represent high-speed impact icing applications [88]. The rotational ST, as seen in Figure 33 has two configurations; annular and cylindrical [93]. It is reported that the cylindrical configuration does not provide accurate results since unknown stress concentrations occur at the substrate's interface [93]. For that reason, the annular design is recommended, since it offers a pure shearing movement with the stress in the torsional direction [93].

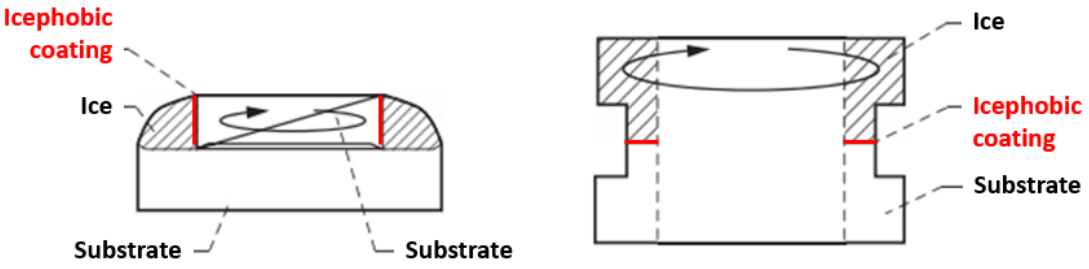

Figure 33. Rotational ST; cylindrical (left) and annular (right) [88]

The lap-joint ST is the most common of ST's because of its very simple design [88]. This method is modelled the same way as a tensile test, with the use of a load cell to register the shearing force when the ice is forcibly removed [88]. The lap-shear consists of two plates parallel to each other with an ice sample adhered to either side, as seen in Figure 34. Pulling on the plates in opposite directions results in a shearing force to remove the ice and, since the area is known, the adhesive shearing strength can be computed using equation (5).

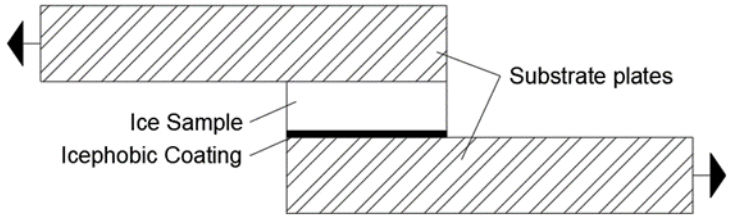

Figure 34. Lap-Joint ST

The 0° cone test is very similar to a lap-joint test although it shears annular formed ice [88]. A model used by the United States Army at the Cold Regions Science and Engineering Laboratory (CRREL) involved using a circular cylinder substrate [16]. The cylinder is coated in the potential icephobic coating and is inserted inside a larger mold, as seen in Figure 35 [16]. There is a small gap left between the mold and the cylinder allowing for ice to be formed. This test uses a load cell to push down on the cylinder while the mold is being held up, resulting in a shear force being applied on the thin ice coating between the two materials [88]. This method, like all other ST methods, do not provide accurate operating conditions of aircrafts since the ice formation is not under high-speed impact.

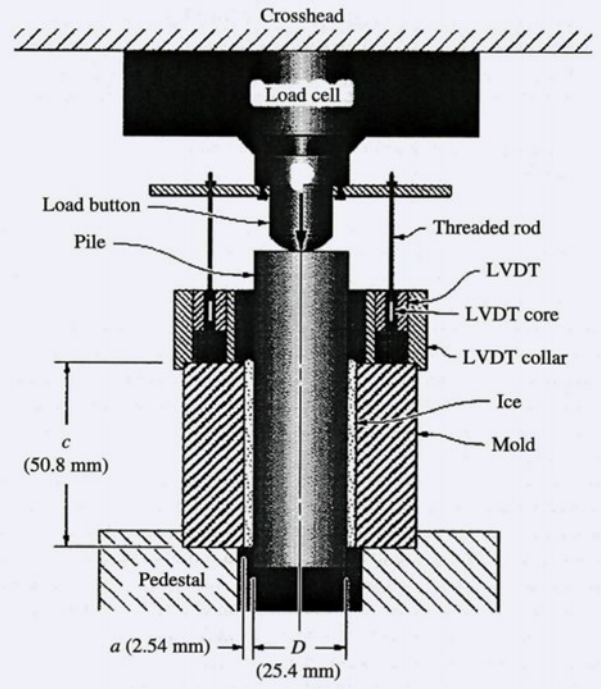

Figure 35. 0° cone test [16]

3 RESEARCH OBJECTIVES

3.1 General Objectives

The main objectives in this work were to study the CS deposition of icephobic materials and to characterize their icephobic properties. This work is split in two main icephobic solutions, differentiated by materials; namely a polymer and a complex metallic alloy. The polymer solution used adhesive perfluoroalkoxy alkane (PFA) and the metallic solution used an aluminum-rich QC, chosen for their potential hydrophobic and icephobic properties, such as low surface energy and low dielectric constant (PFA specific) [27], [40]. Recent developments of polymer icephobic coatings using other thermal spraying methods suggest the advantage of using CS [21]. However, limited work on this subject has been done and published, which has demonstrated the challenge when depositing polymers onto metallic substrates [38], [39]. This work aimed at a) adapting the cold spray process for polymeric feedstock deposition on metallic substrates, b) producing thin coatings of adhesive PFA onto aluminum substrates, c) evaluating the PFA coating's hydrophobic, d) ice nucleation/growth, and e) ice adhesion performance. Secondly, QC alloys have also shown great promise in the field of icephobic coatings, however their inherent brittleness makes plastic deformation a challenge. Literature on the production of icephobic QC coatings using CS is very limited and therefore the objective for this second study was to explore various spray parameters that could allow the deposition of QC feedstock onto aluminum and stainless-steel substrates.

3.2 Nozzle Design for Polymer Cold Spray

The deposition of polymeric feedstock in the CS process differs greatly from metallic materials. The nature of polymers and their resulting inability to form metallurgical bonds with a metallic substrate leads to bonded coatings relying exclusively on mechanical anchoring. In addition, polymer particles typically have much lower critical velocities than their metallic counterparts [94]. As a result, the use of a supersonic gas flow could be detrimental to deposit polymer feedstock material. For these reasons, the first objective for the polymer solution sought to redesign a CS nozzle to accommodate polymer feedstock. To assess the new nozzle's performance compared to a commercial nozzle, experimental results and computational simulations were used.

3.3 Production of Polymer Coating on Metallic Substrate

Once the nozzle assembly was redesigned, the next objective focused on the deposition of full-size coatings. Spray parameters such as stagnation temperature, stagnation pressure, standoff distance, traverse speed, and powder feeding rate were investigated to observe the effects they have on the deposition of coatings and establish the appropriate spray window. Once the specific spray parameters for this feedstock and substrate combination were determined, coating adhesion was addressed. Various substrate preparation techniques were used to increase the mechanical bonding between the substrate and coating. The deposition of dissimilar materials can lead to a thermal mismatch between the coating and metallic substrate, causing residual stresses within the coating. Therefore, substrate pre-heating was investigated as a mitigation method.

3.4 Hydrophobic Performance of Polymer Coating

Once the PFA coating was successfully produced, the next objective was to characterize the first component of icephobic coatings; namely the wetting behavior. The coating's room temperature wetting behavior was characterized with the static contact angle, determined through the sessile drop method. The wetting behavior was then justified and correlated to surface roughness. To serve as benchmarks, five control surfaces were used to compare the results obtained for the wetting behavior and surface roughness. The materials included two as-received aluminum, ultra-high molecular weight polyethylene (UHMW), polytetrafluoroethylene (PTFE), and bulk PFA.

3.5 Ice Nucleation and Growth Characterization of Polymer Coating

Once the wetting behavior of the PFA coating and all reference surfaces were characterized, the second component of icephobic surfaces was examined. The ice nucleation and growth characterization is an important aspect of icephobic surfaces as it is the middle ground and transition period for the phase transformation of water to ice. The ice nucleation process, and subsequent growth was observed through a timed experiment using a single water droplet, at two different surface temperatures. The droplet's total solidification times were then compared for each surface, indicating their ability to delay ice formation, and correlations were made with temperature, frost formation, and wetting states.

3.6 Ice Adhesion Behavior of Polymer Coating

Once the ice nucleation behavior of each surface was characterized, the interfacial ice adhesion strength of each surface was characterized as the final component of icephobic surfaces. Obtaining the interfacial ice adhesion strength of a surface can be acquired in many ways, however two methods were used in this work: a macro CAT, examining large ice covered surfaces, and a micro shear test, examining the ice adhesion of microdroplets. Ice adhesion strength values were acquired for each surface, including all control surfaces, throughout a number of de-icing cycles. For the macro CAT, 15 de-icing cycles were used and the average of the interfacial ice adhesion strength for each surface was computed. For the micro shear test, 6 de-icing cycles were performed with both cooled samples and room temperature samples being progressively cooled. In addition, using an as-received aluminum surface as the reference material, the ARF was computed for each surface to characterize the reduction in ice adhesion strength.

3.7 Production of Aluminum-rich Quasicrystal Coatings

As the main objective for the metallic solution, the deposition window for QC feedstock on aluminum and stainless-steel substrates was examined. The inherent brittleness of QC materials presents a challenge because plastic deformation is relied upon to produce a coating in CS. The QC powder was deposited using conventional process parameters; however, two brittleness mitigation methods were also studied. The first mitigation method includes pre-heating the feedstock material, to thermally soften the feedstock prior to entering the hot gas. Due to the high brittle-to-ductile transition temperature for QCs, a powder pre-heating system was used, and the resulting deposition of the QC feedstock material was investigated. The second mitigation method involves the addition of a softer feedstock material to create a matrix around the brittle particles, more commonly known in the field as a ceramic-metal, or cermet, coating. Two feedstock composition ratios were used in the second mitigation method to examine the effect on the cermet coating deposition.

4 EXPERIMENTAL PROCEDURES

4.1 Powder materials and substrates

The polymer solution uses a fluoropolymer called adhesive perfluoroalkoxy alkane, or PFA (FLUON® EA-2000 PW50, AGC Chemicals America Inc., PA, USA). Due to material availability, powder flowability requirements with the CS system, and the similar chemical properties as PTFE, PFA was selected for the polymer solution. This powder is irregular-shaped and flaky and has a size distribution of 20-50 μm. The metallic solution focuses on depositing aluminum-rich QC feedstock (CRISTOME A1, Avignon, France), with a spherical morphology and a size distribution of 10-30 μm. The selection of QC feedstock was determined based on specific alloying elements that typically present the most favourable chemical properties for icephobicity [81]. The alloying elements constituting the QC feedstock are shown in Table 2.

Table 2. Alloying elements of QC powder Cristome A1

Element	**Al**	**Cu**	**Fe**	**Cr**	**Si**	**B**	**Zn**
% wt	51.4	17.4	13	15	0.04	0.02	0.01

In conjunction with the QC powder for the production of cermet coatings, the metallic solution also uses aluminum feedstock (SST-A5001, Centerline, ON, CA). This aluminum powder has a size distribution of 5-45 μm and is irregular-shaped to maximize particle velocity. Scanning electron images of powders used in both icephobic solutions are shown in Figure 36.

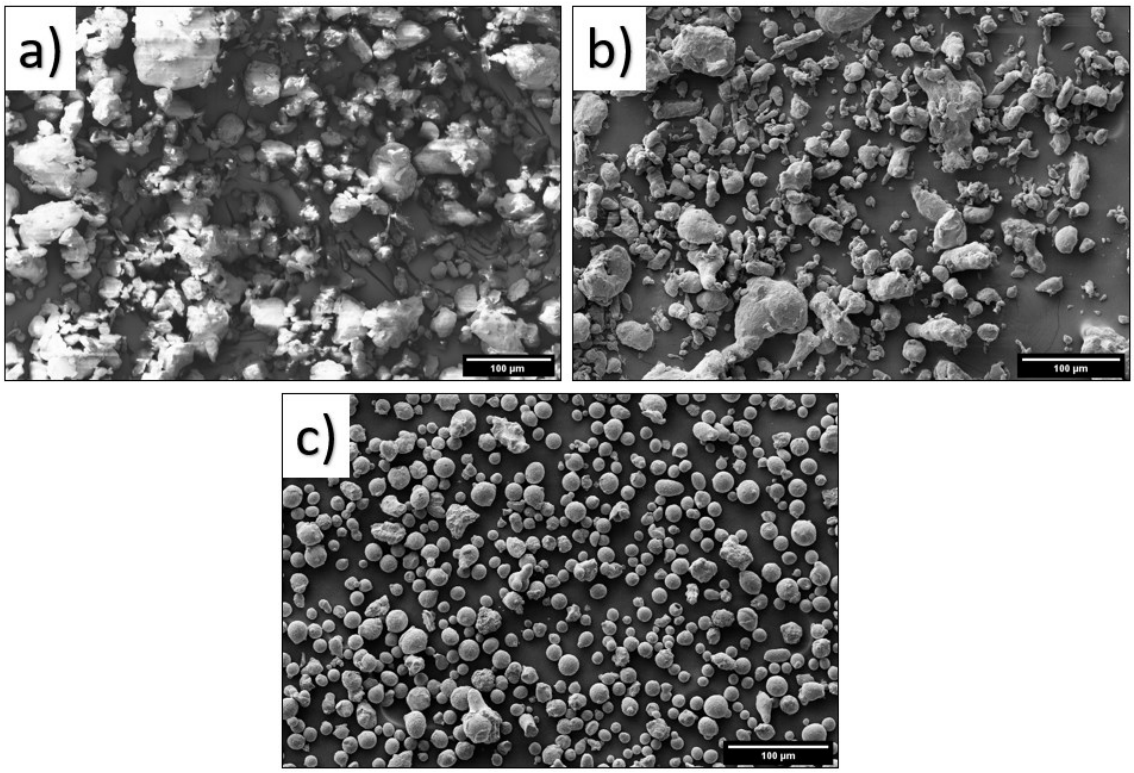

Figure 36. Power morphology of a) Perfluoroalkoxy alkane, b) Aluminum, and c) Quasicrystal

Two substrate materials are used in both icephobic solutions: namely an aerospace grade aluminum alloy (6061-T6), and stainless steel 304. Aluminum alloys are common materials used for aircraft wings, whereas stainless steel is more often used as an erosion shield on components like the leading edge of helicopter rotors. The polymer solution exclusively used aluminum substrates, for its low cost and availability, and were grit-blasted (AG, Ruemelin Manufacturing Company, Milwaukee, WI, USA) prior to depositing the polymer feedstock, using ferrosilicate grit (16 mesh – 20 grit). Grit-blasting was used to increase surface roughness and promote mechanical interlocking with deposited feedstock. To further increase surface roughness than is typically seen with grit-blasting, nitrogen was used at a pressure of 690 kPa. The metallic solution used both aluminum and stainless-steel substrate materials, to examine the effect of substrate hardness and ductility on the deposition of QC feedstock. Substrates were not grit-blasted in the metallic solution due to the deposition of a very hard feedstock material, which would render the surface preparation step redundant due to substrate erosion, and to isolate and observe the impact

behavior of particles without obscured results from grit-blasting. Substrates used in both icephobic solutions were ultrasonically cleaned using ethanol after any surface preparation steps and before depositing feedstock materials.

4.2 Cold Spray System

4.2.1 Gas Heater and Control Unit

This work used a commercially available CS system (SST EP, Centerline Ltd, Windsor, ON, Canada). It consists of a 15 kW gas heater, which can reach a stagnation temperature and pressure of 650 ℃ and 3.4 MPa, respectively. Stagnation conditions are found prior to the beginning of the cold spray nozzle, ahead of the converging section where the gas is assumed to be stagnant. The gas heater is mounted on the robotic traverse system with the stagnation conditions located at the nozzle assembly mounting junction. The stagnation temperature given by the gas heater can be controlled by a touch screen on the system's cabinet, whereas the stagnation pressure can be adjusted with a regulator found near the system. The gas heater and system cabinet can be seen in Figure 37.

Figure 37. SST control cabinet (left) and gas heater (right)

4.2.2 Powder Pre-heater

A custom-made powder preheater was used in the deposition of QC feedstock for the icephobic metallic solution. The pre-heating device consists of mixing the feedstock with

a hot gas for the feedstock to thermally soften prior to entering the CS nozzle. The pre-heating device uses 1.5 m of stainless-steel tubing coiled to a 2 inch diameter with two inlets, for the powder and hot gas, and one outlet for the injection into the nozzle. The hot gas for the powder pre-heater is provided by a gas heater from a commercial pulsed gas dynamic spray system (Waverider, Centerline Ltd, Windsor, ON, Canada). The hot gas, produced by a 14 kW gas heater, can reach a maximum temperature of 900 ℃ and was delivered to the powder pre-heater through an insulated nickel-copper tube. The pre-heater and a system schematic are shown in Figure 38.

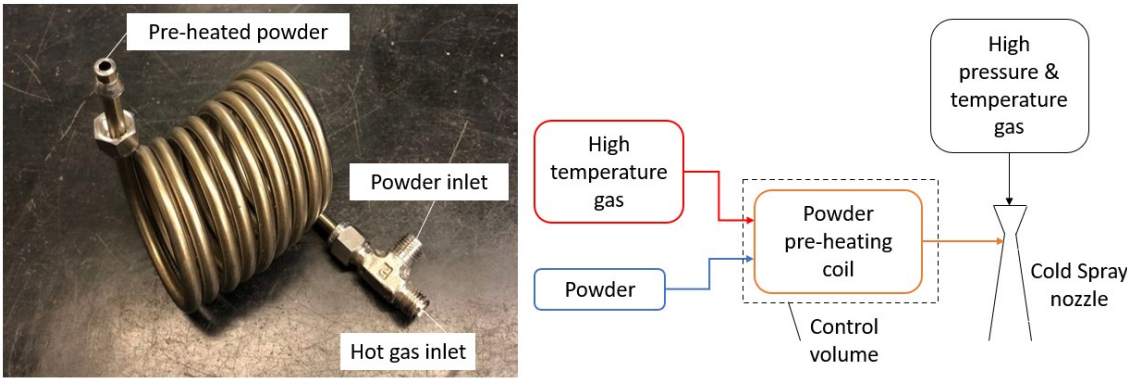

Figure 38. Powder preheating coil (left), system schematic in reference to cold spray nozzle (right)

The desired powder temperature at the outlet of the pre-heating coil was determined using mass conservation and the first law of thermodynamics. This analysis is only looking at the mixing of the nitrogen gasses at different temperatures and different mass flow rates. It is also worth noting that in this calculation the thermal capacity of the feedstock was not accounted for, however since a very small powder feed rate was used (0.0006 kg/s), it is believed that this is a reasonable assumption. The following hypotheses were made, in reference to the control volume of Figure 38:

1. Powder pre-heater is in a steady state
2. There is no change in kinetic energy
3. There is no change in potential energy
4. There is no heat being transferred to or by the system
5. There is no work done by or on the system
6. The nitrogen gas follows ideal gas law

The mass conservation for the pre-heating system is as follows:

$$\frac{dm_{c.v.}}{dt} = \sum \dot{m}_i - \sum \dot{m}_o \tag{17}$$

where $\frac{dm_{c.v.}}{dt}$ represents the change in mass within the control volume as a function of time, $\sum \dot{m}_i$ is the sum of all mass flow rates into the system (in kg/s), and $\sum \dot{m}_o$ is the sum of all mass flow rates out of the system (in kg/s).

Since the system is in a steady state, the mass conservation can be written as

$$0 = \sum \dot{m}_i - \sum \dot{m}_o \tag{18}$$

With two inlets and one outlet, equation 18 can be simplified to

$$\dot{m}_{hot\ gas} + \dot{m}_{cold\ gas} = \dot{m}_{pre-heated} \tag{19}$$

where $\dot{m}_{hot\ gas}$ is the mass flow rate for the hot gas entering the pre-heating coil (in kg/s), $\dot{m}_{powder}$ is the mass flow rate for the cold gas propelling the feedstock powder into the pre-heating coil (in kg/s), and $\dot{m}_{pre-heated}$ is the mass flow rate exiting the pre-heating coil and entering the cold spray nozzle (in kg/s).

The first law of thermodynamics is then used to calculate the required hot gas temperature for a set pre-heated feedstock temperature. The general first law is written as

$$\begin{aligned} \dot{Q}_{c.v.} + \sum \dot{m}_i \left(h_i + \frac{v_i}{2} + g z_i\right) &= \dot{W}_{c.v.} + \sum \dot{m}_o \left(h_o + \frac{v_o}{2} + g z_o\right) \\ &+ \left[\frac{m_2 \left(h_2 + \frac{v_2}{2} + g z_2\right) - m_1 \left(h_1 + \frac{v_1}{2} + g z_1\right)}{\Delta t}\right]_{c.v.} \end{aligned} \tag{20}$$

where $\dot{Q}_{c.v.}$ is the heat transfer by or on the system (in W), h is enthalpy (in kg/kJ), v is velocity (in m/s), g is the gravitational constant (in m/s^2), z is the potential height difference (in m), $\dot{W}_{c.v.}$ represents the work done on or by the system (in W), and Δt represents a change in time (in seconds).

Using the assumptions stated above, equation 20 can be simplified to

$$\left(\dot{m}_{hot\ gas} * h_{hot\ gas}\right) + \left(\dot{m}_{cold\ gas} * h_{cold\ gas}\right) = \left(\dot{m}_{pre-heated} * h_{pre-heated}\right) \quad (21)$$

Based on the assumption that the nitrogen gas follows the ideal gas law, the following relation can be used

$$\Delta h = C_p * \Delta T \quad (22)$$

where C_p is the specific heat for nitrogen (in kJ/kg*K), and ΔT represents a change in temperature (in K).

Substituting equation (22) into equation (21), the following simplified equation is obtained

$$\left(\dot{m}_{hot\ gas} * T_{hot\ gas}\right) + \left(\dot{m}_{cold\ gas} * T_{cold\ gas}\right) = \left(\dot{m}_{pre-heated} * T_{pre-heated}\right) \quad (23)$$

To obtain the targeted feedstock pre-heating temperatures, the mass flow rates and gas temperatures were adjusted until suitable ratios were reached, in compliance with equipment capacities.

4.2.3 Nozzle Assemblies

The two icephobic solutions presented in this work used three different nozzles; a steel nozzle, a tungsten carbide nozzle, and the new nozzle design described in the subsections below. Different nozzle materials were used based on the nature of the feedstock materials being deposited. The new nozzle design was only used with adhesive PFA, the tungsten carbide nozzle was only used for QCs, and the steel nozzle was used with both feedstock materials.

4.2.3.1 Steel Nozzle

The steel nozzle assembly is comprised of four components; the powder inlet, the nozzle holder, the converging-diverging section, and the diverging nozzle extension which is commonly referred to as the nozzle. This nozzle, shown in Figure 39, has a throat diameter of 2 mm, a diverging section length of 120 mm and an exit diameter of 6.6 mm, respectively.

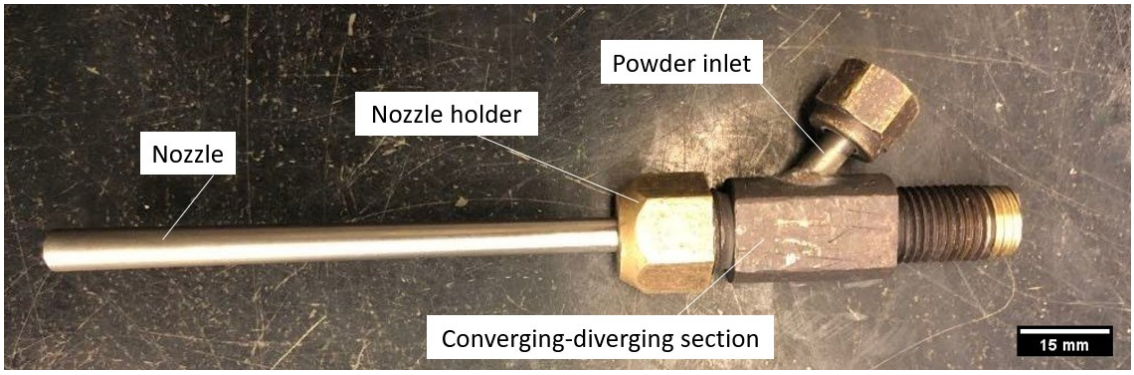

Figure 39. Steel nozzle

4.2.3.2 New Nozzle Design

The new nozzle design is made of stainless-steel, seen in Figure 40, and has three main components: the powder injection assembly, the hot gas inlet, and the stainless-steel nozzle extension. The hot gas inlet acts as the connection between the gas heater and the remaining nozzle assembly. This nozzle assembly does not have a converging or diverging cross-section as seen with the steel nozzle assembly. The nozzle has a length of 151.5 mm and a constant cross-sectional diameter of 4 mm. Details on the design of the stainless-steel nozzle can be found in section 5.1.

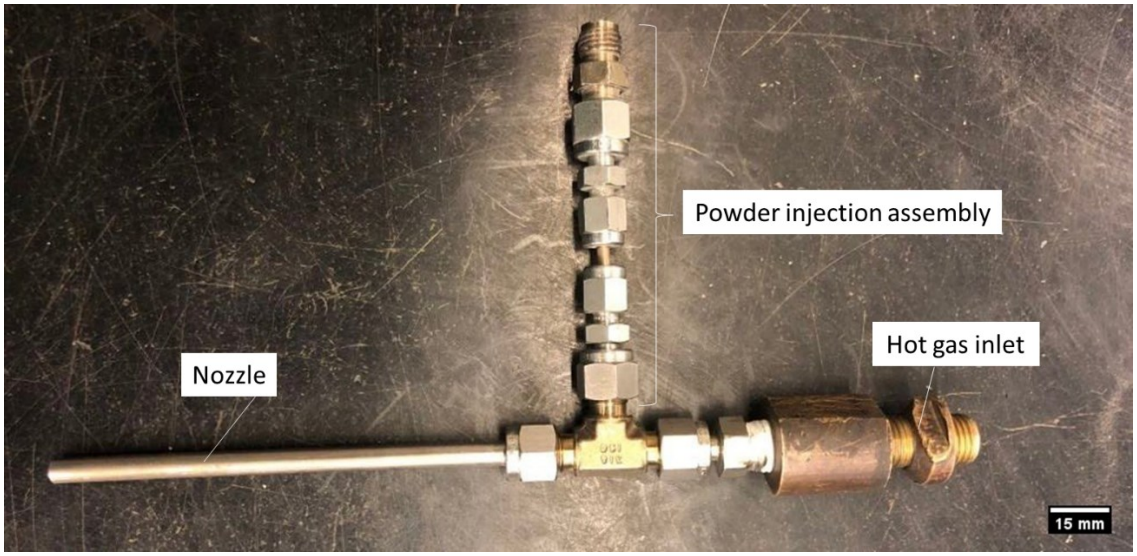

Figure 40. New nozzle design

The powder injection assembly, shown in Figure 41, consists of a powder inlet which is being fed by the powder feeder, and a powder outlet designed to inject the powder at the

mid-stream of the hot gas. The powder injection consists of a 3.175 mm diameter copper tube cut at a 45° angle facing downstream.

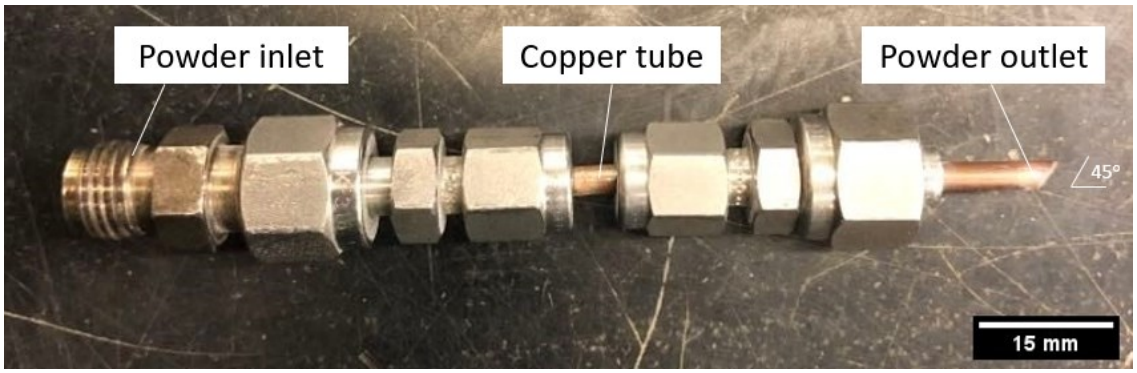

Figure 41. New nozzle powder injection assembly

4.2.3.3 Tungsten Carbide Nozzle

The tungsten carbide nozzle, shown in Figure 42, is used only in the icephobic metallic solution, to deposit QCs on metallic substrates. Like the steel nozzle, the converging-diverging section of the tungsten carbide nozzle acts as the connection between the gas heater and the remaining nozzle assembly. In addition, the powder inlet also injects into the diverging section of the nozzle. The nozzle holder acts as a fastener to keep the tungsten carbide nozzle extension in place. This nozzle has a throat diameter of 2 mm, a diverging section length of 120 mm, and an exit diameter of 6.35 mm, respectively. The tungsten-carbide nozzle was used to deposit QC feedstock in place of the steel nozzle due to the hardness of the feedstock material and the potential to erode the interior steel nozzle walls.

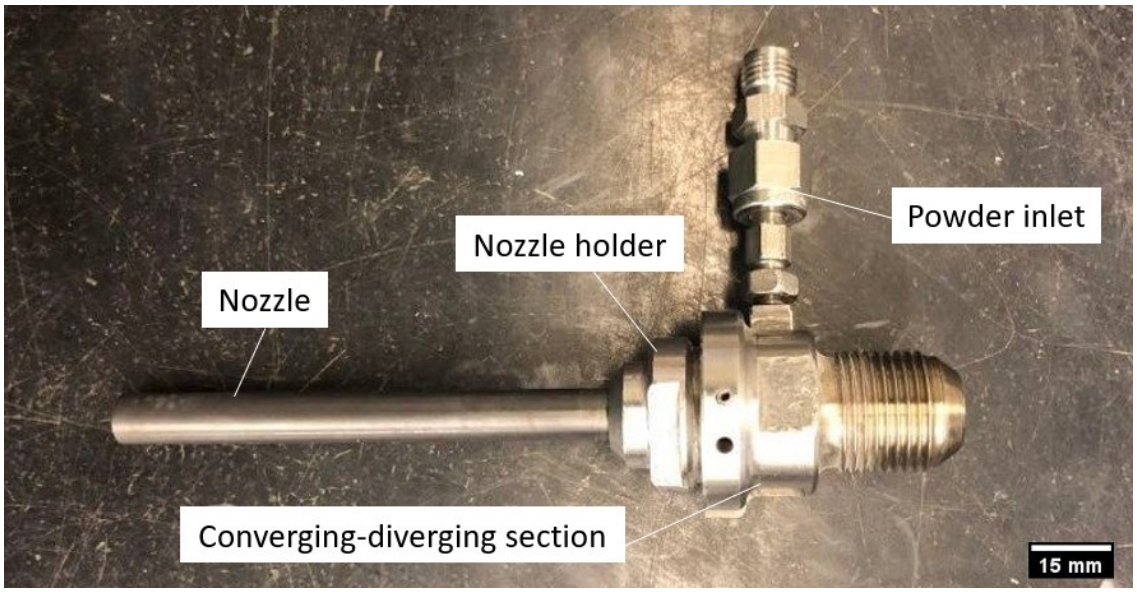

Figure 42. Tungsten carbide nozzle

4.2.4 Robotic Traverse System

The robotic traverse system allows the spray gun to move in a planar motion and is controlled digitally with the system software. The XY traverse system allows the gun to travel over designated substrates at traverse speeds up to 200 mm/s. The robotic system can be seen in Figure 43.

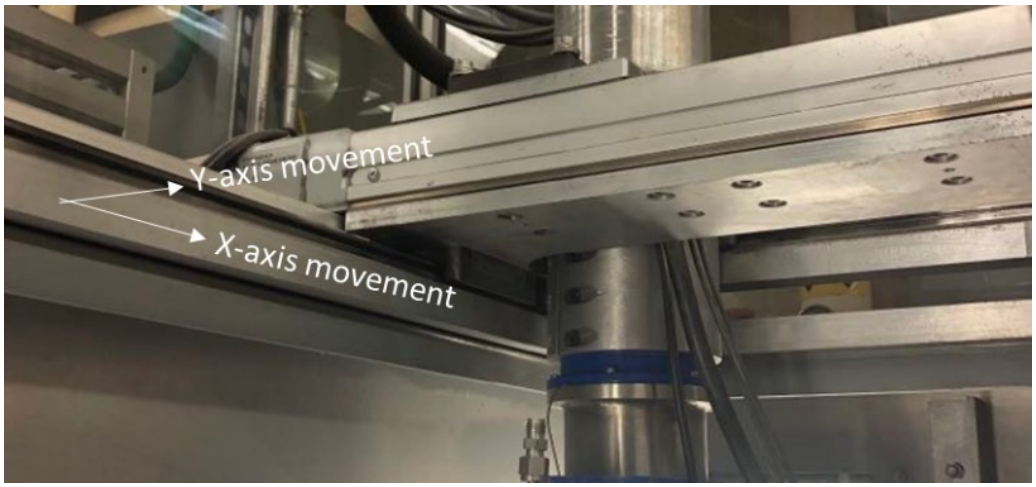

Figure 43. Robotic traverse system

4.2.5 Powder Feeding Equipment

The feedstock powders, for both icephobic solutions, were fed using a commercially available powder feeder (AT-1200HP, Thermach Inc., Appleton, Wisconsin, USA), shown in Figure 44. The powder is contained in a pressurized canister and is fed by a rotating wheel with perforated holes around its circumference. The quantity of powder being fed can be controlled by the angular velocity of the feeding wheel and by the size of the holes on the perforated feeding wheel.

Figure 44. Powder feeding canister (left) and feeding wheel (right)

4.2.6 Spray Chamber

The spray chamber, as seen in Figure 45, houses the robotic traverse system, the spray gun, and the movable X-Z stage for substrates to be placed. The chamber is equipped with a heavy-duty hinged door to protect the user during operation and to provide a safe line of sight. Chamber lights along both sides of the inner walls provide proper lighting while a dust collection system works to safely dispose of any non-deposited particles.

Figure 45. Cold spraying chamber

4.2.7 Strip Heater

Substrate pre-heating, used in the polymer solution, was performed through heat conduction with a strip heater (Omega Environmental, QC, CA), shown in Figure 46. Using a 300W power source (Vishay Instruments Inc, Model BAM1, PA, USA), the 25.4 mm x 200 mm strip heater can reach maximum surface temperatures of 650 ℃.

Figure 46. Strip heater beneath (top) and conducting side (bottom)

4.3 Characterization Procedures and Analysis Equipment

4.3.1 Sample Post-Processing

Sample post-processing begins with the use of a silicon carbide cut-off wheel mounted to a precision saw (Secotom-10, Struers, Mississauga, CA) to cut samples to the appropriate size for examination. Based on material properties, samples can either be mounted in epoxy resin if the material used has a low melting temperature (e.g., polymers) or they can be mounted using a phenolic plastic powder using a hot mounting press (LaboPress-3, Struers, Mississauga, CA). If cross-sectional views of samples are required, mounting the samples followed by grinding/polishing (Tegrapol, Struers, Mississauga, CA) is necessary to obtain a mirror surface finish. Figure 47 and Figure 48 shows the precision saw and polishing machines.

Figure 47. Sample cutting machine

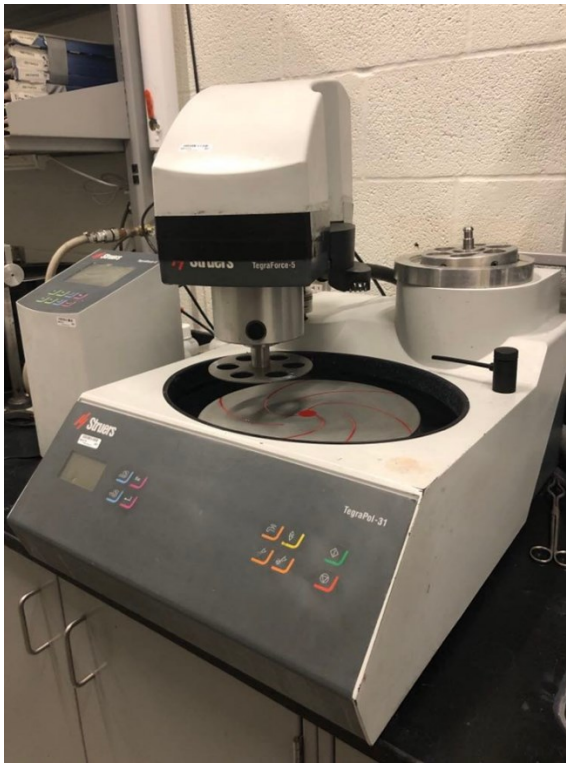

Figure 48. Sample polishing machine

4.3.2 Scanning Electron and Optical Microscope

Scanning electron microscopy (SEM, Oxford Instruments, EVO-MA10, Zeiss, UK) is used to examine surface topography, particle morphology and sample cross-sections. The secondary electron (SE) and back-scattered electron (BSE) signals are used in this analysis.

Material's elemental composition is also determined using energy-dispersive X-ray spectroscopy (EDS), as seen in Figure 49. Samples requiring SEM analysis are placed in a gold-sputtering system (Denton Vacuum, USA) to deposit a thin layer of gold and make the surface conductive. An optical microscope (VHX-2000, Keyence Corporation, Osaka, JP) was used to produce digital images of surface topography and sample cross-sections. The microscope, as shown in Figure 50, can magnify a sample from 100X to 1000X.

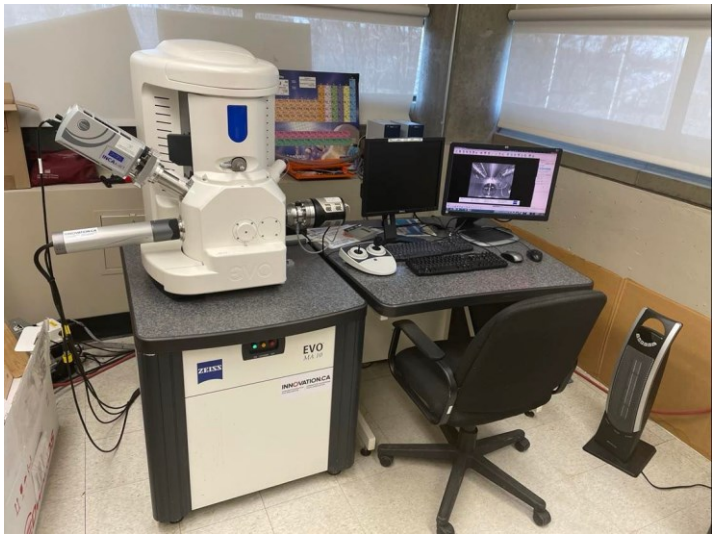

Figure 49. Scanning electron microscope

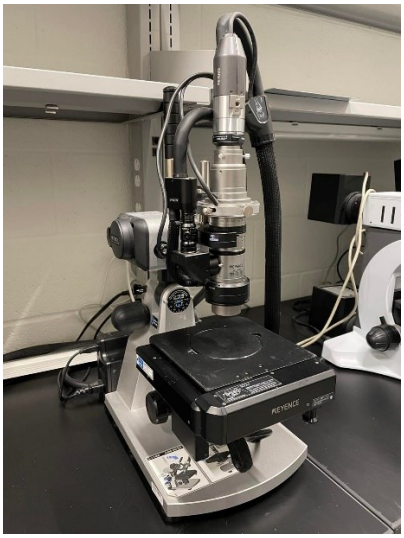

Figure 50. Optical microscope

4.3.3 Surface Roughness Measurements

Surface roughness measurements of coatings and control surfaces were obtained using a profilometer (SRG-4000, Phase II Plus, NJ, USA) equipment with a diamond stylus. Samples are analyzed over a 17.5 mm tracing length and the diamond stylus can measure roughness from 0.005 to 16 µm with 0.001 µm accuracy.

4.3.4 Goniometer System

A goniometer system, shown in Figure 51, was used to obtain static contact angle measurements using the sessile drop method [95]. Analysis requires the placement of the surface on a high-precision motion stage (Benchtop XYZ Motion System, Aerotech Inc., PA, USA). A computer-controlled micro-syringe is used to produce a 10 µL water droplet. Digital images of the side view of the droplet are captured by a USB microscope camera and backlighting of the droplet is provided by a LED light source (MNWHL4 LED,

Thorlabs, NJ, USA). Contact angle measurements are obtained using the ImageJ software plugin.

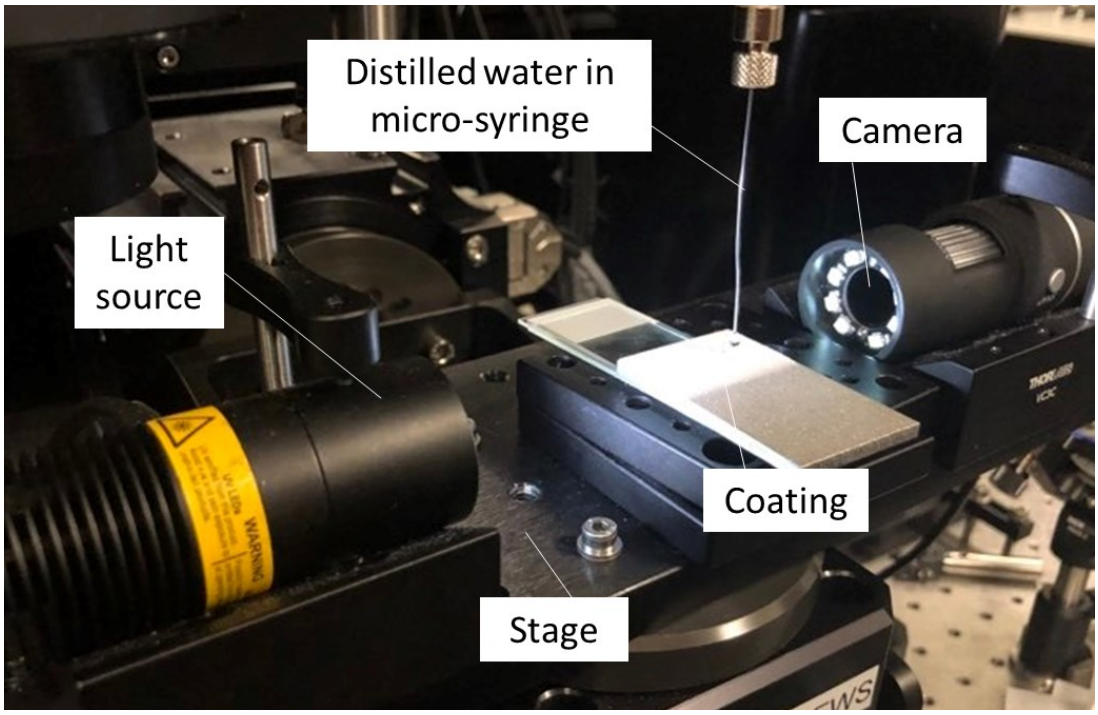

Figure 51, Goniometer system for sessile drop method

4.3.5 Ice Growth and Droplet Pusher System

4.3.5.1 Cryostage

Observation of the ice growth process, for water droplets placed on cooled test surfaces, was performed using a cryostage, as seen in Figure 52. The cryostage uses a programmable thermoelectric cooler (TEC) (S3 Series 800, Omega Instruments, QC, CA). The unit is coupled with a heat sink to draw heat away from its surface and thus reduce the surface temperature. A water bath (Thermo NESLAB, Marshall Scientific, NH, USA) placed underneath the TEC is used as the heat sink. Temperature of the TEC is held at -10. 0 ℃ ± 0.1 ℃ and monitored using an embedded thermocouple. Two different environmental icing conditions were used for the samples to observe the effect frost formation and wetting states would have on ice growth. The first method stored and pre-cooled test surfaces in a commercial freezer at -4 ℃ and then individually placed them within the cryostage allowing them to cool for an additional 5 minutes to reach equilibrium. This method will be referenced as the isothermal substrate. The second method involved placing samples at

room temperature directly on the cryostage, without any equilibrium time. This method will be referenced as the cooled substrate. For both icing conditions, a 10 µL distilled water droplet was placed on the test surface with a micropipette. A chilled needle, kept on dry ice, was used to mechanically prompt the initiation of nucleation of the water droplet if nucleation did not occur naturally. To observe the freezing process of a single droplet, a high-resolution digital camera (Nikon OEM), fitted with a 35 mm lens, was used in conjunction with a compound microscope. The camera has a working distance of 0.2 m, an aperture of 2 and, to get a closer look at the droplet, used a 7 mm spacer ring. An exposure between 5 to 25 µs was used depending on the degree of refracted light on the test surface in order to regulate image brightness captured by the camera. Video processing was done with the NIS Elements D software to visually extract ice growth times.

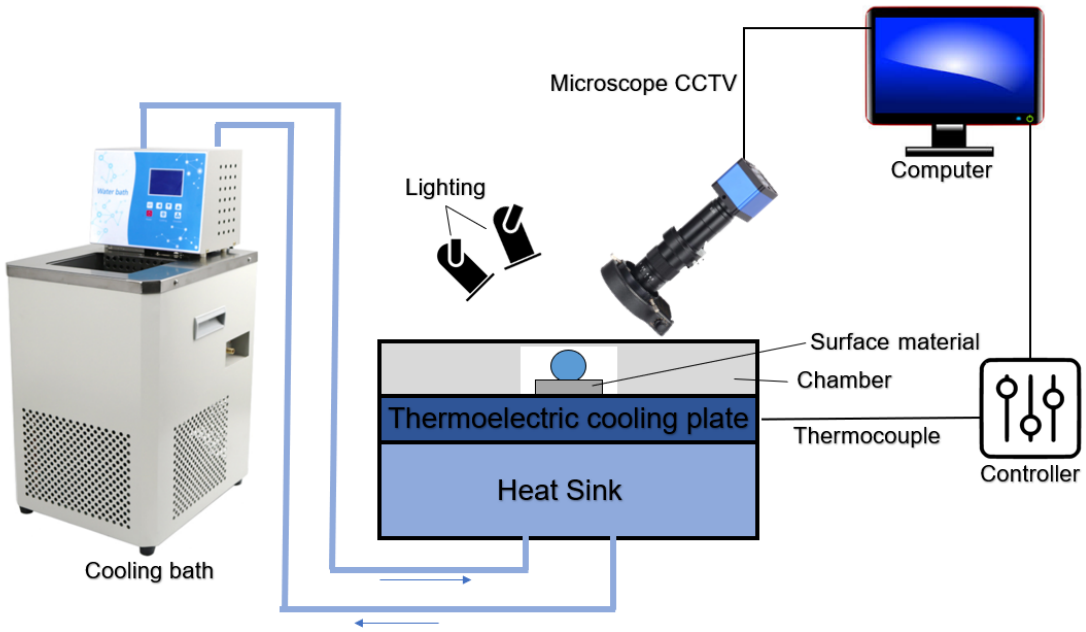

Figure 52. Cryostage experimental equipment

4.3.5.2 Droplet Micro Shear Tester

Characterization of the adhesion strength of frozen water droplets was performed by a custom-built droplet pushing system. The droplet pushing assembly, shown in Figure 53, consists of a base plate which supports the cryostage unit along with a dovetail rail system housing the load cell and push rod. A 1000 g ± 1 g compression load cell (REB7, Loadstar sensors, CA, USA) is fitted with a steel pushing rod which descends into the cryostage and

onto the test surface. Pushing rods are kept on dry ice at approximately -78 ℃ prior to testing to avoid melting the solidified water droplet upon contact. A manually controlled micrometer is used to incrementally push the top dove-tail assembly, containing the load cell and droplet pusher, against a solidified water droplet. Data received by the load cell was monitored through the LV-1000 software, provided by the manufacturer, at an acquisition rate of 10 Hz. Ice adhesion was obtained using the peak load experienced by the load cell prior to detachment. The pushing rod is mounted to the load cell in a cantilever position, which resulted in load cell readings being calibrated at 83% of actual loads. As a result, all values used to quantify surface ice adhesion were adjusted accordingly.

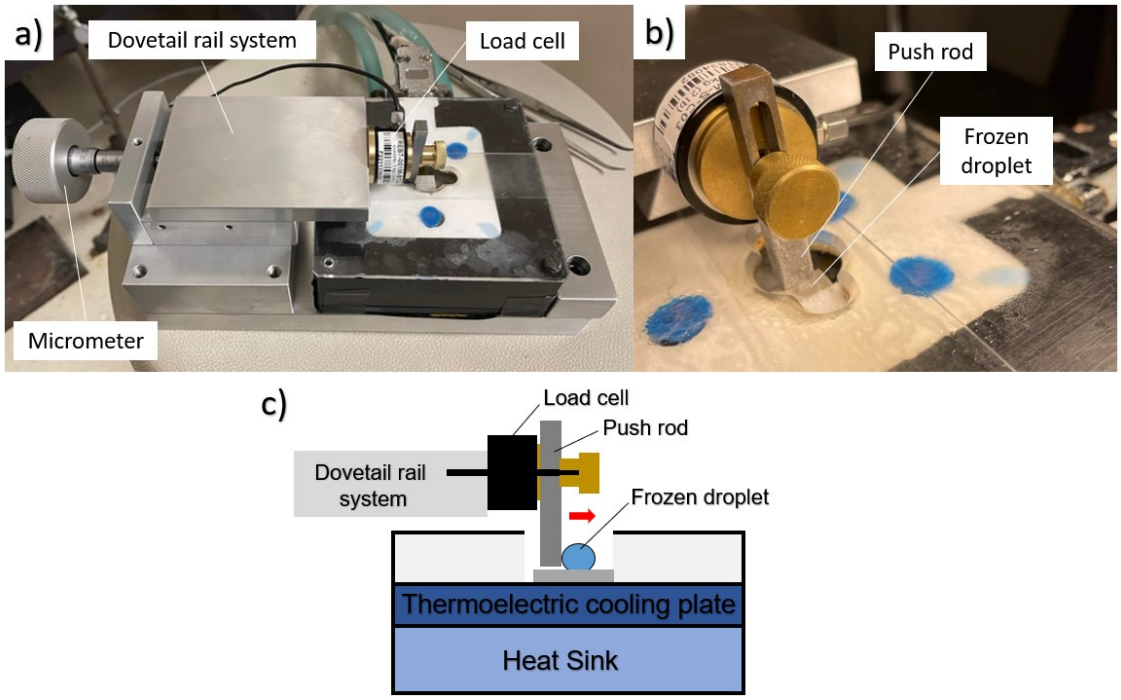

Figure 53. Droplet pusher: a) Overall assembly, b) Push rod and load cell image, and c) System schematic

4.3.6 Climatic Ice Adhesion Test Chamber

The Climatic Ice Adhesion Test Chamber's (CIATC) uses the same principles as a conventional CAT to obtain an interfacial ice adhesion shear strength. However, calculations accounting for the tangential force exerted on iced samples can be found in Appendix - B. Description of a CAT and its principles is explained in section 2.6.1. Details of the CIATC's equipment and functions are given in the current section.

4.3.6.1 Rotor

The rotor used in the CIATC is a 254 mm long and 3.175 mm thick flat bar with a width of 31.75 mm. The rotor's material is interchangeable; however dimensions must remain the same. Aluminum 6061-T6 is used in this work. On the first end of the rotor is the designated area for the ice cube to be statically formed. This end of the rotor is treated as a conventional CS substrate or can mount any other control surface and will later mount the ice cube. The other end of the rotor is fitted with a counterweight of equal mass and position as the ice cube and any other material weight. The counterweight can be made of either metallic material, granted the weight balances itself, and is secured to the rotor via an aluminum rivet, shown in Figure 54. The iced rotor assembly is mounted on the shaft at its midpoint using a standard sized hex bolt and lock-washer. A tapped hole within the shaft allows for mounting the flat rotor on its end point.

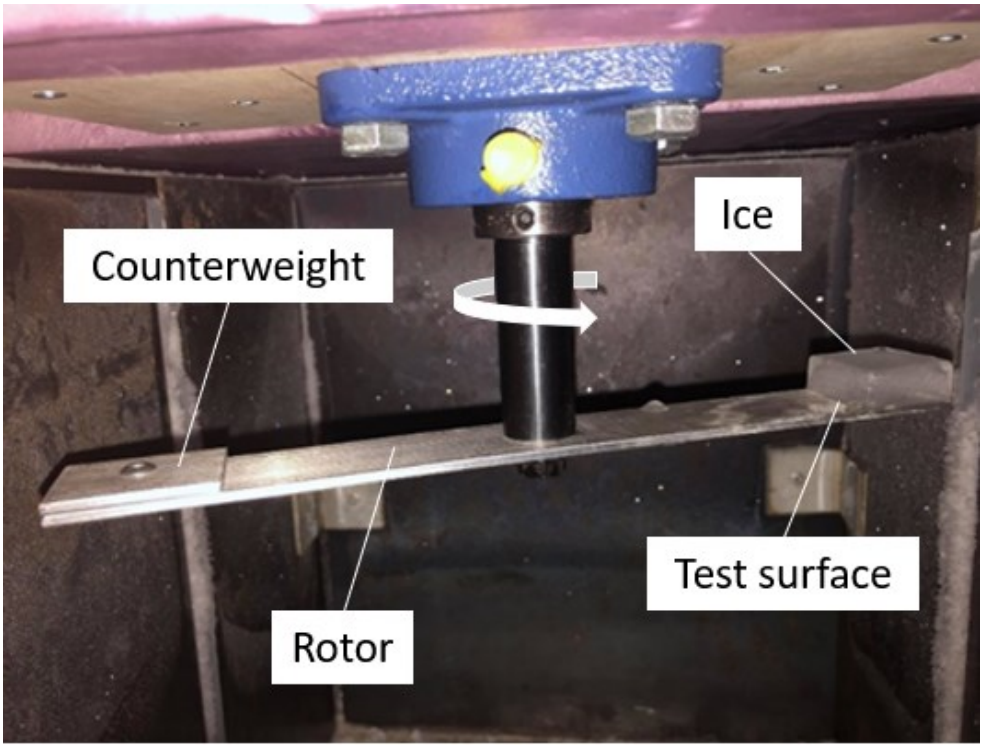

Figure 54. Mounted rotor for CAT

4.3.6.2 Ice Production

Icing the rotors is done using a silicone ice cube tray, with five available ice cube prisms on the tray. A wooden platform supports the rotors during their icing cycle and clamps are

used for stability and height consistency, shown in Figure 55. Rotors are placed face down in the ice cube trays. Distilled water is inserted in each ice cube prism until they are filled. The entire assembly is then placed inside the climatic chamber for the water to solidify. The iced rotor, as seen in Figure 56, is then removed and turned right side up with the shown dimensions.

Figure 55. Ice production assembly

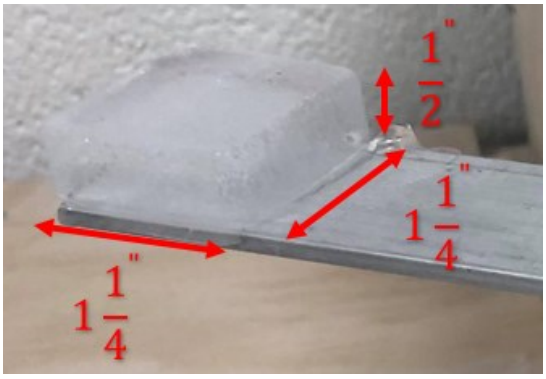

Figure 56. Ice cube dimensions

4.3.6.3 Climatic Chamber

The climatic test chamber uses the cooling system and general structure of a 5.5 cubic feet commercial chest freezer. The lid on the climatic chamber was replaced with an insulated wooden structure to allow mounting mechanical components and houses an access door. The wooden lid is secured on the freezer using two ratchet straps, pulling underneath and on both sides of the chest freezer. The wooden lid is also mounted to the wall using two heavy duty steel brackets and multiple screws to avoid vibrations during operation that would otherwise interfere with the rotor vibration signal. Figure 57 and Figure 58 present the chest freezer, mounting brackets and ratchet straps.

Figure 57. Mounting brackets for chest freezer

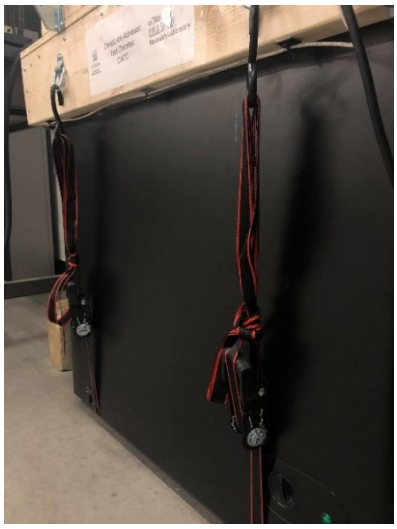

Figure 58. Securing straps for chest freezer

Figure 59 shows the wooden lid assembly complete with the shaft and ball bearing locations, along with the access door. The access door is large enough for the operator to mount a rotor and for the ice production assembly to be placed inside the chamber. Underneath the wooden lid and the access door is 2-inch solid insulation to ensure freezing temperatures are controlled.

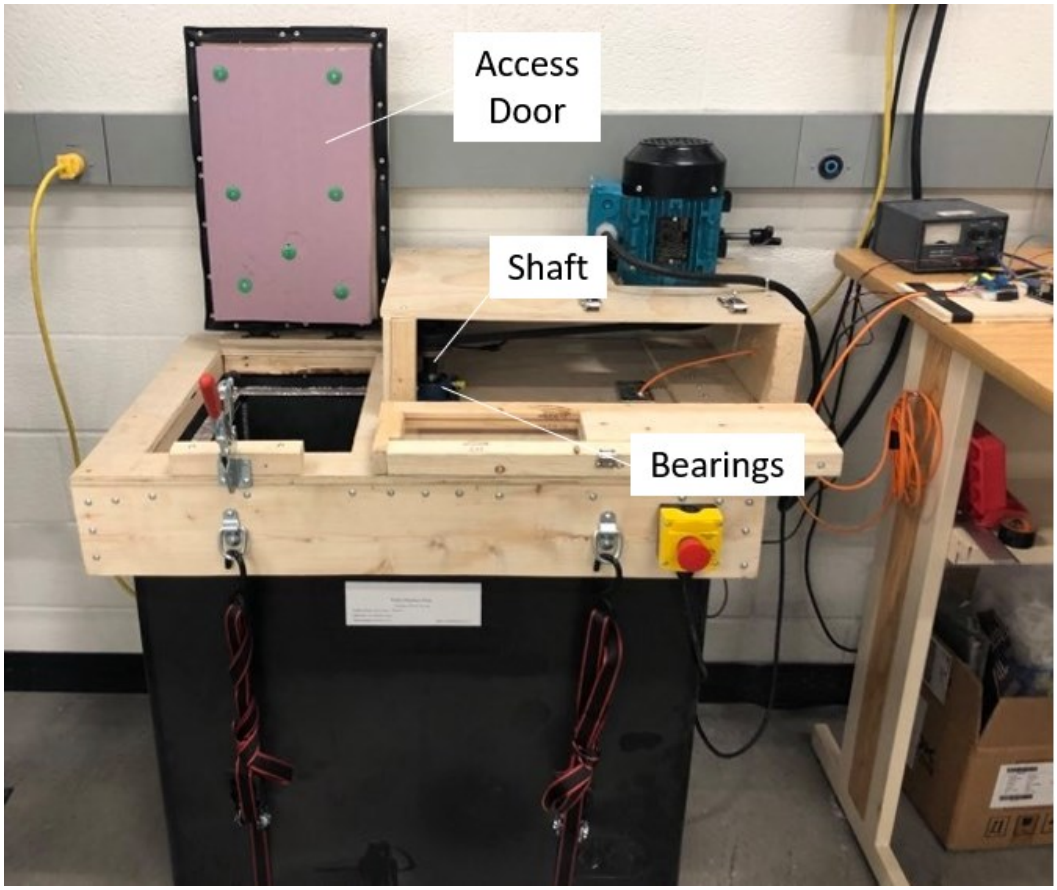

Figure 59. Wooden lid asssembly of CIATC

4.3.6.4 Thermocouples

Two thermocouples are used in the climatic chamber. The first is a household thermometer (TP49-B, ThermoPro) mounted on the wall of the chamber in front of the access door, as shown in Figure 60. This sensor provides a digital reading of the temperature and serves as a benchmark for the calibration of the second thermocouple. The second thermocouple (ITC-308, Inkbird) is placed on the right side of the freezer, shown in Figure 61, and is connected to a controller capable of keeping the temperature within one degree Celsius of the target temperature. The controller turns the freezer on and off to maintain the target temperature.

Figure 60. Access door temperature sensor

Figure 61. Controlling thermocouple

4.3.6.5 Vibration Sensor

The adhesion strength calculation requires a signal allowing accurate assessment of when the ice detaches from the rotor. This is done using a vibration sensor. The vibrations are captured by a corrosion resistant accelerometer (3738T1, McMaster-Carr, IL, USA) and it is mounted on the side of the bottom flange bearing inside the climatic chamber, seen in Figure 62. The sensor is mounted in that position to capture all radial vibrations caused by the rotational imbalance of the shaft once the ice has detached. The information captured by the sensor is sent to the Arduino controller and converted into frequency values ranging from 10 to 1000 Hz. The Arduino code used for vibration calculation can be found in Appendix - A.

Figure 62. Vibration sensor mounted on the flanged bearing unit

4.3.6.6 Safety Features

The CIATC is fitted with different safety features for the protection of the user. The first is the use of an emergency stop button, shown in Figure 63 to cut the power to the electric motor. The button is mounted on the front of the machine and is at hip's height for convenience in the case of an emergency.

Figure 63. Emergency stop button

Furthermore, a magnetic door fail safe is mounted on the left side of the access door. The contact of the magnets allows the motor to function, but when the door is opened enough for a hand to fit inside the chamber, it cuts all power to the motor (shown in Figure 64).

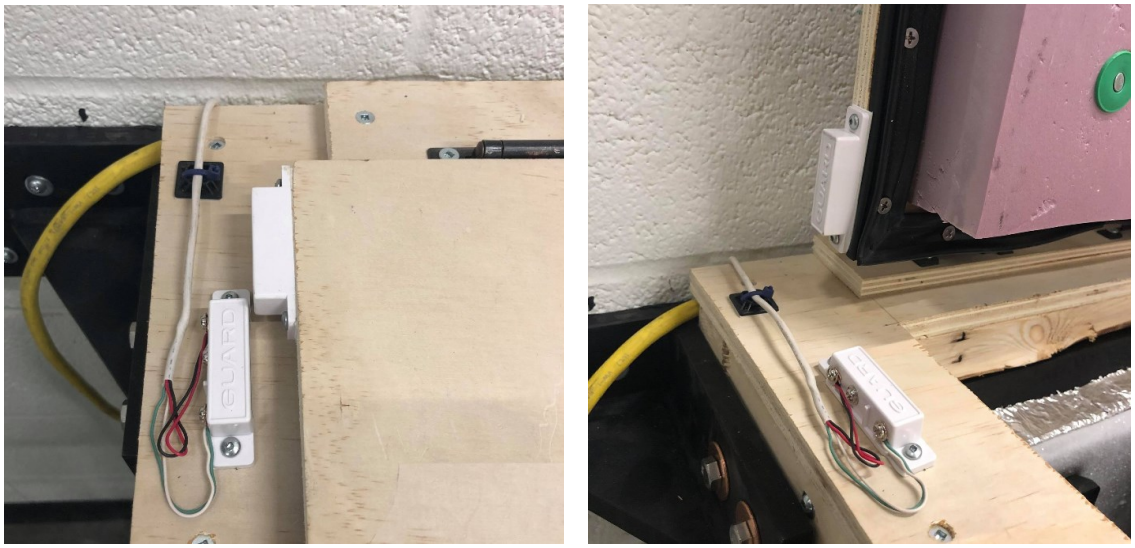

Figure 64. Magnetic safety for CAT

A second feature protecting the user from moving parts is the sheave and belt guard on the top of the climatic chamber, shown in Figure 65. Access to the area is still available with a door on the front of the guard.

Figure 65. Motor and belt guard with access door open (left) and closed (right)

The final safety precaution is inside the climatic chamber. Steel plating was installed on each interior wall to serve as a ballistic shield against high velocity ice projectiles or in the event of a mechanical failure, shown in Figure 66.

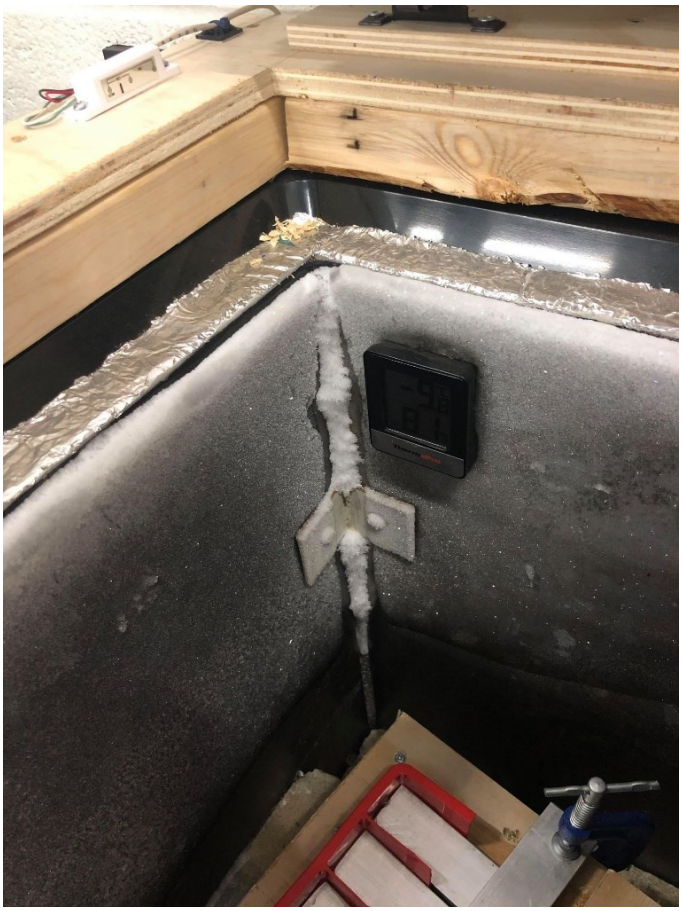

Figure 66. Steel plating inside CAT assembly

4.3.6.7 Electric Motor and Variable Frequency Drive

The motor used in the CIATC is a 1 horsepower AC motor (BC-BF2N001-2C, Brook Crompton, CA). Capable of going up to 3600 rotations per minute (rpm), it drives a large sheave, which in turn transmits the power to a smaller sheave by a v-belt. As a result, the smaller sheave, which is driving the shaft, can reach rpm's of around 7000. Allowing the rotors to reach such high rpm values simulates more closely tip speeds of helicopter rotors or aircraft wings in flight. Belt tension has also been considered and can be adjusted with the use of a tilting motor base, shown in Figure 67. The electric motor is controlled using a variable frequency drive (VFD, EEC-ODE-3-1200-43-1F1B, Invertek, ON, CA), seen in Figure 68. The VFD changes the supplied frequency to the motor from 0 to 60 Hz, on a 45 second ramp up interval. Instructions on VFD functions can be found in the safe operating procedures mounted on the side of the CIATC. The rpm values used in the calculations of ice adhesion strength are derived from the VFD's voltage output. The VFD provides the voltage output to the Arduino controller and the values are mapped to the motor's theoretical RPM and finally multiplied by two to account for the sheave increase seen at the shaft and subsequent rotor. The Arduino code used for rpm mapping can be found in Appendix - A.

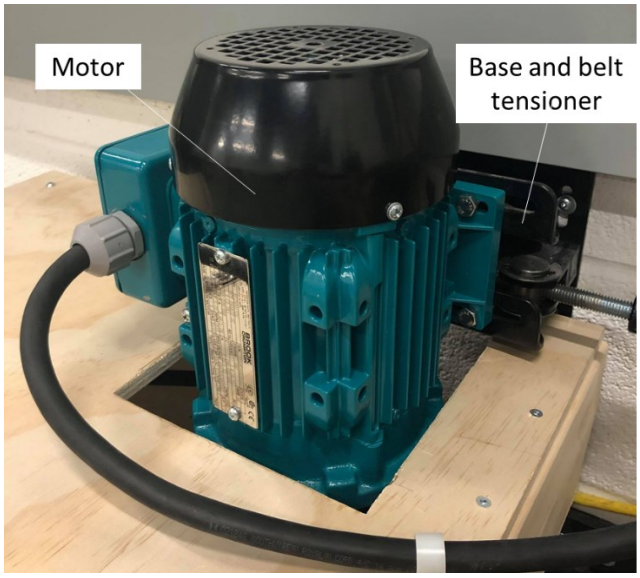

Figure 67. Electric motor and adjustable motor base for belt tensioning

Figure 68. Variable frequency drive unit

4.3.6.8 Arduino Hardware

The VFD, used for the tachometer, and the vibration sensor both send their outputs to an Arduino Uno controller for calculations and for data exportation, shown in Figure 69. The vibration sensor uses an external power source as it requires more voltage, as seen in Figure 70. The Arduino code, as previously described, can be found in Appendix – A.

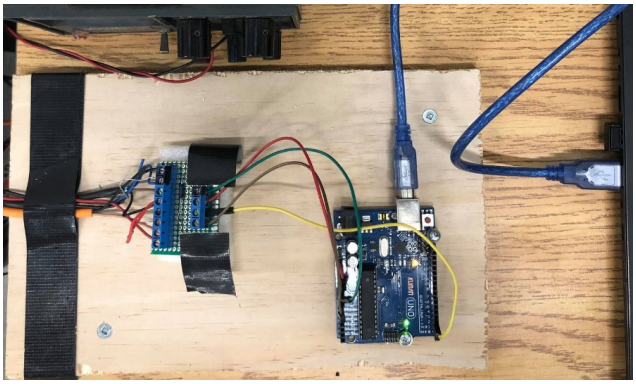

Figure 69. Arduino control board for CAT

Figure 70. Power source for vibration sensor

5 RESULTS

This chapter presents the results of two potential icephobic coating solutions. The first being a polymer coating applied on a metallic substrate, and the second being a metallic coating applied on a metallic substrate. The polymer solution is written as a research article and has been published as a peer-reviewed journal paper.

5.1 Polymer Solution

The first icephobic solution presents the cold spray deposition of adhesive perfluoroalkoxy alkane (PFA) onto aluminum 6061-T6 alloy substrates, and the icephobic performance of the as-sprayed coating. The deposition of the fluorinated polymer was achieved through redesigning the nozzle and powder injection geometries, thus tailoring the gas flow for polymer feedstock. Experimental work demonstrated increased deposition and coating quality when using the new nozzle design, and numerical modelling was used to confirm flow-physics. Coating characterization was then carried out to examine porosity, coating thickness and overall quality of the coating. The wetting behavior was then evaluated for all surfaces using their static contact angles, and the as-sprayed PFA coating displayed a superhydrophobic behavior. Ice nucleation behaviors and growth times were then characterized at two different temperatures to examine the effects on frost formation, on the wetting behavior and to determine the surface's ability to delay complete solidification. Computational modelling of droplet freezing was performed in this work to further understand the effects of surface temperature and nucleation; however this was entirely carried out by co-author Dr. Aleksandra Nastic. Lastly, icing behavior was then assessed in a macro centrifuge adhesion test and micro single droplet shear test, characterizing ice adhesion.

Manufacturing and Icephobic Performance Evaluation of Cold Sprayed Adhesive Perfluoroalkoxy Alkane Coatings

Z. Leclerc[1], L. E. McMunn[2], A. Nastic[3], R. N. Ben[2], B. Jodoin[1]

[1]University of Ottawa Cold Spray Research Laboratory, Ottawa, ON, Canada

[2]Faculty of Science, University of Ottawa, Ottawa, ON, Canada

[3]Department of Mechanical and Industrial Engineering, University of Toronto, Toronto, ON, Canada

Abstract

There is an increasing need for ice protection systems that do not require complex manufacturing considerations or are energy intensive. Fluorinated polymer coatings are potential candidates for such systems although conventional manufacturing processes can be costly, limited in the achievable coating thickness or can degrade the coating's material mechanical properties during deposition. The current work aims to offer an alternative approach by using cold spray as the mean of coating production. Computational and experimental approaches are used to design a new cold spray nozzle for the efficient deposition of adhesive perfluoroalkoxy alkane. The icephobicity of as-sprayed coatings are evaluated using three-fold characterization, one for each stage of the icing process. First, the surface's wetting behavior is established using single droplet analysis, followed by a time-lapse study of water droplets to observe their freezing process, and finally ice adhesion is evaluated with both macro and micro ice adhesion tests. While the as-sprayed coatings exhibited superhydrophobic properties that should be sought in icephobic coatings, their behavior changed when exposed to frost formation. Ice adhesion testing revealed that surface frosting leads to degraded wetting behaviors resulting in much higher ice adhesion, which demonstrates the importance of this phenomena when studying icephobic coatings.

Keywords: Cold Spray, PFA, superhydrophobic, icephobic, CFD

Introduction

Preventing ice accretion is a challenge in many industrial sectors such as aerospace [1], power generation [2]–[4], marine [5], energy transportation [6] and building construction [7], [8]. Ice accumulation can be detrimental by preventing proper operation leading to a decrease in performance, disruption in aerodynamics, increased weight, reduction in reliability, and increased safety risks [1], [2], [4], [9]. Ice mitigation systems include various de-icing and anti-icing methods; however, systems currently used are exclusively active. These systems require thermal, pneumatic or chemical energy to operate, making them less desirable because of their high maintenance and increased overall weight. Passive systems however, typically in the form of coatings, use their material physical properties to protect surfaces from ice formation and/or accumulation without the use of external energy sources. These coatings, normally referred to as icephobic, can operate by 1) presenting hydrophobic properties preventing liquid droplet accumulation; 2) slowing down the freezing process, and 3) demonstrating very low ice adhesion [10], or taking advantage of combinations of these features.

While there are many important properties an icephobic coating should possess, such as durability, porosity level and coating adhesion, equal importance should be given to the coating's interface topology interacting with water and ice. Surface types used in icephobic applications can vary from very rough, such as superhydrophobic surfaces (SHS) [11]–[14], or very smooth, such as slippery liquid infused porous surfaces [15]–[18], or viscoelastic surfaces [19], [20]. Rough SHS have shown promising icephobic potential by reducing overall ice adhesion strength and delaying overall ice nucleation/growth times [13], [21]–[23]. SHS impart a unique behavior for water droplets by reducing the contact area at the solid-liquid interface which results in droplets resting above surface features, commonly referred to as the Cassie wetting state [24]. Maintaining a superhydrophobic Cassie state allows water droplets to roll-off or in some cases bounce off a surface, thus reducing the overall quantity of liquid droplets remaining on the cold surface and reducing the probability of attachment through solidification. Despite this, it has been shown that the unique surface features which give the SHS its Cassie wetting state can be quite fragile in humid environments resulting in compromised icephobic properties [25], [26]. The

intricate surface features of SHS can serve as nuclei initiation sites for frost growth causing the Cassie wetting state to be lost and the water droplet to completely wet the surface. Upon complete surface wetting, known as the Wenzel state, the droplet's solid/liquid interface is increased leading to more heat being transferred to the cold surface and accelerating the ice growth process [25]. As such, the use of SHS as icephobic coatings relies primarily on maintaining the Cassie wetting state and minimizing frost growth on its surface.

The solidification of water on structures exposed to atmospheric icing has commonly been examined as a macroscopic problem. However, the microscopic transition of single water droplets can be viewed as the root issue to be studied. As shown in Figure 1, when a single water droplet contacts a cold substrate, it undergoes four freezing stages; (1) pre-cooling or supercooling, (2) recalescence, (3) freezing, and (4) cooling [27]–[29]. For supercooled droplet, the freezing process starts when subjected to a small external disturbance. First, the temperature of the droplet decreases from its initial temperature (room temperature) to a nucleation temperature (below the equilibrium freezing point), which marks the start of the recalescence stage. The supercooled state drives rapid kinetic crystal growth from the crystal nuclei. The latent heat released from the ice generates an abrupt increase in temperature up to the phase change temperature (solidification temperature). The duration of the recalescence stage is very short, at the millisecond level, and dependent on the volume of water. During this stage, the supercooling state drives the rapid crystal growths from crystal nuclei until the droplet has reached an equilibrium freezing temperature. At the end of the nucleation/recalescence stage, the droplet consists of a water-ice mixture. This marks the start of the subsequent freezing stage, which is governed by the rate of heat transfer to the surrounding environment/substrate. During freezing, the temperature is constant at the solidification phase change temperature. Once the droplet is frozen and upon further cooling, the droplet temperature will start decreasing, which marks the beginning of the fourth stage, as shown in Figure 1. Understanding the freezing process and finding aspects that can be controlled by coating properties could offer new avenues to explore in the development of icephobic coatings.

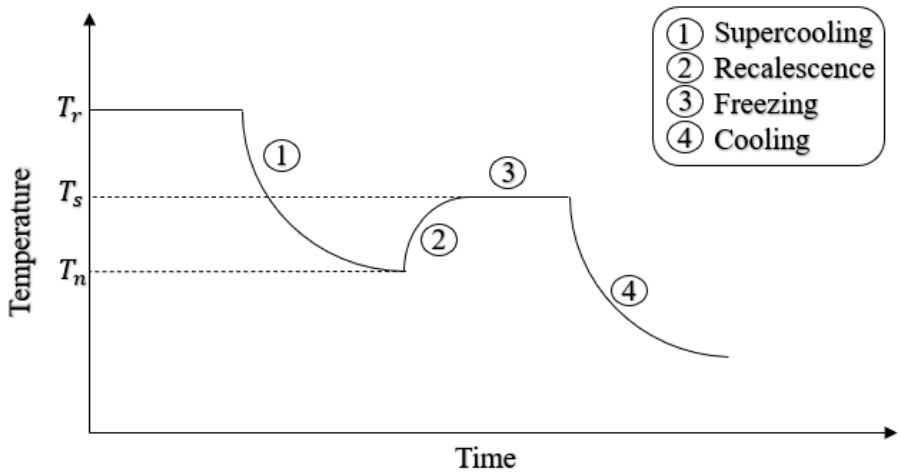

Figure 1. Droplet temperature transition of the four freezing stages. T_r represents the room temperature, T_s represents the solidification temperature, and T_n represents the nucleation temperature.

Current works on icephobic surfaces involve a variety of polymers mainly for their low cost, hydrophobic nature and chemical properties relevant to icephobicity: low dielectric constants and low surface free energy [7], [14], [36]–[39], [19], [20], [30]–[35]. Polymer coatings can be applied using different methods, such as brushing/rolling, electrostatic spraying and dipping [40]. However, these methods require precise chemistry, can be expensive and/or are typically limited by the thickness they can achieve [40]. The development of polymer coatings for hydrophobic or icephobic applications is commonly carried out by thermal spraying methods, most commonly flame spray [30], [33], [41], [42]. Flame sprayed polyethylene coatings on aluminum and stainless-steel substrates have been reported to have promising anti-icing behavior [30]. Nevertheless, the effectiveness of this deposition method relies on carefully tuned spray parameters, which include high processing temperatures [41], [43]. The feedstock material is injected into the flame, resulting in molten or semi-molten particles being propelled toward the substrate [43]. Such elevated temperatures can result in degradation or burning of the polymer feedstock material and it has been reported that similar decay of the substrate can occur when depositing on composite materials [44].

Cold gas dynamic spray or cold spray (CS), commonly used to produce metallic/cermet coatings, has been proposed as a manufacturing method for the production of polymer coatings [43], [45]–[50]. The CS process relies on gas dynamics principles to accelerate a gas flow to supersonic velocities and propel solid powder particles towards a substrate, where plastic deformation of the solid particles and substrate occurs and a coating is created upon impact with the substrate [43], [51], [52]. CS differs from other thermal spray processes as it is a solid-state process, thus preserving the feedstock material microstructure and properties [51]. It was recently reported that superhydrophobic perfluoroalkoxy alkane (PFA) coatings can successfully be deposited on stainless-steel substrates using CS [47] while exposing the challenge of depositing PFA particles due to the low surface energy of fluoropolymers. As such, substrate laser texturing was required to increase particle-substrate adhesion as well as the addition of fumed nano alumina (FNA) to the feedstock material [47], serving as a binding agent/filler. This approach improved mechanical properties, thermal properties and promoted adhesive bonding with the substrate [49], [53]–[57].

Adhesion mechanisms for polymers in the CS process differ from metallic particle deposition. The absence of metallic bonds for polymers in the CS process implies that bonding can occur solely through mechanical interlocking. Such a bond occurs when the sprayed particles deform on the substrate topography and infiltrate surface asperities, creating physical anchoring between the coating and the substrate [58]. This adhesion mechanism relies on the substrate surface roughness to allow initial bonding of the first layer, and therefore substrate surface preparation, such as grit blasting, is typically required [59]. In addition, it has been reported that improving the adhesion of the coating/substrate interface can be achieved with substrate pre-heating [60]–[63]. It was reported that polyolefin powder could not be deposited on room temperature aluminum substrates, but when the substrate was pre-heated significant deposition was observed [63]. Substrate preheating is also said to relieve thermal stresses of the coating, which is especially important when depositing dissimilar materials [62], as thermal stresses induced in the coating can cause peeling or complete delamination from the substrate [64].

Interparticle bonding, or cohesive bonding, can also be a challenge when cold spraying polymers. Just as the particle-substrate interface lacks metallic bonding, cohesive bonding of polymer particles faces the same issue. It was reported that a variety of polymers, including high-density polyethylene, polyamide-12, polyurethane and others, all failed cohesively when deposited on polymer substrates [48]. In the CS deposition of polyolefin powder on aluminum substrate, it was claimed that the thermal effects during particle impact are responsible for the cohesive bonding of polymer particles [63]. Although general melting of the feedstock does not occur in the CS process, the plastic deformation of the particle from the impact, coupled with thermally assisted interdiffusion, is believed to lead to interparticle bonding [63]. The bonding mechanisms responsible for the cohesion of polymer particles in CS will require further investigation if they are to be used in wear resistant applications or those requiring thicker deposits. Despite icephobicity being a surface phenomenon, surface durability remains a concern for the longevity of such coatings if they are to be used in harsh environments.

Metallic particles typically present elevated critical velocities (500-1200 m/s) allowing oxide cleaning to take place, while this is not the case for polymers [65]–[68]. For instance, critical velocities of 50-100 m/s were reported for the deposition of high density polyethylene feedstock on various polymer substrates [48]. In addition, critical velocities of 260-360 m/s for polyether-ether-ketone (PEEK) particles on PEEK substrates have also been observed [69]. Particle critical velocity can depend on many powder-related factors, such as the feedstock hardness, morphology, and mechanical and thermal properties, but is also influenced by other factors such as the substrate properties [66]–[68], [70]. Reaching, or going beyond the critical velocity in CS can present certain challenges for polymer feedstock. Increasing the particle's velocity can be achieved through increased stagnation conditions, however the resulting impinging gas supersonic velocities can delaminate layers that have been previously deposited. For this reason, decreasing the feedstock's particle critical velocity (therefore required gas velocity) can provide a way of obtaining particle deposition without compromising the coating's bonding to the substrate. It has been shown that particle temperature can greatly influence the particle critical velocity in CS [67], [70]. For instance, when depositing bronze feedstock onto aluminum and mild steel substrates, critical velocity decreases by 50 m/s for an increase of 100 °C in gas

temperature [70]. This conclusion is supported by the prediction of the critical velocity developed by Assadi et al.:

$$v_{cr} = 667 - 14\rho + 0.08T_m + 0.1\sigma_u - 0.4T_i \quad (1)$$

where ρ is the density in g/cm3, T_m is the melting temperature in ℃, σ_u is the ultimate strength in MPa, and T_i is the initial particle temperature in ℃ [67]. As can be deduced from the equation, particle temperature is the only variable that can be controlled by the process, rendering it a controlling factor in particle adhesion [67].

Reaching high particle impact temperature can be achieved in multiple ways, such as using a higher stagnation temperature. However, this will also increase gas velocity when using a conventional converging-diverging nozzle. Such elevated gas velocities can lead to coating delamination, which is attributed to not only the weaker bonding of polymers with metallic substrates (compared to metal-metal bonding) but also the large shear forces applied to the coating by the supersonic gas jet itself. More simply, higher particle impact temperature can also be achieved by altering the nozzle geometry [54], [65]. For instance, using a diffuser at the nozzle exit of a converging-diverging nozzle for the deposition of polyethylene feedstock on aluminum substrate was shown to created a shockwave within the nozzle, which reduced particle velocity and increased particle temperature to improve the deposition of the polymer feedstock [65], [71]. Despite the successful deposition, this nozzle design involves unnecessary gas velocity changes, such as rapid acceleration followed by a subsequent deceleration, rendering the design redundant. Similar nozzle design changes were performed to deposit ultra-high molecular weight polyethylene (UHMW) feedstock on aluminum substrate [54]. The complexity in the manufacturing of such nozzles could be a challenge. Alternative designs could be employed to attain similar particle impact velocity and temperature. Such designs could leverage the gas stagnation temperature to heat the particles, without having to produce a complex flow with shockwaves within the nozzle.

The current work aims firstly at developing a CS nozzle specifically adapted for PFA feedstock to allow its efficient spraying on metallic substrates. Using identical stagnation conditions as commercial nozzles, the new nozzle design should prevent the gas from expanding too much, thus preserving more of the thermal energy rather than converting

largely to kinetic energy. As a result, particles will increase in temperature, thus decreasing their critical velocity, and the integrity of bonded particles should not be compromised by the gas flow, preventing delamination. Computational fluid dynamics (CFD) modelling is used as a design tool while experiments are performed to validate and evaluate the performance of the new nozzle design compared to a commercially available nozzle. The second focus of this paper is to characterize the icephobic properties of the as-deposited coating along with reference surfaces, in a three-fold manner. First, static single droplets are analyzed on room temperature surfaces to examine the wetting state. Second, static single droplets are analyzed on both cold surfaces held at a specific temperature, and room temperature surfaces being progressively cooled to the same target temperature, to examine dynamic ice nucleation behaviors, ice growth times and frosting effects. A numerical model is developed to provide insight into the ice front formation and evolution during water droplet freezing. Lastly, surfaces with single droplets as well as surfaces with completely covered surfaces are analyzed to characterize ice adhesion and examine the effects of frost formation.

Experimental Procedure

Feedstock and Surface Materials

The feedstock powder used in this work is a commercially available adhesive perfluoroalkoxy alkane, or adhesive PFA (FLUON® EA-2000 PW50, AGC Chemicals America Inc, PA, USA) [72], with a particle size distribution, provided by the manufacturer, between 20 and 50 μm. Adhesive PFA is an inert crystalline fluoropolymer with very similar properties to PTFE (Teflon®), commonly used in non-stick applications [72], [73]. Scanning Electron Microscopy (SEM, Oxford Instruments, EVO-MA10, Zeiss, UK) images of adhesive PFA's morphology are presented in Figure 2. Unlike many commercial CS powders that have very spherical morphologies, this polymeric powder displays an irregular morphology with flake and coral-like shapes.

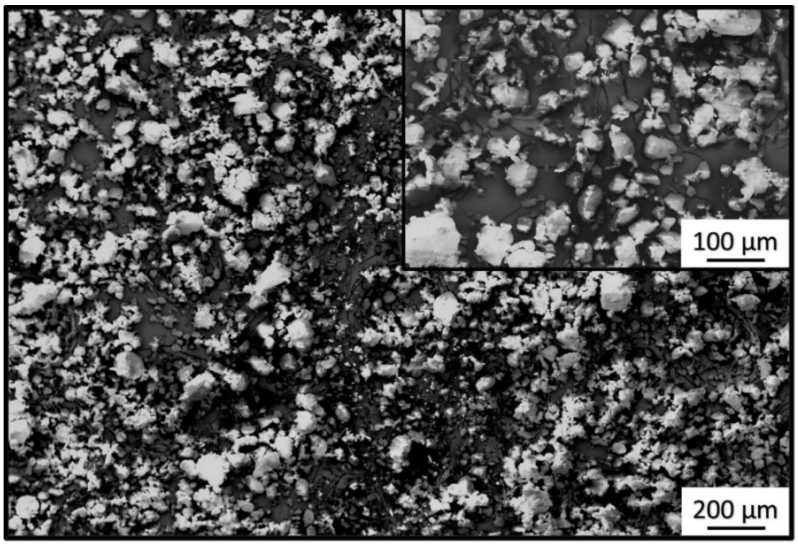

Figure 2. Adhesive PFA powder morphology at 45 and 175X magnification

Various reference materials are used for the comparison of icephobic level of the coatings produced. Two as-received aluminum surfaces are used: extruded (Al-1) and hot-rolled (Al-2) aluminum 6061-T6 (Metal Pros, ON, CA). Three polymer surfaces are also used: ultra-high molecular weight polyethylene (UHMW), polytetrafluoroethylene (PTFE) and PFA (McMaster Carr, IL, USA). A list of sample names and materials can be found in Table 1. The aluminum, UHMW and PTFE surfaces are all bulk materials in the form of plates and therefore are not applied on substrate materials. However, the bulk PFA is a thin film and therefore was applied on a substrate using two-sided tape (VHB, 3M, USA).

Table 1. List of sample names and surface materials

Sample name	Substrate	Surface material	Description
Al-1	N/A	As-received	Extruded plate
Al-2	N/A	As-received	Hot-rolled bar
UHMW	N/A	As-received	4.76 mm plate
PTFE	N/A	As-received	4.76 mm plate
PFA-F	Al6061-T6	As-received	0.127 mm film
PFA-C	Al6061-T6	As-sprayed	Cold sprayed coating

Coatings Preparation and Nozzle Design

Adhesive PFA coatings were deposited using a commercially available CS system (SST-EP, Centerline (Windsor) Limited, Windsor, ON, CA). The adhesive PFA powder was fed into the spray nozzles using a commercially available rotary powder feeder (AT-1200 Rotary, Thermach Inc., Appleton, WI, USA). A standoff distance of 15 mm was used with a 200 mm/s nozzle traverse speed. Aluminum 6061-T6 alloy substrates (Al-2) were grit-blasted (AG, Ruemelin Manufacturing Company, Milwaukee, WI, USA) prior to spraying using ferrosilicate grits (16 mesh – 20 grit) and nitrogen at 690 kPa was used as the grit blasting gas. The polymer feedstock material has a thermal expansion coefficient substantially larger than that of the metal substrate. As a result, tensile stresses can occur in the coating. To bridge that difference, pre-heating of the substrate was conducted using a 25.4 mm x 200 mm strip heater (Omega Environmental, QC, CA). Raising the surface temperature of the substrate to 200 ℃, prior to the deposition of the polymer coating. Substrate temperature was monitored with a thermocouple probe (K-type, Omega Environmental, QC, CA) inserted within the substrate at an acquisition rate of 10 Hz. Substrate temperature was monitored for the entire deposition process of a coating, with and without substrate pre-heating to examine the effect of substrate temperature on coating adhesion. Coatings were produced in a single layer deposition, with a 0.5 mm step between each nozzle passes over the substrate.

Coatings, Feedstock and Surface Analysis

Adhesive PFA coating samples were cut (Secotom-10, Struers, Mississauga, ON, CA) into manageable pieces required for the analysis steps. Samples were mounted, using epoxy resin, followed by mechanically grinding and polishing (TegraPol-31, Struers, Mississauga, ON, CA) the mounted samples to a mirror finish. Coating cross-sections and top views were examined using a scanning electron microscope (SEM) (EVO-MA10, Zeiss, Germany) to observe the coating/substrate interfaces, determine coatings thickness and porosity level. Surface roughness of samples were obtained using a profilometer (SRG-4000, Phase II Plus, NJ, USA).

Wettability

Wettability characterisation was carried out using the sessile drop method [74]. The goniometer system consists of a high precision motion system (Benchtop XYZ Motion System, Aerotech Inc., PA, USA) coupled with a CNC-controlled micro-syringe, as shown in Figure 3. The 10 µL water droplet was precisely controlled by the computer monitored syringe until the target droplet volume was achieved. The syringe carrying the droplet was lowered at a constant speed until the droplet contacted the surface. Images were captured once the syringe was removed and the droplet settled, using a digital microscope camera. Backlighting was provided by a LED light source (MNWHL4 LED, Thorlabs, NJ, USA) located behind the droplet.

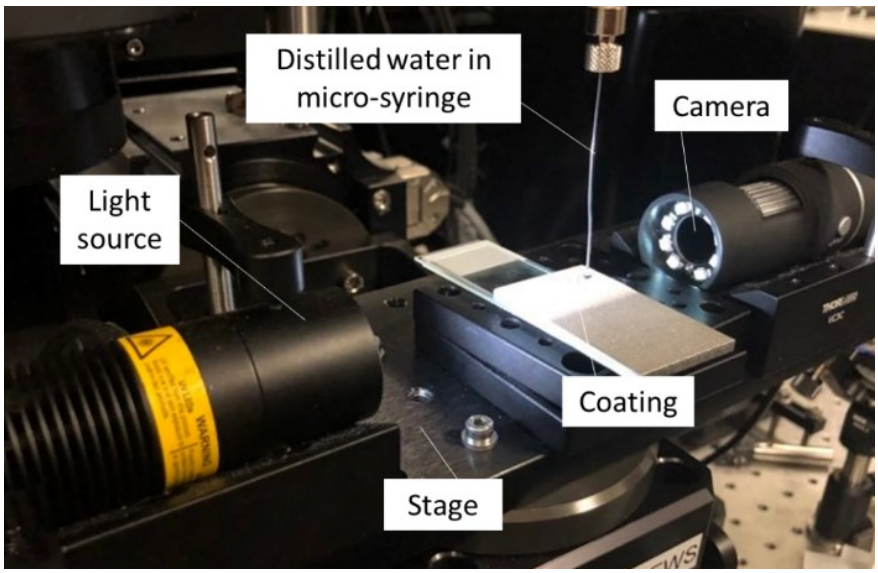

Figure 3. Goniometer used to perform the sessile drop method on coated and uncoated surfaces

Single Droplet Analysis

The experimental setup used to observe the ice nucleation and growth is shown schematically in Figure 4. The setup consists of a custom-built cryostage which uses a programmable Peltier unit (S3 Series 800, Alpha Omega Instruments, QC, CA) coupled with a cooling bath (Thermo NESLAB, Marshall Scientific, NH, USA) acting as a heat sink. The cooling bath fluid is a 50:50 mixture of ethylene glycol and 99% ethanol. The cryostage's temperature was held at -10.0 ℃ ± 0.1 ℃ and was monitored using an

embedded thermocouple. A micropipette was used to deposit a 10 µL droplet of Milli-Q® water onto the testing surface and lighting overlooking the droplet was adjusted as needed to allow the distinction of clarity changes in the droplets throughout the test. High resolution videos were obtained using a digital microscope camera (Nikon OEM, NY, USA) fitted with a 35 mm lens (3520ML12M, Azure Photonics, Fujian, JA) that is set to a working distance of 0.2 m and aperture of 2.0. To decrease the working distance of the lens for imaging, a 7 mm spacer ring was fitted between the camera and the lens. Camera exposure ranged from 5 to 25 µs depending on the surface brightness and how much light was required for a clear view of the droplet. Images used in this work were extracted from the high-resolution videos using the NIS elements D software.

Reference surfaces along with the cold sprayed adhesive PFA coating were cut to 8 mm x 8 mm sections to fit within the 15 mm diameter opening in the cryostage chamber. Samples were subjected to two different ice formation conditions to observe the effect of different wetting states during freezing, and the effect of frost formation on each surface type. The first method involved pre-cooling the test surfaces by storing them in a commercial freezer at a temperature of -4.0 ℃, followed by placing the surface within the cryostage chamber for a period of 5 minutes allowing the sample surface reaching equilibrium at -10 ℃ prior to depositing the water droplet. This method will be referenced as the isothermal substrate. The second method involved placing an individual test surface at room temperature inside the cryostage without any pre-cooling or equilibrium time, followed by immediate deposition of a water droplet. This method will be referenced as the cooled substrate. To maintain consistency of the initial nucleation event between experimental trials, droplets were mechanically nucleated using an 18-gauge needle pre-cooled to -78 ℃ (needles were stored on dry ice) held near the surface of each droplet. Nucleation prompting using the needle was kept constant through all trials by bringing the needle close to droplets immediately after deposition. However, for the cooled substrate case, it was not uncommon requiring a few attempts at nucleating the droplet since the droplet temperature was likely still above its freezing point. Freezing time data was visually assessed through time-lapse videos establishing the time from nucleation initiation until complete droplet solidification. Based on the SCA measurements obtained in the sessile drop method, SCAs and uncertainties for single droplets on the cryostage were determined through visual image

comparison. As a result, uncertainty measurements are larger than they are for the SCAs obtained in the sessile drop method.

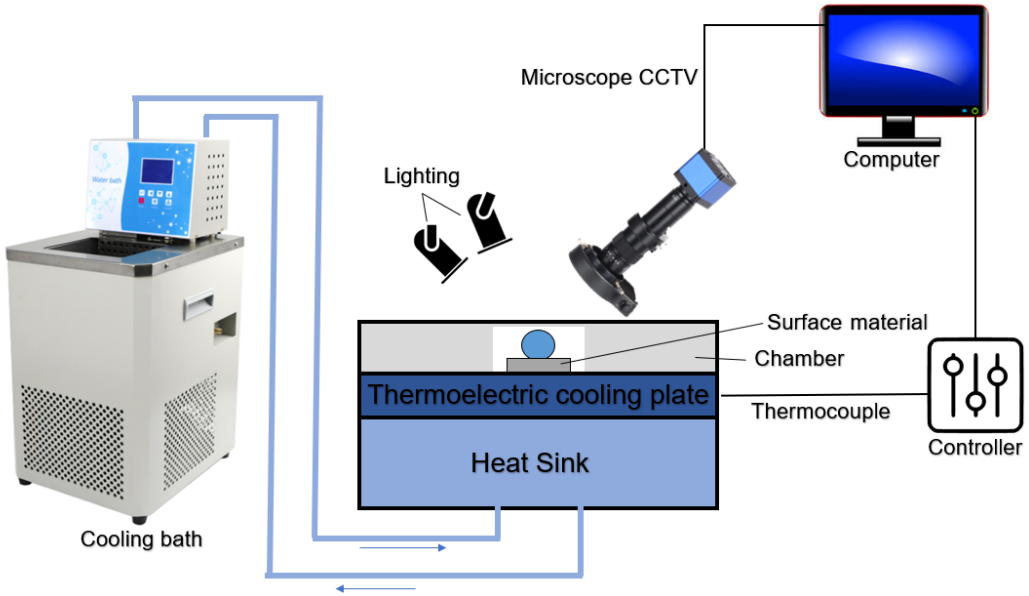

Figure 4. Schematic of water droplet icing delay and nucleation observation setup

Ice Adhesion Testing

Ice adhesion strength on test surfaces was determined in two ways; the macro centrifuge adhesion test (CAT) and the micro shear test.

Macro Centrifuge Adhesion Test

In the macro test, icephobic performance of a surface was quantified using the interfacial ice adhesion shear strength (τ_s) obtained through CAT [75], [76]. The custom CAT system involves constantly accelerating an iced rotor until the ice detaches from the surface. Test rotors in this work were 31.75 mm wide by 254 mm long by 3.175 mm thick and made of aluminum 6061, and test surfaces were glued on a single end of the rotor using two-sided tape (VHB, 3M, USA). For the cold sprayed PFA coating, deposition occurred directly on the aluminum rotor which served as the substrate. An aluminum counterweight was fixed on the opposing end of each rotor with the equivalent weight (HZT-B3000, THEMIS-BP, Rockland, Canada) as the test surface and solidified ice cube. An example of a mounted rotor is shown in Figure 5. The ice was statically produced with distilled water in a 31.75

mm wide by 31.75 mm long by 12.7 mm deep silicone ice cube tray. Rotors were placed upside down with their test surface facing the bottom of the tray and distilled water was used to fill the tray up to the test surface's interface. Rotors were left to solidify inside the climatic chamber at -10 ℃ ± 1 ℃, simulating glaze ice formation seen in atmospheric icing [1]. Temperature control of the cooled environment was maintained using a thermocouple (ITC-308 with NTC probe, InkBird, China).

The τ_s of the surface was obtained by the centrifugal force needed to detach the ice from the test surface. The centrifugal force is given by

$$F = m * r * \omega^2 \tag{2}$$

where *F* is the force (N), *m* is the mass of the ice cube (kg), *r* is the rotor radius (m) and ω is the angular velocity when ice is detached (rad/s). The angular velocity, needed for ice detachment, was determined when the shaft became unbalanced at the moment ice detached. Radial shaft vibrations from the unbalanced rotations were tracked with a vibration sensor (3738T1, McMaster Carr, IL, USA) mounted radially on the flange bearing within the chest freezer. The shaft's angular velocity could then be determined at the precise moment ice was detached, due to the imbalance of weight on the spinning shaft. The rotor's angular velocity was determined using in the motor's variable frequency drive (VFD) (Optidrive E3, Invertek Drives, Orangeville, Canada). The VFD's output voltage was mapped to the theoretical rotational velocity of the motor, and then multiplied by the belt ratio to account for the increase in sheave size. The ramp up time, which enables the shaft to constantly accelerate from zero to full speed, was set at 45 seconds which provided enough resolution to accurately determine the rotational velocity when ice detached. Using the centrifugal force, the τ_s of the surface is given by

$$\tau_s = \frac{F}{A} \tag{3}$$

where τ_s is the interfacial ice adhesion shear strength (Pa) and A is the surface area covered by the ice cube (m2). Due to the large variations of different testing setups used in different laboratories, and the lack of a standardized testing procedure relating to CAT, this experiment typically lacks replicability [77]. As such, the τ_s values presented in other work can seem skewed or difficult to accurately compare. For this reason, a ratio was made

between the τ_s of a tested surface and a bare metallic surface to determine the icephobic efficacy and reduction in τ_s [1]. Quantifying this ratio was done using the adhesion reduction factor (ARF) and is given by

$$ARF = \frac{(\tau_{ice})_{reference\ material}}{(\tau_{ice})_{test\ surface}} \quad (4)$$

where ARF is adimensional and represents the ratio of reduced interfacial ice adhesion shear strength between the icephobic surface and a control surface. If the ARF of a surface is above 1, then the surface successfully reduced the τ_s, however a surface is typically deemed as passively icephobic if the ARF reaches around 10 [1]. The reference material, meant to represent current applications using aluminum surfaces and facing icing challenges, was the Al-1 surface, based on its surface finish and overall surface roughness.

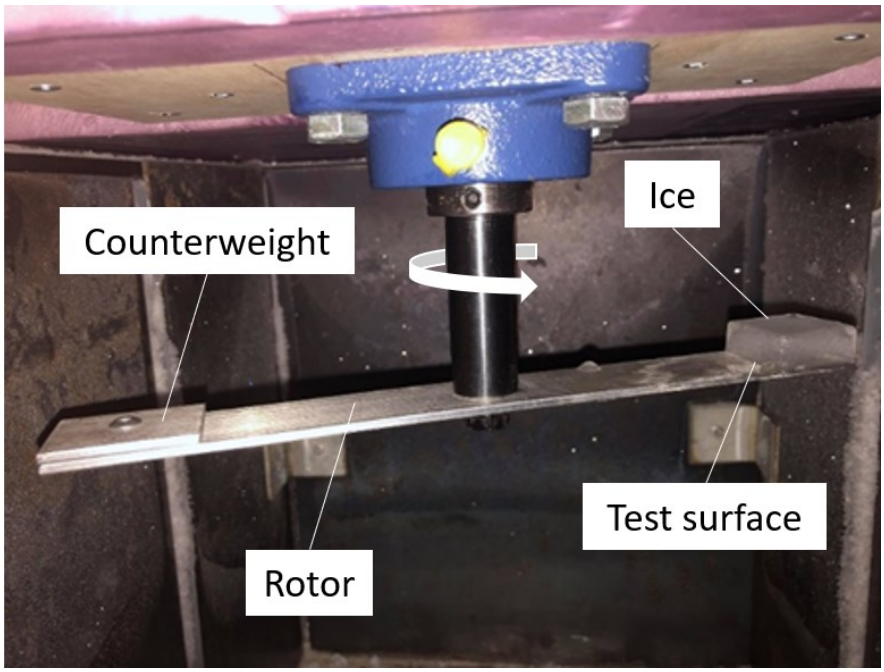

Figure 5. Iced rotor used in the CAT

Micro Shear Test

In the micro shear test, ice adhesion is also quantified; however, this test is performed on single solidified micro droplets, using a custom-built pushing system, shown in Figure 6. The micro shear test's main components include an aluminum base to support the cryostage

and a dovetail rail system allowing a linear movement of the pushing surface. The top section of the dovetail houses a 1000 g ± 1 g compression load cell (REB7, Loadstar sensors, CA, USA) fitted with a steel pushing rod extending into the cryostage and onto the test surface. The micro shear test was performed immediately after single droplet solidification, as described in the previous section. Steel pushing rods were kept on dry ice at approximately -78 ℃, which prevented melting of the frozen droplet at contact. Using a manually controlled micrometer, the top dovetail assembly was pushed horizontally resulting in the steel pushing rod being pressed against the solidified water droplet. Data was captured by the load cell and was monitored through the LV-1000 software, provided with the sensor, at an acquisition rate of 10 Hz. The peak load observed during the micro shear test was retained and used to characterize the ice adhesion for each surface. Due to the pushing rod being in a cantilever position, loads seen by the load cell excluded a moment being induced on the system. As a result, the load cell was calibrated as it reads 83% of actual loads.

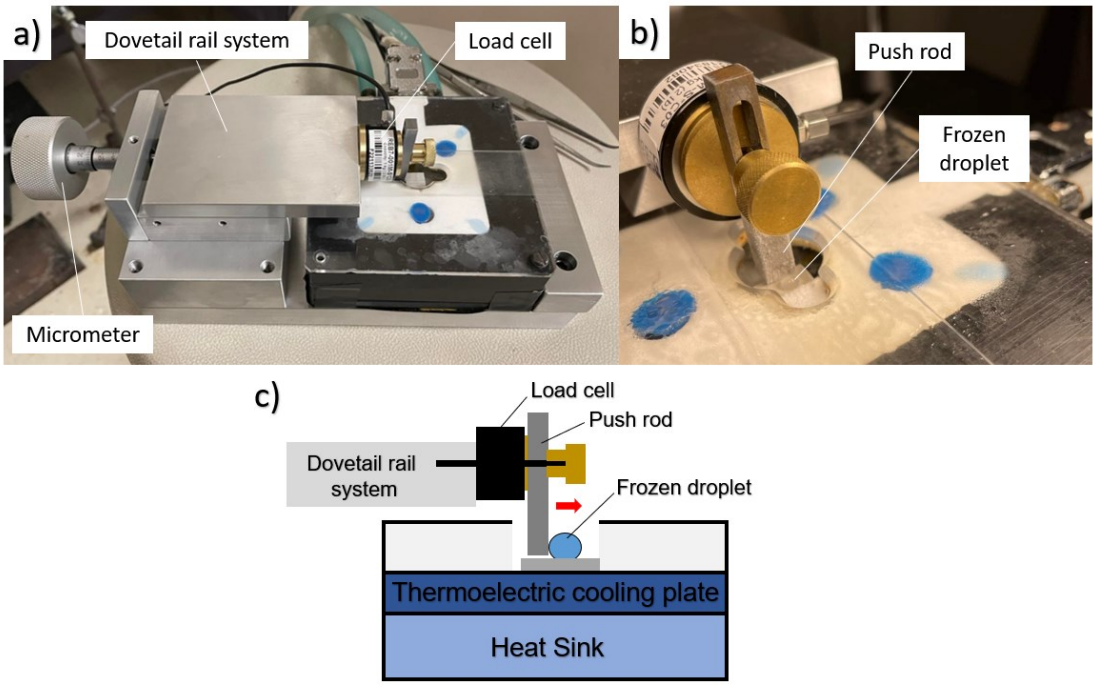

Figure 6. Micro shear test: a) experimental setup with cryostage, b) pushing rod with frozen water droplet, and c) overall schematic cross-section

Computational Fluid Dynamics Modeling

Computational modelling was used to simulate the nozzle gas flows of the commercial and of the newly designed cold spray nozzles. Modeling of the freezing of water droplets to examine the ice nucleation and growth behaviors was also performed.

Nozzle Flows

Modelling of the gas flow inside and outside of both the commercial CS nozzle (nozzle 1) and the specifically designed nozzle (nozzle 2) was done using the commercial computational fluid dynamics software, ANSYS Fluent version 16. Dimensions used to model both nozzles are found in Figure 7, with the nozzle 2 dimensions being the result of a series of conceptual nozzle designs tested but only the retained geometry being presented here.

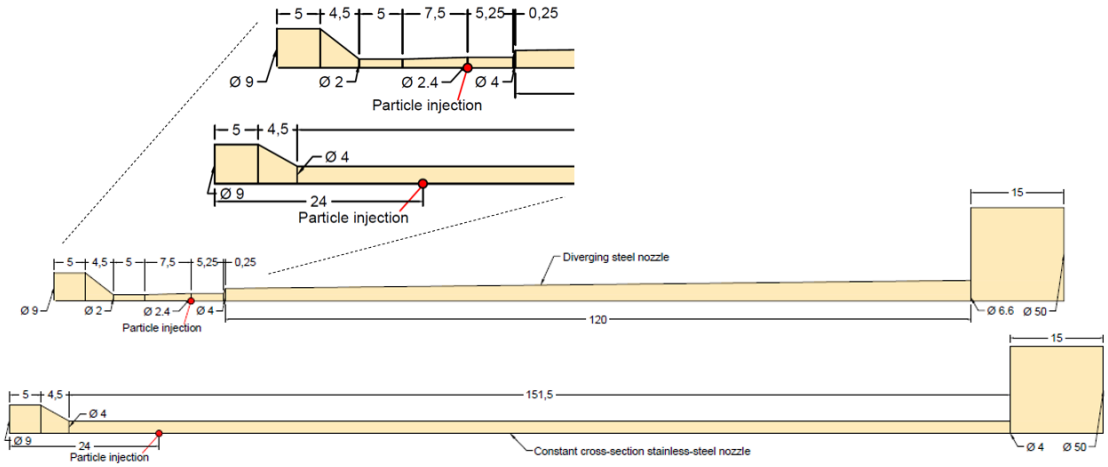

Figure 7. Computational domain dimensions for nozzle 1 (top) and nozzle 2 (bottom). Downstream particle injection on the symmetry axis is found in red for both nozzles. (All dimensions in mm)

Both nozzle flows were modelled as steady-state and two-dimensional axisymmetric assumption was used to reduce computational time. Reynolds Average Navier-Stokes (RANS) equations were used along with the re-normalized k-ε turbulence model (RNG k-ε) to account for turbulent effects of the supersonic flows. The RNG k-ε turbulence model was chosen for its renowned accuracy when modelling supersonic flows in CS nozzles [78]–[80]. Compressibility effect of the nitrogen process gas was accounted for by assuming the gas obeys the perfect gas law, and a constant viscosity was used as the

variation of viscosity with temperature is not prominent in low Mach-number flows [78], [79]. Particle history in the flows were studied by single particle injection downstream of the nozzle throat, for nozzle 1, and downstream of the converging section for nozzle 2, as indicated in Figure 7. The feedstock's mean particle size of 35 μm was used for the modelling of injected particles and particle shape was assumed to be spherical. Injection occurred on the centerline using the one-way Lagrangian discrete phase model (DPM). The DPM along with high-Mach-number drag law was also used to obtain particle velocity and temperature throughout the nozzle. Particle injection location for both nozzles are shown in Figure 7.

Properties of the nitrogen gas and the injected Adhesive PFA particles are found in Table 2.

Table 2. Simulated phases properties

Property	Nitrogen Gas	PFA Particles
CS parameters	413 kPa, 375 ℃	N/A
Particle size (μm)	N/A	35
Density, kg/m^3	Ideal Gas	2150
Specific heat capacity, J/kg K	Piecewise polynomial	1050
Thermal conductivity, W/mK	0.0242	0.209
Viscosity, kg/ms	Constant	N/A
Initial particle temperature (^{o}C)	N/A	25

A pressure-based solver was used along with a Green-Gauss node-based gradient method to model the nitrogen gas within both nozzles [78], [79]. Convergence was determined firstly by a decrease in residuals of at least four orders of magnitude and then by a mass imbalance of less than 0.1% between the nozzle inlet and outlet. Nozzle inlets were set to a pressure-inlet boundary condition, with chosen stagnation condition values matching experimental values used, and the nozzle outlets were set to pressure-outlet, with atmospheric condition values. The substrate was modelled as an adiabatic wall with a 15 mm standoff distance from the nozzle outlet (for both nozzles). The spray chamber was set at 50 mm radius to prevent affecting the flow field (the spray chamber is not to scale in Figure 7). Stagnation conditions and boundary conditions for both nozzles can be found in Table 2 and Table 3, respectively.

Table 3. CFD model boundary conditions

Location	Boundary Condition	Temperature	Pressure
Nozzle inlet	Pressure-inlet	375 ℃	413 kPa
Nozzle walls	Wall	Adiabatic	N/A
Nozzle outlet	Pressure-outlet	Ambient Conditions	Atmospheric
Substrate	Wall	Adiabatic	N/A

The computational domain was meshed using ANSYS Workbench Meshing Tool 16 and the domains were discretized into individual sections at the junction of each nozzle wall. Edge sizing was used within the discretized sections to control the mesh size. Both nozzles have structured quadrilateral non-uniform meshes with orthogonal quality above 0.98 and skewness equal to 0.02 (nozzle 1) and 0.01 (nozzle 2). The domain grid consists of approximately 200,000 elements for both nozzles. Grid independence was confirmed through a mesh refinement study and further mesh refinement was carried out in the diverging section of nozzle 1 and at the exit of nozzle 2 to adequately capture all flow features, such as expansion fans and shock waves.

Water Droplet Freezing

Numerical Simulation Method

A coupled volume-of-fluid (VOF) approach was used to model the air/water interface. The finite-volume flow solver ANSYS Fluent 2022-R2 was chosen for the implementation of water droplet solidification. The Solidification/Melting model was used to simulate the phase change within the solidifying water droplet. A two-dimensional axisymmetric computational domain has been used, a shown in Figure 8. The aluminum substrate surface (located at the bottom) is regarded as a cold wall with a no slip boundary. The right axis is set as the axis of symmetry while the other boundaries are set as pressure outlet boundaries. A structured mesh was used to better capture the liquid-gas interface and improve the computational efficiency. Incompressible fluid property was assumed. The volume change due to water expansion during freezing is known to have negligible influence [81] and hence has been disregarded in the current numerical model. Moreover, since the time of the nucleation and recalescence steps is very short, making it difficult to simulate, these

processes have not been included in the model. Additionally, since it is a supercooled water droplet that changes into a water-ice mixture during the disregarded nucleation and recalescence stages, the supercooling process has also been omitted from the model.

To simplify the numerical model further, the surrounding environment has been modeled as dry air, i.e. no humidity, which eliminates air related phase changes. Hence, the mass of the whole droplet is conserved throughout the freezing process[82], [83]:

Gravity was included in the direction of droplet fall. A surface tension of 0.0735 N/m was applied at the contact between air and water volume [83]. The wall-adhesion model was utilized to describe the effects of contact angle. Contact angles of 120° and 85° were used for the cases with an aluminum substrate at -10 ℃ (isothermal substrate) and an aluminum substrate cooled from room temperature, i.e. 20 ℃ to -10 ℃ (cooled substrate), respectively.

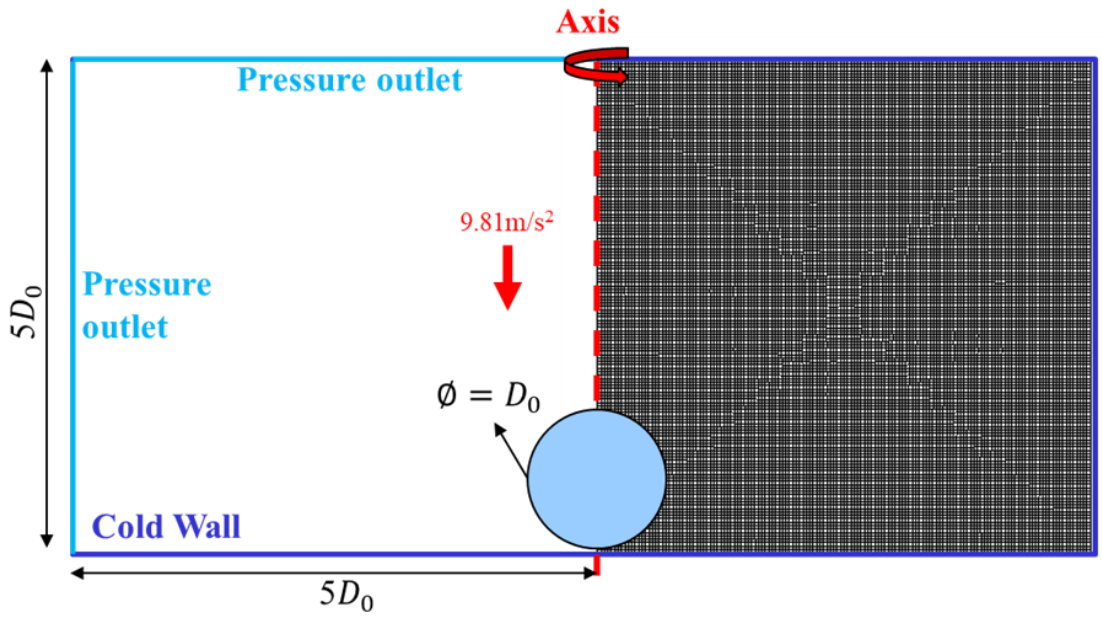

Figure 8. Physical model with dimensions (left half) and numerical structured mesh (right half).

The water droplet was initialized to 15 ℃ and has zero initial velocity. The surrounding dry air was initialized at -10 ℃. The droplet was placed close to the substrate surface to

replicate close initial contact of the experimental set-up. The water droplet was accelerated by gravity, however, the impact of such acceleration was minimal as the particle was modeled relatively close to the deposition location. The simulation was carried out until the 10 µL water droplet was fully frozen. The properties of water, air, and aluminum utilized in the current numerical model are presented in Table 4.

Table 4. Material properties for water and ice used in the numerical model

Material	$\boldsymbol{\rho, kg/m^3}$	$\boldsymbol{C_p, J/kg \cdot K}$	$\boldsymbol{k, W/m \cdot K}$	$\boldsymbol{L, J/kg}$
Water	1000	4187	0.6	333000
Air	1.225	1006.43	0.0242	0
Aluminum	2719	871	202.4	N/A

Solidification Model

An enthalpy-porosity method was utilized to model the solidification, i.e. freezing, in the water medium. In this method, liquid fraction indicates the fraction of the cell volume that is in the liquid form. The domain is regarded as a porous media, in which the porosity β takes the value of $\beta = 1$ in the liquid phase, $\beta = 0$ in the solid phase and $0 < \beta < 1$ in a "mushy" zone (partially solidified zone). When the porosity reaches a solid state ($\beta = 1$), the velocity in the zone drops to zero. The "mushy" state decreases as the latent heat is removed from the liquid, which accounts for increased rigidity and decrease in velocity during solidification. To account for such changes, a source term is added to the momentum equation and expressed as;

$$S = \frac{(1-\beta)^2}{(\beta^3 + \epsilon)} \cdot A_{mush} \cdot v \tag{5}$$

where A_{mush} is the "mush" zone parameter, ϵ is a small number (0.001) to prevent a division by zero, and v is the fluid velocity. The rate at which the source term decreases the velocity is controlled by the "mushy" parameter. Hence, a larger value of A_{mush} increases the rate at which the source term dominates the momentum equation. Various studies have indicated that the A_{mush} term is empirical and should be determined on a case-by-case basis. In the current study, a value of 5×10^4 was chosen based on previous studies for which similar impact process have been modeled [81], [83]. This term controls the rate

at which the velocity in the front of the "mushy" zone transitions to ice as the solidification front advances, i.e. reflects the degree of difficulty of freezing.

The effect of phase change on the energy equation is performed by modifying the material total enthalpy, *H*, (sum of the internal energy) expressed as;

$$H = h + \Delta H, \tag{6}$$

where h is the sensible heat and $\Delta H = f(T)$ is the latent heat. The sensible heat can be expressed as;

$$h = h_{ref} + \int_{T_{ref}}^{T} C_p dT \tag{7}$$

where h_{ref} is the reference enthalpy set to 333 kJ/kg at the reference temperature, T_{ref}, set at 273 K and C_p is the specific heat at constant pressure. The latent heat released during the freezing process is modeled as the difference in enthalpy between the ice and water. In the current model the liquid fraction is computed using;

$$\Delta H = L\beta \tag{8}$$

where L is the latent heat of the phase change and the liquid fraction, β is defined as;

$$f(T) = \begin{cases} \beta = 0 \quad if \;\; T < T_{solidus} \\ \beta = 1 \quad if \;\; T > T_{liquidus} \\ = \dfrac{T - T_{liquidus}}{T_{liquidus} - T_{solidus}} \quad if \;\; T_{solidus} < T < T_{liquidus} \end{cases} \tag{9}$$

In the current study, $T_{solidus} = T_F - \Delta T_F/2$ and $T_{liquidus} = T_F + \Delta T_F/2$, where T_F is the freezing temperature such that $\Delta T_F = 0.2$ ℃ represents the phase change temperature range. A small ΔT_F value is chosen to smooth the sharp changes in temperature-dependent thermophysical properties at the freezing temperature and allow convergence. Additionally, previous studies have shown that such value of ΔT_F provides results matching experimental freezing data [84]. Hence, the material latent heat, ΔH, is controlled to vary between 0 (pure solid phase) and *L* (pure liquid phase).

Results and Discussion

Feedstock Powder

The effect of powder properties in CS, such as morphology and size distribution has been documented extensively for metallic powders [85]–[87]. The morphology of the particles is said to influence coating porosity, hardness and deposition efficiency [87]. MacDonald et al. found that irregular morphology Ti6Al4V powder can be deposited with high deposition efficiency and minimal porosity [85]. They found the coral-shaped particles flattened on themselves during deposition giving very dense coatings [85]. Wong et al. demonstrated that for CS of pure titanium, spherical powder with an average diameter of 29 microns resulted in the best coatings based on deposition efficiency and porosity levels [86]. Polymer powders, on the other hand, can be largely influenced by their chemical properties such as interparticle cohesive forces [88]. The cohesive attraction between particles can result in the formation of aggregates prior to injection or while in flight and thus influence the particle velocity reached during the process [88]. The polymer powder used in this work, Adhesive PFA, as shown in Figure 2, displays an irregular morphology with flake and coral-like shapes. Contrary to other polymer powders that suffer from aggregate formation, the adhesive PFA feedstock does not because of the additive in the chemical composition of the powder.

CFD Nozzle Flows

The gas temperature and velocity contours for nozzles 1 and 2 are shown in Figure 9, for stagnation conditions of 413 kPa and 375 ℃. These stagnation conditions were chosen based on trials performed with nozzle 1, because any further increase in pressure or temperature resulted in partial delamination of the coating from the substrate. In addition, increased stagnation temperature also resulted in feedstock melting, leading to observable clogging in nozzle 1. With these stagnation conditions, the highest gas velocity reached in nozzle 1 is 1052 m/s, and 560 m/s in nozzle 2. In a converging-diverging nozzle geometry, such as nozzle 1, the pressure ratio between the back pressure (ambient pressure in this case) and stagnation pressure determines whether the flow will be supersonic or subsonic [89]. For nozzle 1, shown in Figure 9, the gas velocity becomes supersonic after the throat

and reaches Mach 4.2 at 0.0322 m from the nozzle inlet. The pressure ratio at this point of the flow is much lower than the designed pressure ratio (over-expanded flow) and results in the initiation of a series of oblique shock waves that eventually bring the gas pressure to the ambient pressure.

Nozzle 2, on the other hand, does not behave the same way for several reasons. Firstly, a supersonic gas flow requires a converging-diverging cross-section, which nozzle 2 does not possess. A subsonic flow can only become supersonic once it has reached a sonic condition (Mach=1), located at a minimum area section, and will continue to accelerate if the gas can expand through a diverging cross-section [89]. Secondly, nozzle 2 has a constant diameter twice the size of nozzle 1's throat, which means even if the pressure ratio is the same between both nozzles, the ratio between the throat area and exit area are not the same. As a result, the difference in area ratios prevents nozzle 2's flow from reaching its sonic condition at the smallest area, as shown in Figure 10 by the visible difference in gas velocity within both nozzles. Nonetheless, the flow inside nozzle 2 does accelerate and reach supersonic velocities once outside the nozzle. This occurs because of the formation of a Prandtl-Meyer fan (expansion fan) that develops to allow gas expansion to the ambient pressure. As seen in Figure 10, the gas velocity outside of nozzle 2 rapidly increases, then decreases, which is caused by sequential expansion fan and shock waves to bring the flow back to the atmospheric pressure and in line with the original flow direction.

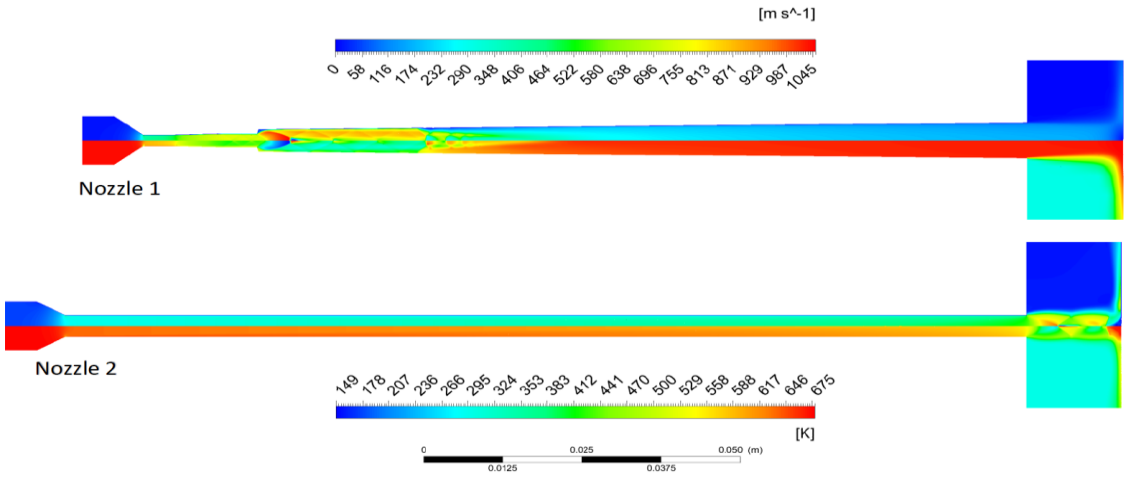

Figure 9. Nitrogen flow velocity (top) and temperature (bottom) contours for nozzle 1 and nozzle 2 at inlet stagnation conditions of 413 kPa and 375 °C

Particle Velocity and Temperature

Adhesive PFA particle injection was simulated in both nozzles, on the nozzle symmetry line: downstream of the nozzle throat for nozzle 1, and after the converging section of nozzle 2. The modelled particle in nozzle 1 reached a maximal velocity of 254 m/s inside the nozzle, at 0.063 m past its injection location, and had a velocity of 244 m/s before impacting the substrate. The modelled particle in nozzle 2 was continually accelerated in the nozzle and reached its maximal velocity in the free stream, at 0.15 m from its injection location, with a velocity of 328 m/s, and had a velocity of 325 m/s prior to impacting the substrate. The particle injection for nozzle 1 is located immediately before a rapid acceleration of the nitrogen gas caused by gas expansion, followed by a shock train to restore the pressure. The injected particle rapidly accelerates until its velocity is affected by the strong oscillating gas properties caused by the shock waves, as seen in Figure 10. Despite the gas velocity steadily decreasing at this point, the injected particle's inertia maintains the particle's velocity fairly constant until it exits the nozzle. Conversely, the injected particle in nozzle 2 is subjected to continuous acceleration, much like the processing gas. As can be observed in Figure 10, the result is a continuous increase in particle velocity throughout the nozzle with a slight fluctuation in the free stream caused by the expansion fan. The resulting particle velocity in the new nozzle is 80 m/s higher than in the commercial CS nozzle, when using the same stagnation conditions. This increase in particle velocity will help reach the particle's critical velocity, thus aiding the deposition of the feedstock material.

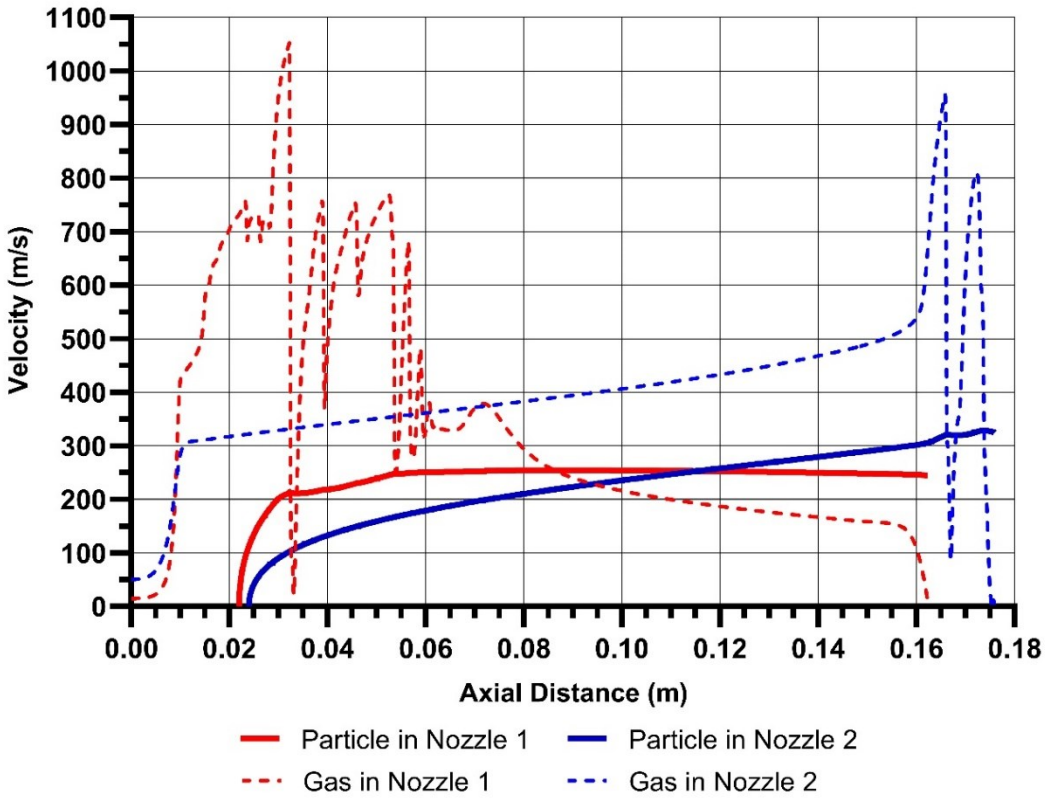

Figure 10. Adhesive PFA particle velocity, and nitrogen gas velocity for nozzle 1 (red) and nozzle 2 (blue)

The modelled Adhesive PFA particles reached a maximal temperature of 85 ℃ with nozzle 1, and 181 ℃ with nozzle 2, prior to impacting the substrate. These temperatures are well below the melting and maximum operating temperature of 300 ℃ and 260 ℃ for adhesive PFA. As can be seen in Figure 11, the modelled particle temperature in nozzle 1 steadily increases from its injection into the nitrogen gas flow until it reaches the substrate. The particle enters the flow at the coldest region of the nozzle, which is where the gas is accelerating to its peak Mach number. However, once the particle passes through the shock waves, the gas temperature rises to near its stagnation temperature, thus accelerating the heating of the polymer particle in the process. In contrast, the modelled particle temperature in nozzle 2 is subjected to a large amount of heating at its injection location because the nitrogen gas flow remains subsonic, and therefore the gas temperature remains close to the stagnation temperature. The modelled particle temperature in nozzle 2 then begins to plateau, reaching a constant value at the nozzle exit and in the free stream. The observable

increase in particle temperature for the new nozzle design suggests that particles are thermally softened prior to deposition. As a result, the particle critical velocity is expected to be lower and therefore the deposition of the feedstock should increase, leading to thicker deposits.

Based on these results, the new nozzle design was manufactured and used for experimental comparison with the existing commercial nozzle.

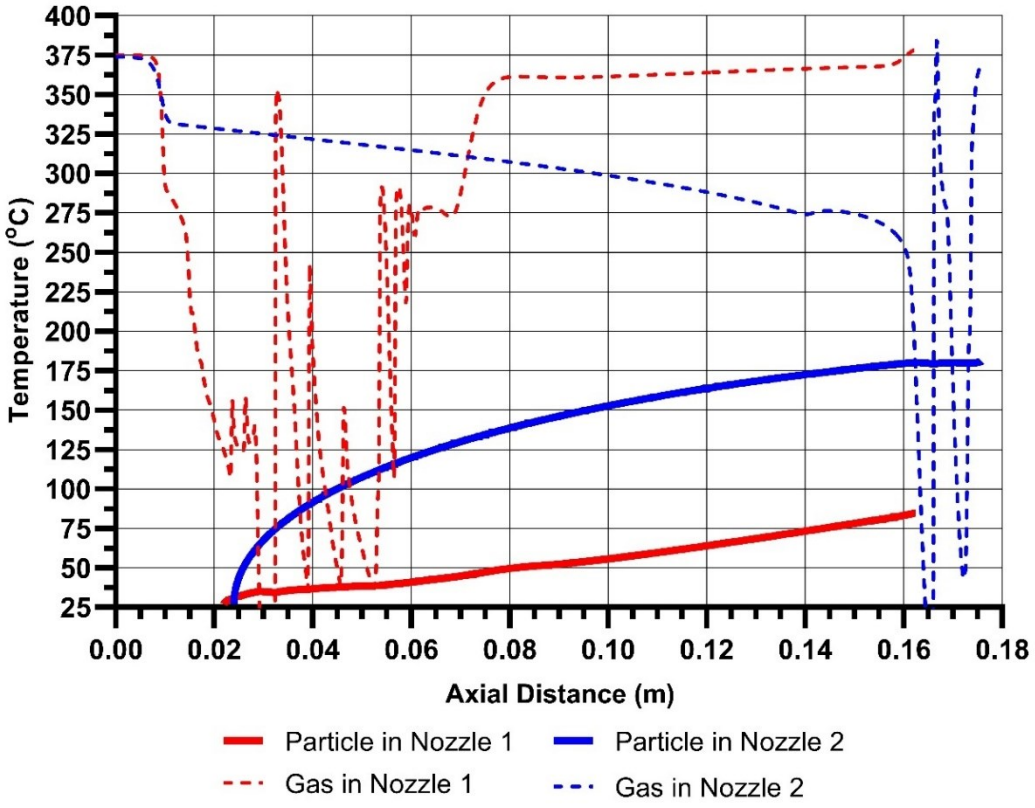

Figure 11. Adhesive PFA particle temperature, and nitrogen gas temperature for nozzle 1 (red) and nozzle 2 (blue)

Cold Spray Coating Analysis

Passive anti-icing systems, such as icephobic coatings used on aerodynamically sensitive structures, are expected to be thin, as icephobicity is a surface phenomenon. Aerodynamic properties like lift optimization and drag reduction must not be altered [1]. However, it is known that polymer coatings do not have high erosion resistance or durability in harsh environments [90]. Therefore, it is imperative to obtain a fully dense coating that improves

the coating's wear resistance and overall durability, while remaining thin enough to prevent alteration of the original substrate design geometry. Figure 12a shows the coating produced by nozzle 1, displaying an approximate thickness of 50 µm. However, it is a porous coating and there is minimal deposition. Figure 12b shows nozzle 2 coating cross-section, which displays a 150 µm thick coating with minor amounts of visible pores. Contrarily to nozzle 2, it appears that the coating produced with nozzle 1 does not contain any deposition past the first layer. The variability in overall deposition and coating quality between both nozzles is linked to particle impact temperature and velocity. Computational results show that particles exiting nozzle 2 should be warmer and faster than the particles exiting nozzle 1, while using the same low spray parameters to minimize delamination due to the impinging gas. Therefore, it is reasonable to assume that the increase in particle temperature and velocity with nozzle 2 did lead to the observed enhanced deposition. Although coating delamination is observed in nozzle 2's coating cross-section, it is believed that any observable delamination took place during the sample's cutting, mounting, and polishing procedure due to the use of non-optimized parameters for sample preparation.

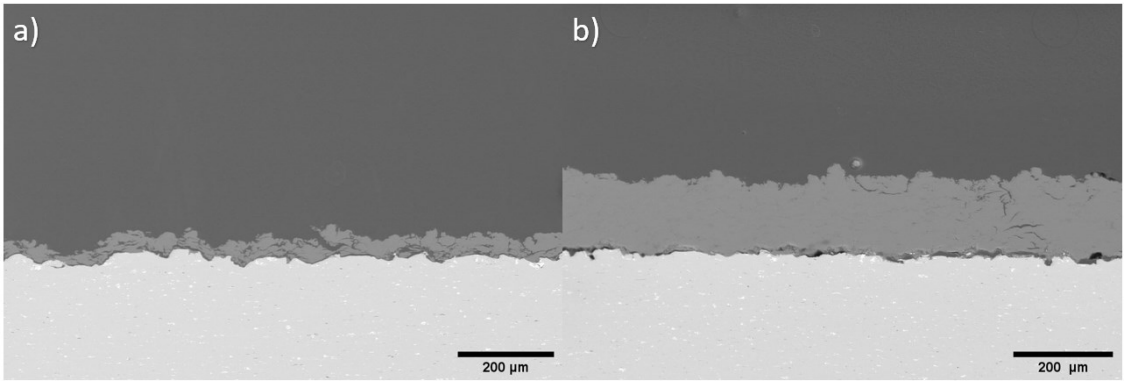

Figure 12. SEM image of coating cross sections produced by a) nozzle 1, b) nozzle 2.

In CS, coating adhesion is greatly influenced by the coating's residual stresses [64]. In the case of depositing dissimilar materials, such as adhesive PFA onto aluminum, the large difference in thermal expansion coefficients creates residual stresses due to thermal mismatch [91]. This difference in thermal expansion causes mechanical bonds to break by the sliding movement at the coating/substrate interface.

Since substrate pre-heating was required to prevent the delamination of the thick coatings produced with the nozzle 2, the substrate's temperature was monitored with substrate preheating and without to observe its effect on substrate temperature. As shown in Figure 13, with the use of substrate preheating to a surface temperature of 200 ℃, the substrate's temperature begins to decrease immediately once the deposition begins and constantly decreases as the nozzle makes its way over the substrate. Although the gas coming from the nozzle is initially warmer than the substrate, with a stagnation temperature of 375 ℃, mixing of the hot gas with ambient air, combined with convection effects on the substrate surface, led to the constant drop in temperature. Without preheating the substrate, the substrate's temperature quickly begins to rise from ambient conditions immediately once the nozzle passes over the surface. The sudden rise in substrate temperature occurs in the first 30 seconds of deposition. The substrate then reaches a constant temperature for the remaining 30 seconds. The final substrate temperatures, registered by the thermocouple, are 60 ℃ and 118 ℃, without and with substrate preheating, respectively. Accordingly, coating delamination was observed exclusively when the substrate was not preheated, indicating that an increased substrate temperature throughout the deposition process successfully reduced residual stresses.

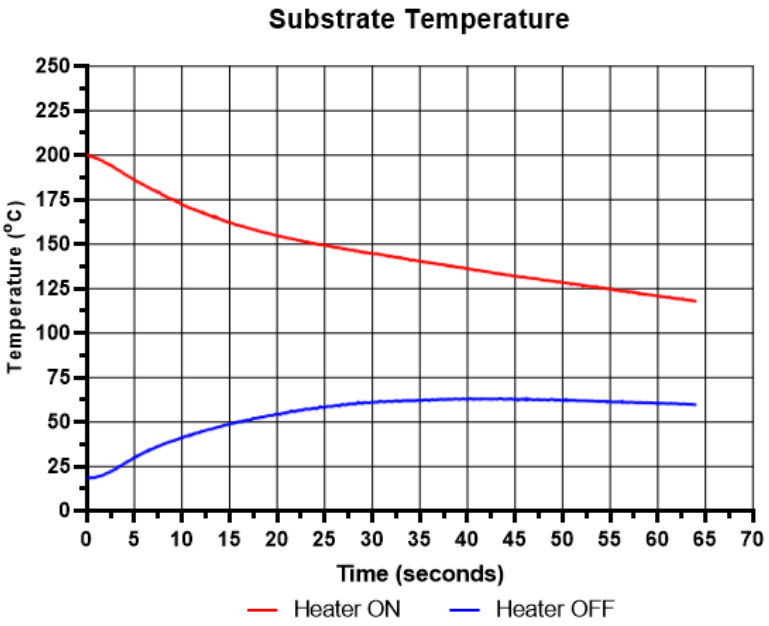

Figure 13. Substrate temperature with substrate preheating (red) and without substrate preheating (blue)

Wetting Behavior

Characterization of the coatings wetting behavior was carried out using the sessile drop method [92]. The measured static contact angle (SCA) images of all surfaces are shown in Figure 14. The Al-1 surface demonstrates the lowest SCA of 85° ± 1°, while PFA-C revealed the highest SCA of 153° ± 1°. To ensure water droplet shedding from a surface, preventing the freezing of droplets, larger SCA values such as with PFA-C are sought out.

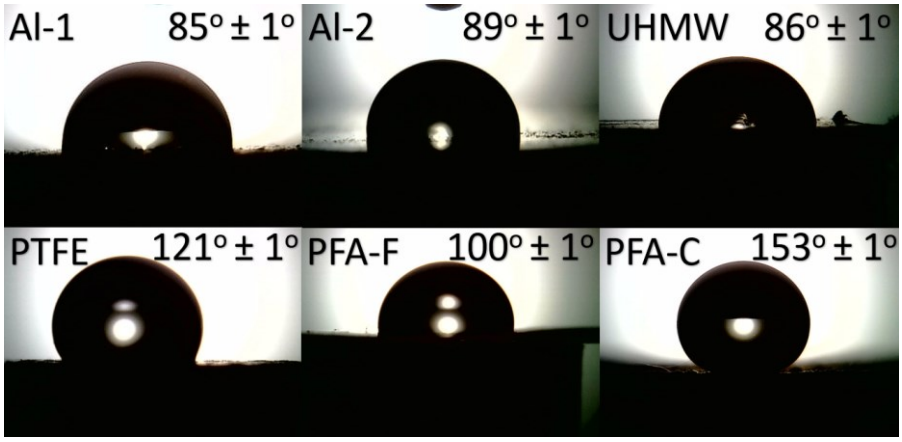

Figure 14. Static contact angles of all test surfaces

Reaching an elevated SCA generally indicates that a combination of the coating's low surface energy and surface topography contributed to its hydrophobic behavior. However, the superhydrophobicity of a surface is more readily correlated to air entrapment leading to a Cassie state [24]. Surface roughness measurements of each surface before and after the macro CATs are shown in Figure 15. The surface roughness of PTFE and PFA-C tend to confirm the presence of a Cassie state through elevated SCAs. This is not the case for UHMW and PFA-F, as shown by their lower surface roughness and smaller SCAs. In addition, it appears the low surface energy of UHMW and PFA-F does not present any advantage in increasing the SCA over the aluminum surfaces. This behavior confirms the large influence that surface roughness has on the wetting state of a surface. For the aluminum surfaces, a Cassie state was not present due to their lack of required surface hierarchy combined with the hydrophilic nature of their surface chemistry. Also shown in Figure 15 is the surface roughness of all surfaces after performing the CAT tests. Even after 15 icing cycles, the PFA-C surface presents a similar drop in surface roughness as all other surface materials, indicating a comparable surface durability.

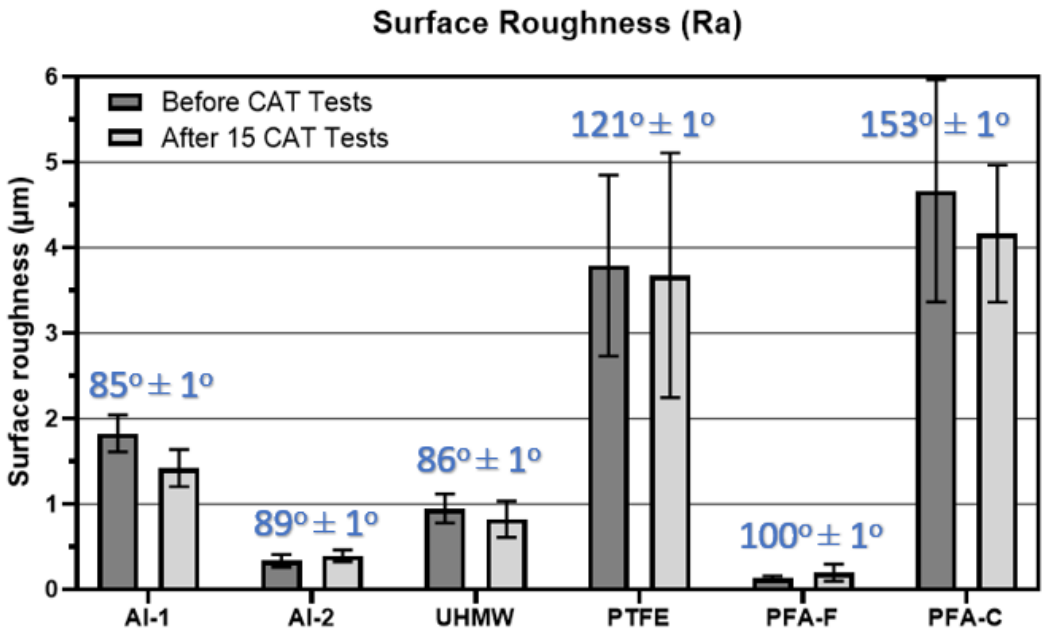

Figure 15. Surface roughness before and after 15 icing-de-icing cycles using the CAT. Static contact angles are shown in blue

The surface topography of PFA-C, shown in Figure 16, demonstrates the micro/nano-textures of the surface in its as-sprayed state. The natural surface topography of PFA-C

does present an advantage over manufactured superhydrophobic surfaces. Manufacturing processes used to create micro/nano-textures includes anodization, laser texturing, two-tiered surface texturing and chemical etching, all of which can be difficult to manufacture for large scale applications and can be quite costly [1]. The PFA-C surface does overcome these challenges by being deposited with a portable coating process and by not requiring any post-processing to achieve its superhydrophobic state.

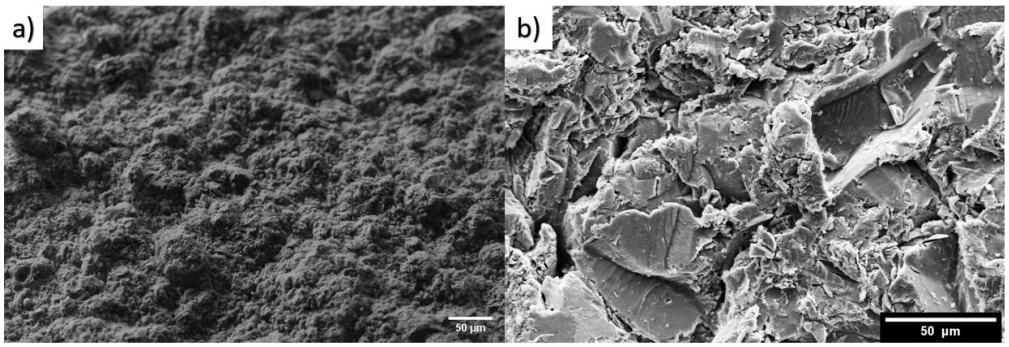

Figure 16. SEM images of as-sprayed adhesive PFA coating topography: a) micro-surface textures, b) nano-surface textures

Droplet Freezing

Results of droplet SCAs and ice growth times, for both the isothermal substrates and cooled substrates, are shown in Figure 17. Bulk polymer surfaces, PTFE and UHMW, were not included in the ice growth tests because of differences in sample thickness compared to the remaining four surfaces of interest, leading to the inability to appropriately compare ice growth times.

SCA and Frost Effect

For both aluminum surfaces, a shift in the wetting state is observed: from more hydrophilic-like on the cooled substrate to more hydrophobic-like on the isothermal substrate. It is hypothesised, based on visual observations, that this behavior is caused by the instantaneous freezing of a small layer of the water droplet as it is being deposited on the isothermal substrate: A thin layer at the interface instantaneously solidifies and acts as an initial base, supporting the remainder of the water being deposited. As the final volume of water is deposited, the surface tension of this frozen film restricts the droplet from

spreading out, resulting in a droplet that appears to be resting on a hydrophobic surface and therefore has a high SCA.

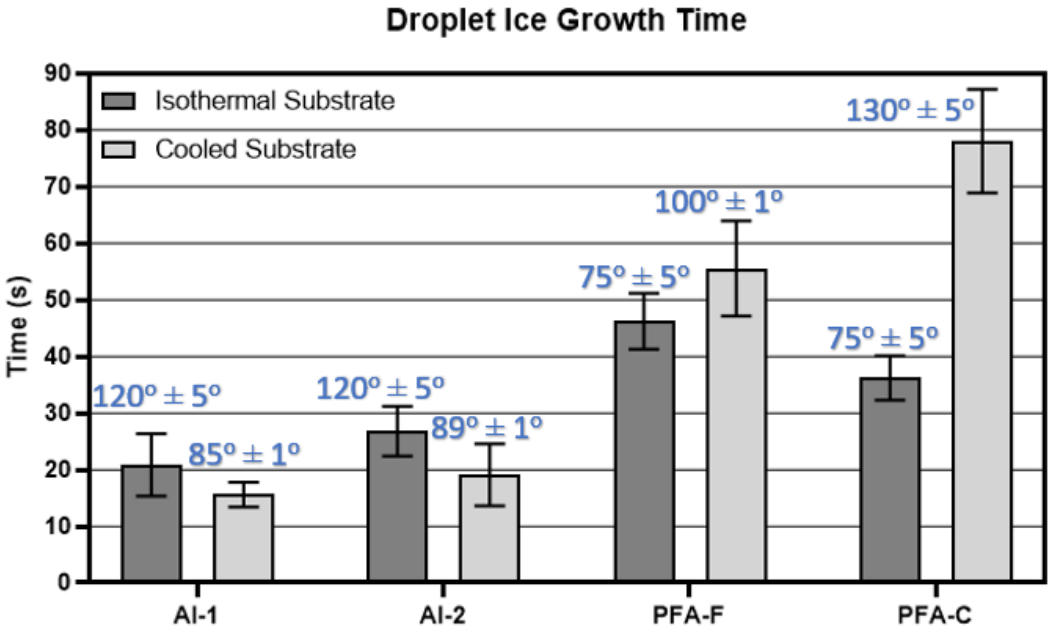

Figure 17. Droplet ice growth times for cooled substrates and isothermal substrates. Static contact angles are shown in blue

A wetting transition is also observed for PFA-F and PFA-C, however this transition was reversed: from hydrophobic/superhydrophobic-like on cooled substrates, to hydrophilic-like on isothermal substrates. Unlike the aluminum surfaces, initial freezing of water droplets on isothermal substrates was not observed visually. This is attributed to the lower thermal conduction of PFA compared to aluminum (approximately 0.2 W/m.k for PFA and 167 W/m.k for aluminum 6061). Rather, the SCA for PFA-F and PFA-C was smaller for the isothermal substrate, and larger for the cooled substrate. Such a behavior has been reported previously and is explained by the surface's sensitivity to humidity and frost formation [93]. In the isothermal substrate cases, the equilibrium period within the cryostage allowed condensation and frost growth prior to droplet deposition. As a result, for the PFA-F and PFA-C surfaces, the Cassie wetting state was compromised upon deposition of the water droplet, and instead went onto a Wenzel state leading to very low SCAs. It is believed that frost formation was also possible for the cases of cooled substrates however the influence is more subtle/gradual than with the isothermal substrates. Figure

18 demonstrates this through an observable decrease in SCA, for a droplet on PFA-C cooled substrate case, from the time the droplet had settled on the surface after deposition to the moment before ice nucleation occurred. As shown in the figure, the left image shows a water droplet with initially a SCA similar the one observed at room temperature of 153°. However, the right image shows the same droplet 72 seconds later with an approximate SCA of 130° ± 5°. The noticeable decrease in SCA during this time period suggests that frost growth led the droplet to progressively lose its superhydrophobic wetting behavior. It is hypothesized that the Cassie wetting state could have been lost in the process due to the infiltration of the cold air through surface textures leading frost to develop underneath the droplet. Frost growth under the droplet would eliminate the superhydrophobic effect by replacing the air channels and disrupting the surface tension which keeps the droplet contained and round. This hypothesis could also explain why PFA-C is the only cooled substrate surface that does not have the same SCA as it did at room temperature.

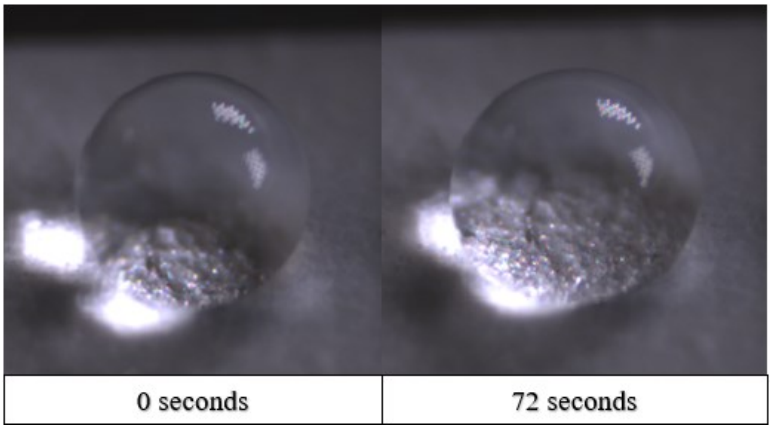

Figure 18. Effect of frost formation on the static contact angle of PFA-C, for the cooled substrate case. The left image (at zero second) shows the moment the droplet settled on the surface after deposition, and the right image at 72 seconds. A large decrease in SCA is observed.

Ice Growth Times

For the cooled substrate cases, the ice growth times for both aluminum surfaces are quite similar. Al-2 has a slightly longer solidification time than Al-1 and this is likely because of its higher SCA, associated with it slightly rougher surface. One can observe that PFA-F's ice growth time is nearly three times longer than the aluminum surfaces. In addition to having a larger SCA that reduces the heat transfer area between the droplet and cold

surface, the increase in ice growth time can be attributed to lower thermal conductivity of the polymer film, acting as an extra thermal resistance. The longest ice growth time for the cooled substrate case was on PFA-C, taking nearly four times as long as the aluminum surfaces to completely solidify. As previously discussed, and shown in Figure 17, the SCA of PFA-C is the highest of all surfaces. A high SCA leads the droplet to have a much larger area exposed to the surrounding air which has a lower thermal conductivity than the cold surface. In addition, the high SCA also decreases the contact area with the cold surface restricting the heat being transferred. As a result, the droplet's wetting behavior reducing direct contact with the cold substrate coupled with the low thermal conductivity of the PFA material led to a longer ice growth time than PFA-F, and both aluminum surfaces.

For the isothermal substrate cases, while the initial substrate temperature is lower than the cooled substrate cases, the aluminum surfaces performed similarly. Their ice growth times increased slightly, attributed to the increase in SCA created by the first layer of water freezing at deposition. The larger SCA likely led to reduced heat being transferred to the cold surface because of lower surface contact area. For the PFA-F surface, ice growth times decreased compared to the cooled substrate case. Unlike the aluminum surfaces and as exposed previously, the SCA of PFA-F decreased for the isothermal substrate case, and this led to increased contact area with the cold surface, thus reducing the ice growth time. For PFA-C, a large decrease in ice growth time was observed for the isothermal substrate case compared to the cooled substrate case. Droplets deposited on isothermal PFA-C substrates took less than half the time to solidify than on a cooled PFA-C substrate, and this is due to the spreading of the droplet which increased the contact area with the cold surface. As discussed previously, all isothermal substrates were subject to condensation and frost growth prior to the deposition of water droplets. For both PFA-F and PFA-C, the frost led to a compromised wetting behavior and the spreading of water droplets with low SCAs, resulting in more heat being transferred to the cold substrate and reduced significantly their ice growth times.

A visual progression of droplet ice growth, for both cooled substrates and isothermal substrates, can be seen in Figure 19. Considering the difference in ice growth time and SCA, for each surface and for both cases (cooled and isothermal), a ratio of ice growth

time/SCA degree can be established. For the PFA-F surface, ice growth time increased by roughly 0.5 seconds for every increase of degree in SCA. The ice growth ratio for PFA-C is approximately 0.75 seconds/degree and for the aluminum surfaces, Al-1 and Al-2's ratios were both approximately 0.2 seconds/degree each. The low ice growth ratios for Al-1 and Al-2 indicate that despite having a large difference in SCAs individually, on both cooled and isothermal substrates, ice growth time was not as heavily impacted by SCA as it was for PFA-F and PFA-C. This further confirms that the thermal conductivity of the surfaces has a greater effect on ice growth time than the SCA. For the PFA surfaces however, the conclusion is not the same. The larger ice growth ratios for PFA-F and PFA-C mean that ice growth time is much more sensitive to a change in SCA when thermal conductivity is low. The similar thickness of both PFA surfaces and their identical thermal properties also confirm that the SCA plays a much larger role in the ice growth time than it does for the aluminum surfaces.

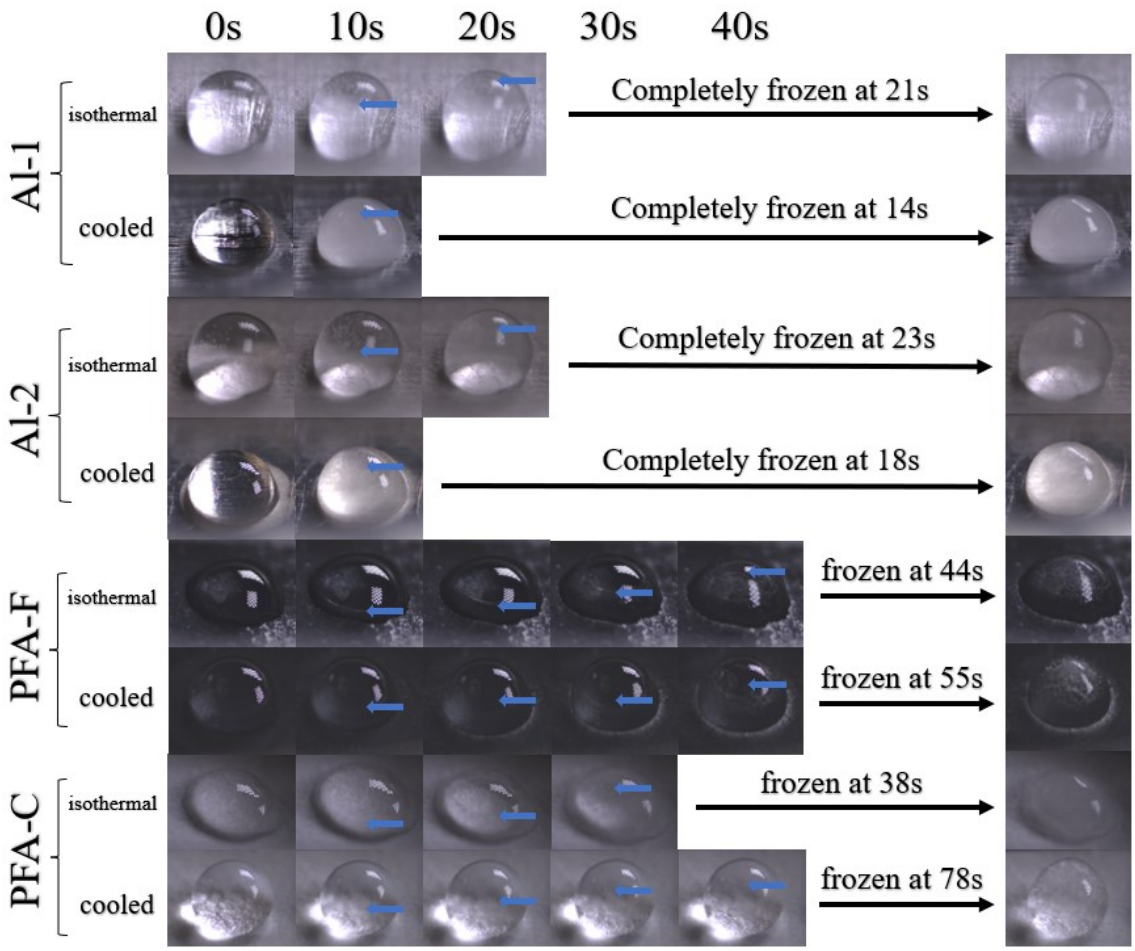

Figure 19. Ice nucleation and growth progressions for Al-1, Al-2, PFA-F and PFA-C. Horizontal blue arrows indicate the freezing front observed. Images without blue arrows indicate that either solidification had not started, or that droplets are completely frozen.

Ice Growth Types

The rationale of the observed ice growth times has been explained based on material thermal conductivity, surface textures and frost formation. However, as reported in Figure 20, various ice growth behaviors were also observed. The first growth type originates at the bottom of the droplet, at the interface with the cold test surface where a solid ice front is clearly defined and making its way upwards until it reaches the droplet apex.

The second growth type is characterized by two separate steps, the first is an extremely rapid change in droplet clarity and the second is the complete freezing of the droplet. In the first step, a sudden change in droplet clarity occurs, in less than 0.15 seconds, where the entire droplet surface appears to nucleate simultaneously. This step is hypothesized to

be linked to the recalescence stage. Due to limitations with the camera speed used in these tests, the exact first step time cannot be accurately determined. The second step consists of the solidification process, with a freezing front not as easily distinguishable as in the case of type 1, attributed to the resolution limitations with the camera and the scattering of light in the droplet.

The third growth type begins by showing surface cracking during solidification. In addition, large air bubbles can be seen in the droplet resulting in the scattering of light, making the distinction of a freezing front extremely difficult to observe.

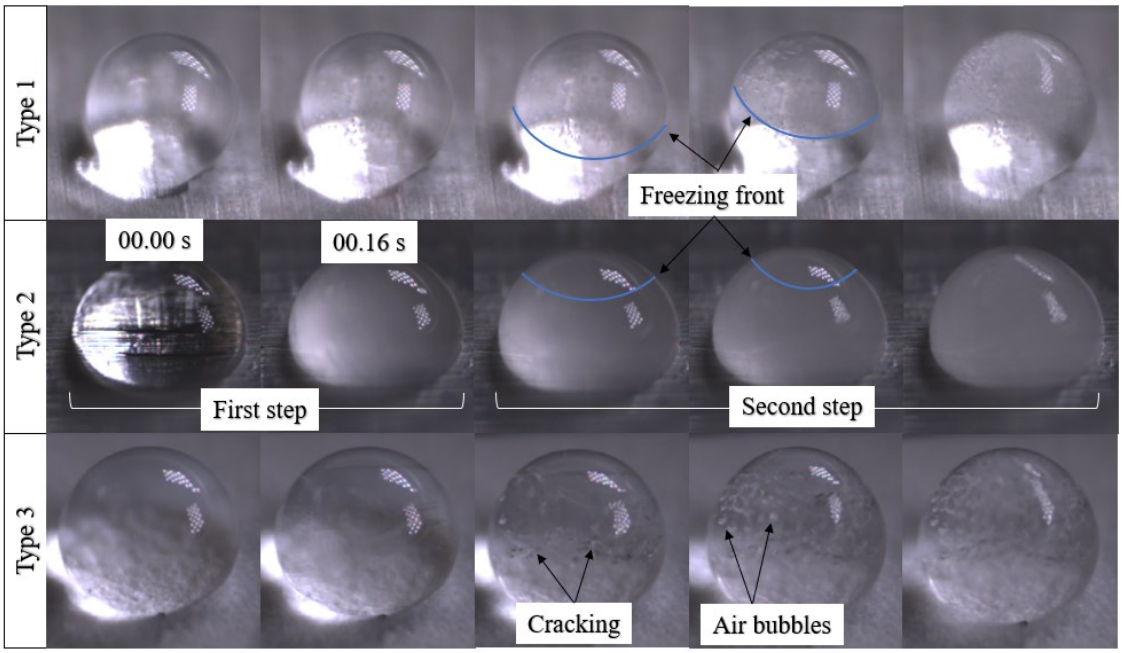

Figure 20. Three ice growth types observed within droplets

The ice growth types occurring for each individual surface material, at both test surface temperatures, are shown in Table 5.

Table 5. Ice growth types based on test surface conditions and surface materials

Surface material	Isothermal Substrates	Cooled Substrates
Al-1	Type 1	Type 2
Al-2	Type 1	Type 2
PFA-F	Type 1	Type 1
PFA-C	Type 1	Type 1, 2 and 3

The initiation of the ice growth process leading to the three different ice growth types observed experimentally has been shown to be controlled by the heat being transferred from the droplet to either the cold surface, the surrounding air, or a combination of the two [94]. In recent work by Irajizad et al. [94], predictive models were put forth demonstrating the ice growth process of water droplets in two different environments: one without air flow (droplet in stagnant air) and one with air flow. Without the presence of air flow, the ice growth process initiates at the base of the droplet, transferring heat from the droplet to the cold surface due to the higher thermal conductivity of the surface material as opposed to ambient air. As shown in Figure 21, this resulted in a freezing front traveling from the base of the droplet upwards to the droplet's apex. However, with air flowing around the droplet, the convective heat transfer from the passing air initiates the ice growth process on the droplet's outer surface resulting in a thin shell of ice growing inwards to the center of the droplet. It is hypothesized that the schematic representations of a droplet without airflow, and with airflow, accurately depict what has been observed experimentally with type 1 and type 3 ice growth.

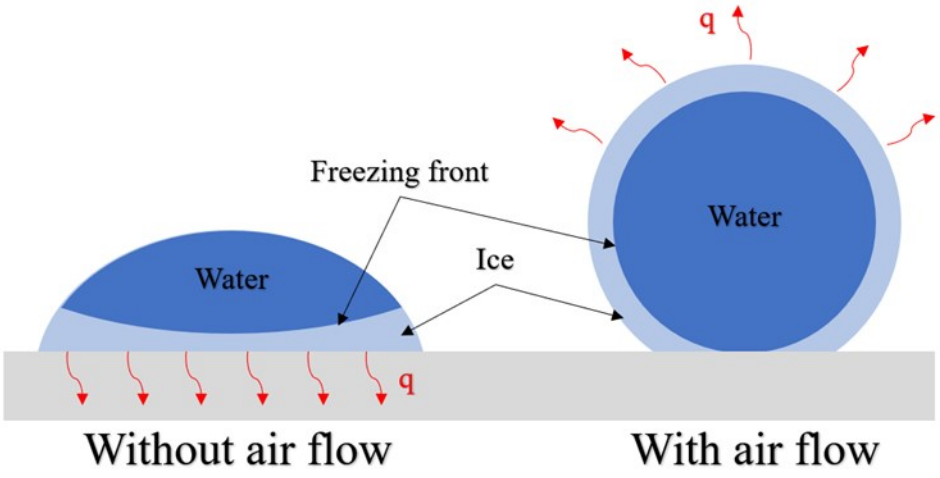

Figure 21. Ice growth behavior without airflow (left), and with air flow (right), as seen within the freezing droplet, based on [94]. Red arrows represent the direction heat is being transferred and "q" represents the heat flux.

While the results presented in this work for type 1 and type 3 align with the schematic representation shown in Figure 21, this study takes place solely in stagnant or quasi-

stagnant air (as natural convection currents possibly occur) and uses two different substrate temperature cases making it difficult to compare results. To explore further the ice growth behaviors, shown in Figure 21, and to understand how type 2 ice growth develops, a numerical model of freezing water droplets was developed, validated, and used.

First, to validate the model, the experimental results of Hou et al. have been used [95]. The experimental conditions include: a water droplet volume of 15 µL, SCA of 84.6°, and a cold surface temperature of -29.5 ℃ [82]. Modeling results used as validation step are shown in Figure 22. The freezing front height is normalized by the initial (time = 0 seconds) droplet height. The evolution of the freezing front height inside the droplet is well predicted by the current model as the freezing height and time agree with the reported experimental and numerical results [95]. Therefore, the solidification/melting model proposed is used to further understand the freezing process of the current study: 10 µL water droplets deposited on aluminum surfaces.

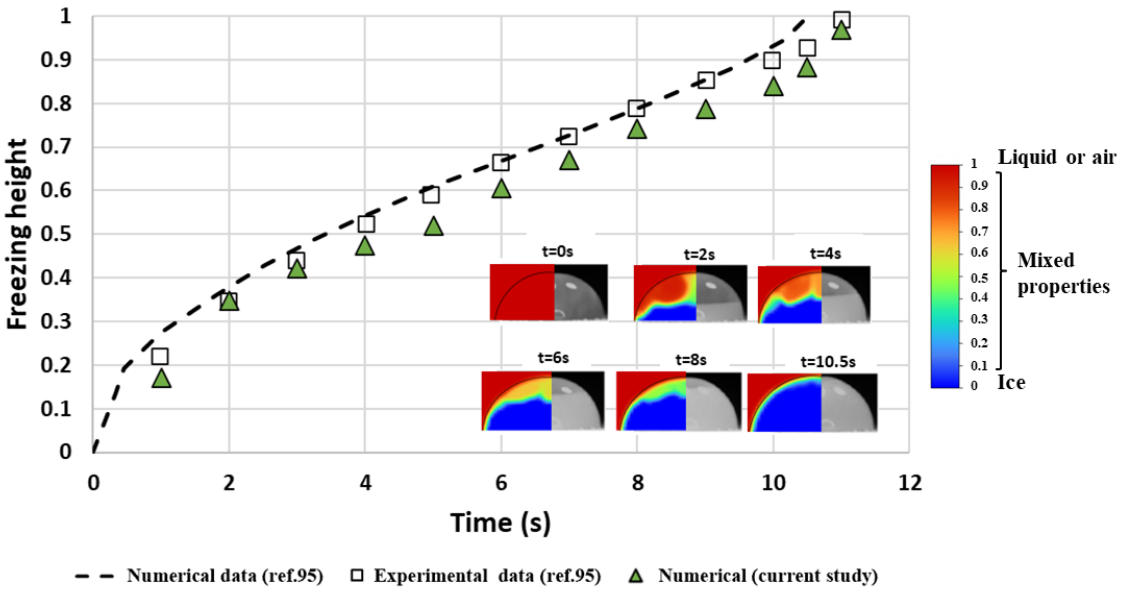

Figure 22. Evolution of the freezing front and height inside the droplet with time (a) experimental data and (b) numerical data using the current study numerical set-up.

The freezing process and the ice distribution within the 10 µL droplet at different times for both simulated cases are presented in Figure 23. A comparative analysis is conducted to extract the factors influencing the evolution of the freezing front. In both cases, once the

water droplet stabilizes into its spherical shape, it gradually freezes from the bottom to the top.

In the experimental results shown in Figure 20, it was observed that when the ice nucleation-recalescence stage starts for type 2 case on Al-1 cooled substrate, the water droplet becomes opaque. Although the surrounding environment (stagnant air) in the numerical model has been set to -10 ℃, freezing of the water droplet from its air-water interface towards the interior has not been detected for the cooled substrate case. Hence, the numerical model confirms that the change in droplet opacity is unrelated to the freezing process directionality. As noted by previous studies, if the outside layer of the droplet freezes ahead of the interior it would then break and burst due to the density decrease, which is not observed in both the experimental and numerical modeling results of type 2 [96]. Additionally, the frozen droplet surface is known to be smooth only in the case when the freezing is induced by a low temperature substrate plate.

Otherwise, if the droplet freezes due to the cold surrounding air, wrinkles would appear at the droplet surface after freezing [97]. As a wrinkled droplet surface is not observed for type 2 ice growth, these observations further validate the current numerical freezing model process and explains the experimental freezing time periods and visual differences between the isothermal substrate (type 1) and cooled substrate (type 2), as seen with Al-1.

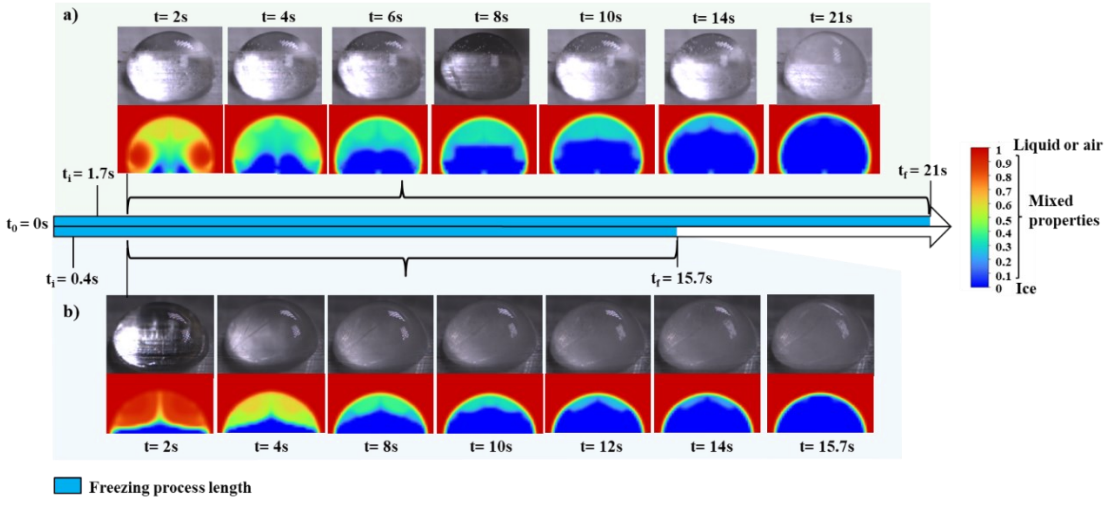

Figure 23. Water droplet solid phase fraction at different times when the substrate a) is kept constant at -10 ℃ (isothermal substrate leading to Type 1 ice growth) and b)

cooled down to -10 ℃ from room temperature (20 ℃) (cooled substrate leading to Type 2 ice growth). The first appearance of ice in both cases is indicated at time t_i. The time necessary for the droplet to reach a fully frozen state is marked as t_f in both cases.

As shown in Figure 23a, for the isothermal case, the first fraction of ice appears at 1.7 seconds. Numerical results predict a complete freezing time of 21 seconds, which agrees with the experimental values, as shown in Figure 19. For the cooled substrate case, the first volume fraction of ice appears at 0.4 seconds. The liquid droplet freezes completely after 15.7 seconds, as shown in Figure 23b, which is 1.7 seconds slower than observed experimentally. Disregarding the supercooling state of the droplet and the presence of a possible liquid-ice mixture at the start of the freezing stage in the numerical model can be the cause of the observed deviation. Obviously, the lower the initial water droplet temperature, the faster is the droplet freezing process. Since ice has a higher thermal conductivity than water, an initial presence of ice in the water droplet results in a faster heat transfer [27]. Similarly, the perfect agreement between the numerical and experimental results for the isothermal case suggests an absence of an ice-liquid mixture at the start of the freezing stage. This distinction between the two cases may lead to the experimentally observed difference in droplet transparency. Different explanations have been given in the literature to clarify the droplet opaque characteristic, with one being the scattering of light due to the partially solidified water droplet [98], [99]. This change in opacity has been described to occur at the nucleation/recalescence stage as the droplet changes suddenly to a water-ice mixture due to its supercooled sate. In the current study experiment, the change in droplet transparency from a clear to opaque state also occurs within a fraction of seconds after the nucleation stage, as shown in Figure 20. This suggests that type 2 ice growth is more closely related to type one, rather than being a direct combination of types 1 and 3. Despite the change in droplet transparency, the droplet is yet to complete the solid phase transition, as observed experimentally and as shown by the numerical model.

Figure 24 depicts the temperature contour within the droplet during the freezing stage for both modeled cases. During solidification, the temperature in the liquid is kept close to 0

°C. At the end of the freezing stage, the temperature in the frozen droplet varies from -10 °C at the lower boundary to 0 °C at the top of the droplet. The temperature contours confirm, once again, that the temperature of the cold plate has a greater effect on freezing than the cold quiescent surrounding air.

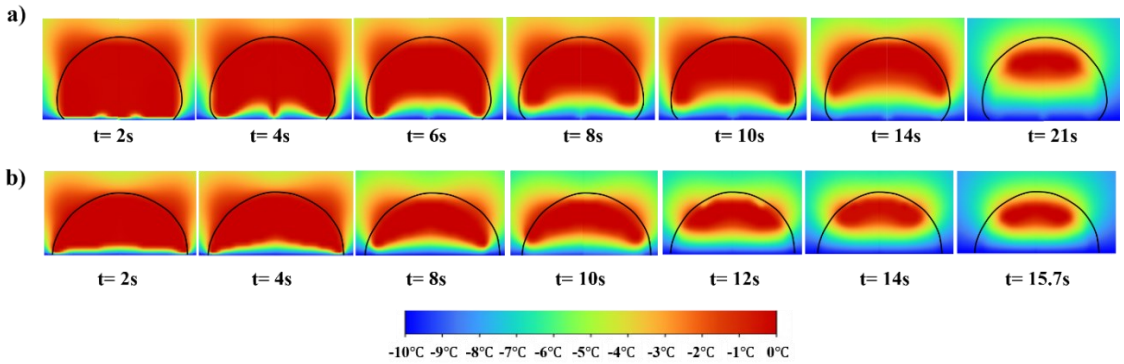

Figure 24. Temperature contour inside the droplet at different times when the substrate a) is kept constant at -10 °C (isothermal substrate) and b) cooled down to -10 °C from room temperature (20 °C) (cooled substrate). The droplet size and geometry is traced in black.

The type 3 ice growth, which occurred exclusively with PFA-C, does appear to demonstrate potential cracking and more prominent air "bubbles" present throughout the droplet. These observations are consistent with rapidly freezing water at the air-water interface that can occur when freezing through the water-surface interface is comparably slower. As previously mentioned, the lower thermal conductivity of the PFA-C surface and the high SCA of the droplet would decrease the rate of heat transfer between the droplet and surface, thereby increasing the heat transfer between the droplet and air. These results confirm the importance in sustaining very high SCAs to obtain type 3 ice growth, as it could be beneficial to the surface's icephobicity. If droplets begin to crack during solidification, this will compromise the ice's mechanical integrity and facilitate the shedding of ice from the surface.

Ice Adhesion

The final aspect of icephobic coatings is being able to mitigate ice adhesion, acting as the last line of defense, after hydrophobicity and freezing time, to prevent the accumulation of ice. To characterize the ice adhesion strength over a large ice covered surface, the common macro CAT method was used [75]–[77]. The mean ice adhesion strengths for each surface, using the CAT, are shown in Figure 25.

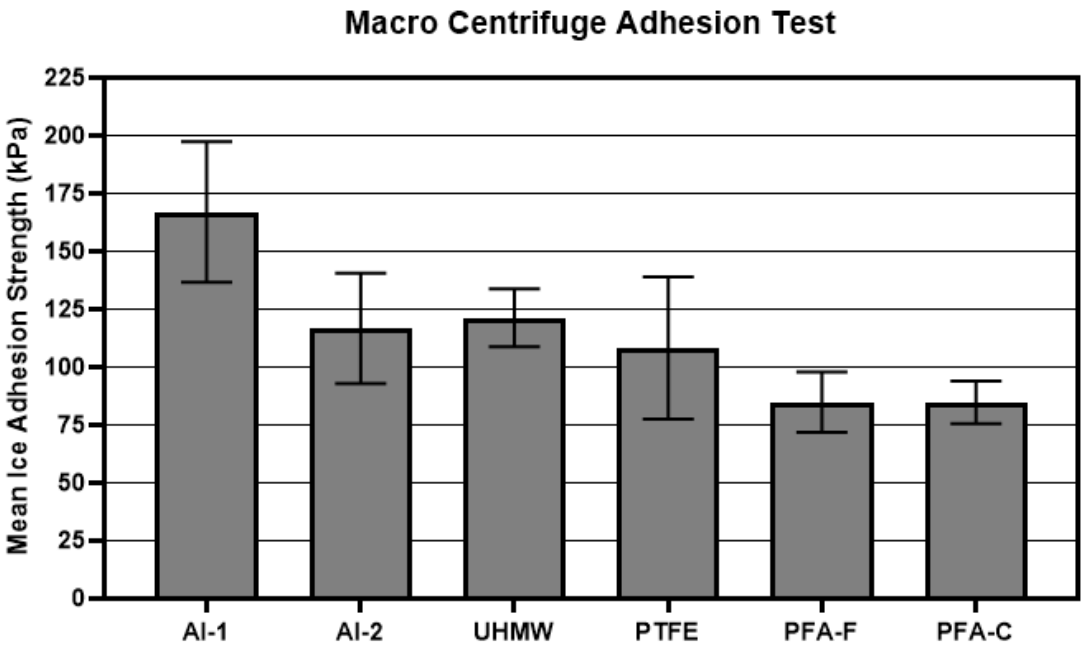

Figure 25. Mean ice adhesion strength, in kPa, obtained through the macro centrifuge adhesion test for large ice-covered test surfaces

The surface with the highest ice adhesion strength was Al-1, and the surfaces with the lowest ice adhesion strength were PFA-C and PFA-F with almost identical values. Previous work has shown that lowering the ice adhesion strength of a surface can be accomplished by reducing overall surface roughness [35], [100]. The reduction in surface roughness leads to lower ice adhesion strength due to the lack of mechanical anchoring at the iced interface. This is also observed in this work with Al-1 and Al-2, confirming that for two identical materials, the one with a lower surface roughness leads to lower ice adhesion strength. However, this is not observed for PFA-F and PFA-C, with their ice adhesion strengths nearly identical, despite having a large difference in surface roughness (larger than the two aluminum samples) that should lead to a lower adhesion strength for PFA-F. This behavior

is explained by the existence of Cassie ice [11], [101] on PFA-C. A Cassie wetting state occurred on PFA-C due to its surface asperities and topographical hierarchy, leading to the entrapment of air, causing water droplets to be held above the surface without wetting it completely. As a result, once solidified, the ice sits above the surface's micro/nano-textures and has less contact with the interface leading to reduced ice anchoring. The presence of air entrapment and subsequent Cassie ice is traced back to the ice formation method being used for the CAT, shown in Figure 26. When filling the ice cube trays with water, air is believed to become entrapped at the coating surface asperities and cannot find a way to escape, causing an artificial Cassie wetting state. This wetting state then remains throughout the solidification process prior to CAT testing. The likelihood of a sustained Cassie state in real life conditions, such as when droplets impact a surface, is unlikely, rendering these results the best-case scenario for the as-sprayed PFA-C surface.

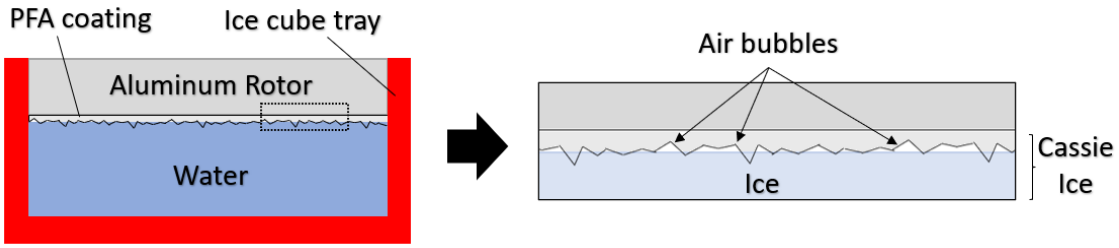

Figure 26. Ice formation method for centrifuge adhesion test displaying air bubbles on the surface of PFA-C

The likely formation of Cassie ice indicates that characterizing the icephobic performance of PFA-C with only the macro CAT data is not representative of real world applications. To examine the icephobic behavior without the presence of Cassie ice, micro shear tests are used to analyze single droplet ice adhesion.

Due to the camera angle and limitations of the micro shear test setup, the surface area at the surface/droplet interface could not be determined accurately, preventing the calculation of ice adhesion strength. Therefore, results are presented as the required force to detach individual droplets from the surface and shown in Figure 27. Bulk polymers, UHMW and PTFE, are not included in the micro shear tests due to differences in sample thickness causing different ice growth times and subsequent inconsistencies in ice crystalline

structures which could impact ice detachment force (the same reasons as outlined for exclusion of these surfaces from the previous section).

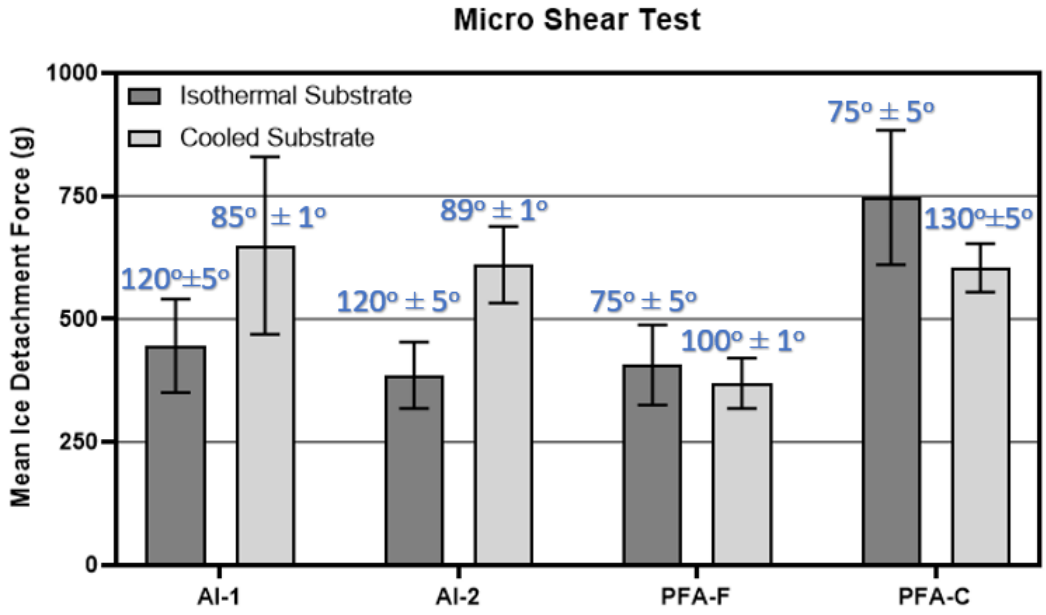

Figure 27. Mean ice detachment force, in grams, obtained through the micro shear test for single droplets. Static contact angles are shown in blue

For the aluminum surfaces, a clear increase in detachment force can be observed when the SCA is decreased (cooled substrate cases). This behavior can be attributed to the increased surface area at the surface/droplet interface. This can also be explained by the type of adhesion the surface is experiencing. Ice adhesion has four adhesion mechanisms all working simultaneously: covalent or chemical bonds, electromagnetic interactions, electrostatic interactions and mechanical bonds, with the latter two mechanisms having the largest influence on overall adhesion [37]. Electrostatic bonding is most prominent with metallic materials because of their inability to act as an electrical insulator, which creates mirrored surface charges with the ice and thus increases adhesion [7]. For this reason, an increase in contact area induces more electrostatic bonding for the aluminum surfaces leading to much higher ice detachment forces. However, due to the low surface roughness of both aluminum surfaces, it is expected that no significant mechanical bonding was experienced, therefore leading to similar forces required for both aluminum substrates.

Unlike the aluminum surfaces, PFA is considered to have dielectric properties minimizing electrostatic interactions. Therefore, when the SCA of PFA-F decreased, a large increase

in ice detachment force was not observed even with a larger surface area. In addition, PFA-F has the lowest surface roughness of all surfaces and therefore will experience the less mechanical bonding, which also coincides with very consistent ice detachment forces.

As seen in Figure 27, the ice detachment force of PFA-C behaves like the aluminum surfaces by increasing when its SCA decreased. The cooled PFA-C substrate has approximately the same ice detachment force as both aluminum surfaces, however the bonding mechanism involved is different. Due to the dielectric properties of PFA, electrostatic interactions are not of importance and bonding is rather associated to mechanical anchoring. As hypothesized for the freezing of droplets on PFA-C, for cooled substrates, the Cassie wetting state is believed to have been lost prior to freezing. As a result, the droplet infiltrated the surface textures of PFA-C thus transitioning to the Wenzel state. The resulting ice was then able to interlock with the coating's surface features, resembling what occurs with Velcro®, and leads to higher ice detachment forces. The formation of Wenzel ice in the micro shear test demonstrates a more representative and realistic approach to characterizing ice adhesion as opposed to the Cassie ice seen in the macro CAT.

To compare the performance of all surfaces in both the macro CAT and micro shear tests, the ARF is used as a ratio between the reference surface (Al-1) and other surfaces. Results of the ARF comparison are presented in Figure 28.

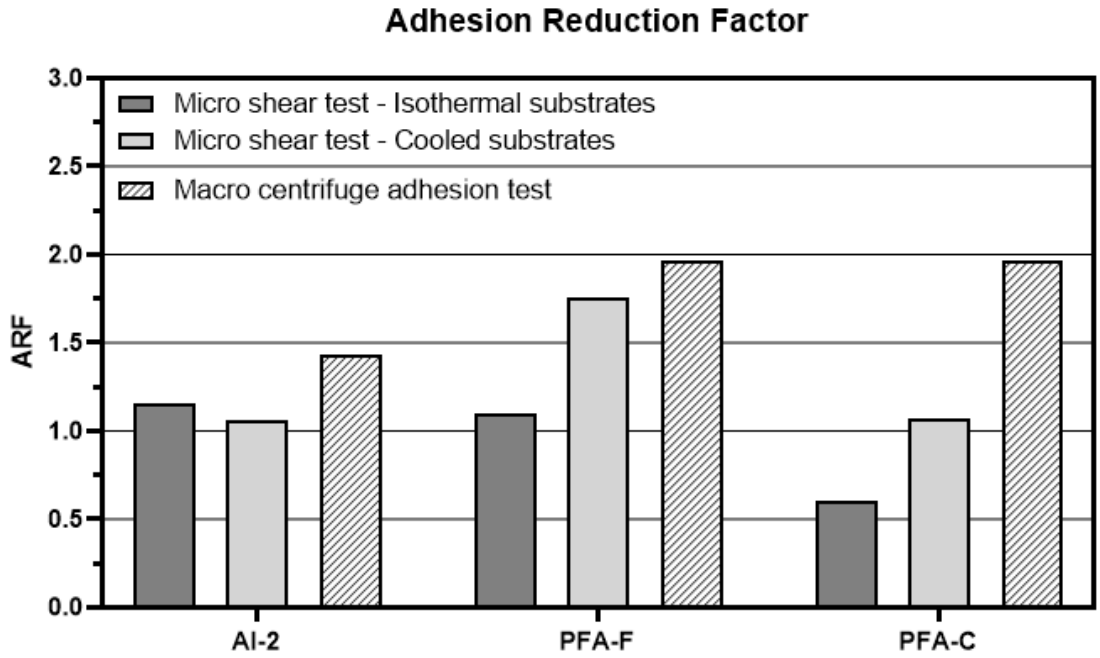

Figure 28. Adhesion reduction factor comparison for the micro shear test and macro centrifuge adhesion test. Reference material used for ARF calculation is Al-1.

The aluminum surface, Al-2, appears to remain somewhat constant across all ice testing methods with an ARF averaging around 1.25. Its ARF being above 1 can be justified by the lower surface roughness than the reference material leading to overall lower ice adhesion. The performance of PFA-F varies from an ARF of approximately 1 with the micro shear test on isothermal substrate, 1.75 on cooled substrate, and nearly 2 with the macro CAT. The low ARF value, seen in the micro shear test on isothermal substrate, can be explained by the initial freezing of water droplets on Al-1 leading to a high SCA and a low contact area. If the initial freezing of the first layer of water had not occurred, it is reasonable to assume that the ARF of PFA-F would be similar to the cooled substrate micro shear test based on its lower electrostatic and mechanical bonding properties than Al-1. The ARF for PFA-C experiences the largest fluctuations among all other surfaces. For the micro shear test, at -10 ℃, its ARF is below 1, which means it had higher ice adhesion than the reference material, Al-1. For both micro shear tests, the PFA-C surface experienced mechanical anchoring with ice due to the loss of the Cassie wetting state which led to high ice adhesion values. In the macro CAT, PFA-C obtained a much higher ARF value, however the ice adhesion was based on Cassie ice, which, as previously explained, is highly unlikely to occur in practical applications and is therefore not an accurate representation of

its icephobic performance. Due to the mechanical bonding experienced by PFA-C in both micro shear tests, the PFA-F surface appears to have performed the best and is the most icephobic based on these results.

Conclusion

Deposition of an adhesive PFA coating on an aluminum substrate was successfully carried out using the CS process through a novel nozzle design. The icephobic performance of the as-sprayed coating was assessed and compared to various polymers and aluminum surfaces in three-fold characterization tests. Firstly, wetting behavior of single droplets was evaluated, secondly static contact angles, ice growth times, ice growth types, and the effect of frost on isothermal and cooled substrates were recorded, and lastly ice adhesion tests at both micro and macro scales were performed. Conclusions from this work are:

- The use of a specifically designed nozzle, rather than a commercial nozzle, resulted in higher particle impact temperatures and velocities while using the same gas processing conditions, improving coating quality and increasing deposit thickness.
- The as-sprayed PFA coating demonstrates a superhydrophobic behavior, at room temperature, due to its complex surface hierarchy causing a Cassie wetting state.
- Single droplet analysis, on both isothermal and cooled substrates, revealed that the PFA coating's wetting state is greatly influenced by frost formation. The presence of frost on the coating's surface resulted in the loss of the Cassie wetting state and led to decreased ice growth time. The as-sprayed PFA coating outperformed the aluminum surfaces for the isothermal and cooled substrate cases, however it underperformed as a cooled substrate compared to the bulk PFA film.
- Overall, ice growth time is more heavily influenced by the thermal conductivity of a surface than the SCA. However, obtaining a high SCA will slow the process down. As a result, the most effective way to increase the ice growth time is to combine low thermal conductivity with a high SCA at time of freeze.
- Modeling has shown that the ice front develops from the substrate surface towards the top of the droplet, whether the substrate is in an isothermal state or a cooled state.

- Visual observations made in ice growth types 1 and 2 do not directly influence ice growth time, as shown by the modelling. They are rather a function of substrate temperature and SCA at time of freeze leading to different recalescence behaviors.
- Ice adhesion for the PFA coating and PFA film were very similar in the macro centrifuge adhesion tests, and both outperformed the aluminum surfaces. In the micro shear tests, the as-sprayed PFA coating underperformed due to the presence of frost, which led to increased ice adhesion from the Wenzel wetting state at time of freeze. The application of the as-sprayed PFA coating can effectively reduce ice adhesion, however only when a Cassie wetting state can be sustained throughout the freezing process, and if frost is avoided. Therefore, for practicality in real world applications, the PFA coating should not be used in its as-sprayed state but rather with a polished surface finish resembling the PFA-F, used in this work.

Acknowledgements

The authors wish to acknowledge the University of Ottawa technicians; Michael Murphy, Ian Myers, Paul Burberry, Leo Denner, Jacques Audet, James Kent, and Stanley Weedmark, for their help in manufacturing the various testing equipment.

References

[1] X. Huang et al., “A survey of icephobic coatings and their potential use in a hybrid coating/active ice protection system for aerospace applications,” Prog. Aerosp. Sci., vol. 105, no. July 2018, pp. 74–97, 2019, doi: 10.1016/j.paerosci.2019.01.002.

[2] N. Dalili, A. Edrisy, and R. Carriveau, “A review of surface engineering issues critical to wind turbine performance,” Renew. Sustain. Energy Rev., vol. 13, no. 2, pp. 428–438, 2009, doi: 10.1016/j.rser.2007.11.009.

[3] M. Farzaneh, Atmospheric Icing of Power Networks, vol. 84. 2008.

[4] J. L. Laforte, M. A. Allaire, and J. Laflamme, “State-of-the-art on power line de-icing,” Atmos. Res., vol. 46, no. 1–2, pp. 143–158, 1998, doi: 10.1016/S0169-8095(97)00057-4.

[5] T. Rashid, H. A. Khawaja, and K. Edvardsen, “Review of marine icing and anti- / de-icing systems,” vol. 4177, 2016, doi: 10.1080/20464177.2016.1216734.

[6] J. Norrman, M. Eriksson, and S. Lindqvist, “Relationships between road slipperiness , traffic accident risk and winter road maintenance activity,” vol. 15, pp. 185–193, 2000.

[7] R. Ramachandran, M. Kozhukhova, K. Sobolev, and M. Nosonovsky, “Anti-icing superhydrophobic surfaces: Controlling entropic molecular interactions to design novel icephobic concrete,” Entropy, vol. 18, no. 4, 2016, doi: 10.3390/e18040132.

[8] W. Tobiasson, J. Buska, and A. Greatorex, “Ventilating attics to minimize icings at eaves,” vol. 21, pp. 6–11, 1994.

[9] F. T. Lynch and A. Khodadoust, “Effects of ice accretions on aircraft aerodynamics,” vol. 37, no. 2001, pp. 669–767, 2002.

[10] O. Parent and A. Ilinca, “Anti-icing and de-icing techniques for wind turbines : Critical review,” Cold Reg. Sci. Technol., vol. 65, no. 1, pp. 88–96, 2011, doi: 10.1016/j.coldregions.2010.01.005.

[11] A. J. Meuler, G. H. McKinley, and R. E. Cohen, “Exploiting topographical texture to impart icephobicity,” ACS Nano, vol. 4, no. 12, pp. 7048–7052, 2010, doi: 10.1021/nn103214q.

[12] Y. Maly et al., “A survey of icephobic coatings and their potential use in a hybrid coating/active ice protection system for aerospace applications,” Nature, vol. 15, no. May, pp. 443–447, 2013, doi: 10.1016/j.paerosci.2019.01.002.

[13] N. Sharifi, A. Dolatabadi, M. Pugh, and C. Moreau, “Anti-icing performance and durability of suspension plasma sprayed TiO2 coatings,” Cold Reg. Sci. Technol., vol. 159, no. December 2018, pp. 1–12, 2019, doi: 10.1016/j.coldregions.2018.11.018.

[14] Y. Shen, X. Wu, J. Tao, C. Zhu, Y. Lai, and Z. Chen, “Icephobic materials: Fundamentals, performance evaluation, and applications,” Prog. Mater. Sci., vol. 103, no. January 2018, pp. 509–557, 2019, doi: 10.1016/j.pmatsci.2019.03.004.

[15] F. Veronesi, G. Boveri, J. Mora, A. Corozzi, and M. Raimondo, “Icephobic properties of anti-wetting coatings for aeronautical applications,” Surf. Coat. Technol., vol. 421, no. May, 2021.

[16] H. Niemelä-Anttonen et al., “Icephobicity of Slippery Liquid Infused Porous Surfaces under Multiple Freeze–Thaw and Ice Accretion–Detachment Cycles,” Adv. Mater. Interfaces, vol. 5, no. 20, pp. 1–8, 2018, doi: 10.1002/admi.201800828.

[17] Y. Maly and H. Koivuluoto, “Cold Sprayed SLIPS Coatings: A pathway towards process optimization and icepho- bicity,” no. May, 2020.

[18] P. W. Wilson et al., “Inhibition of ice nucleation by slippery liquid-infused porous surfaces (SLIPS),” Phys. Chem. Chem. Phys., vol. 15, no. 2, pp. 581–585, 2013, doi: 10.1039/c2cp43586a.

[19] K. Golovin, S. P. R. Kobaku, D. H. Lee, E. T. DiLoreto, J. M. Mabry, and A. Tuteja, “Designing durable icephobic surfaces,” Sci. Adv., vol. 2, no. 3, 2016, doi: 10.1126/sciadv.1501496.

[20] M. Mohseni, Z. A. Dijvejin, and K. Golovin, “Designing scalable elastomeric anti-fouling coatings: Shear strain dissipation via interfacial cavitation,” J. Colloid Interface Sci., vol. 589, pp. 556–567, 2021, doi: 10.1016/j.jcis.2021.01.019.

[21] S. Milles, M. Soldera, B. Voisiat, and A. F. Lasagni, “Fabrication of superhydrophobic and ice-repellent surfaces on pure aluminium using single and multiscaled periodic textures,” Sci. Rep., vol. 9, no. 1, pp. 1–13, 2019, doi: 10.1038/s41598-019-49615-x.

[22] S. Farhadi, M. Farzaneh, and S. A. Kulinich, “Anti-icing performance of superhydrophobic surfaces,” Appl. Surf. Sci., vol. 257, no. 14, pp. 6264–6269, 2011, doi: 10.1016/j.apsusc.2011.02.057.

[23] L. Cao, A. K. Jones, V. K. Sikka, J. Wu, and D. Gao, “Anti-Icing superhydrophobic coatings,” Langmuir, vol. 25, no. 21, pp. 12444–12448, 2009, doi: 10.1021/la902882b.

[24] S. Jung, M. Dorrestijn, D. Raps, A. Das, C. M. Megaridis, and D. Poulikakos, “Are superhydrophobic surfaces best for icephobicity?,” Langmuir, vol. 27, no. 6, pp. 3059–3066, 2011, doi: 10.1021/la104762g.

[25] K. K. Varanasi, T. Deng, J. D. Smith, M. Hsu, and N. Bhate, “Frost formation and ice adhesion on superhydrophobic surfaces,” Appl. Phys. Lett., vol. 97, no. 23, 2010, doi: 10.1063/1.3524513.

[26] J. Chen, J. Liu, and M. He, “Superhydrophobic surfaces cannot reduce ice adhesion,” Appl. Phys. Lett., vol. 111603, no. June 2012, pp. 95–98, 2012.

[27] Y. Wang, L. Ju, and D. Han, “Numerical investigation of the impacting and freezing process of a single supercooled water droplet ARTICLES YOU MAY BE INTERESTED IN,” Phys. Fluids, vol. 33, p. 42114, 2021, doi: 10.1063/5.0048206.

[28] J. P. Hindmarsh, A. B. Russell, and X. D. Chen, “Experimental and numerical analysis of the temperature transition of a freezing food solution droplet,” Chem. Eng. Sci., vol. 59, no. 12, pp. 2503–2515, 2004, doi: 10.1016/j.ces.2004.03.007.

[29] G. Chaudhary and R. Li, “Freezing of water droplets on solid surfaces: An experimental and numerical study,” Exp. Therm. Fluid Sci., vol. 57, pp. 86–93, 2014, doi: 10.1016/j.expthermflusci.2014.04.007.

[30] H. Koivuluoto, C. Stenroos, M. Kylmälahti, M. Apostol, J. Kiilakoski, and P. Vuoristo, “Anti-icing Behavior of Thermally Sprayed Polymer Coatings,” J. Therm. Spray Technol., vol. 26, no. 1–2, pp. 150–160, 2017, doi: 10.1007/s11666-016-0501-x.

[31] R. Menini and M. Farzaneh, “Elaboration of Al2O3/PTFE icephobic coatings for protecting aluminum surfaces,” Surf. Coatings Technol., vol. 203, no. 14, pp. 1941–1946, 2009, doi: 10.1016/j.surfcoat.2009.01.030.

[32] R. Menini, Z. Ghalmi, and M. Farzaneh, “Highly resistant icephobic coatings on aluminum alloys,” Cold Reg. Sci. Technol., vol. 65, no. 1, pp. 65–69, 2011, doi: 10.1016/j.coldregions.2010.03.004.

[33] V. Donadei, H. Koivuluoto, E. Sarlin, and P. Vuoristo, “Lubricated icephobic coatings prepared by flame spraying with hybrid feedstock injection,” Surf. Coatings Technol., vol. 403, no. July, p. 126396, 2020, doi: 10.1016/j.surfcoat.2020.126396.

[34] S. A. Kulinich, M. Honda, A. L. Zhu, A. G. Rozhin, and X. W. Du, “The icephobic performance of alkyl-grafted aluminum surfaces,” Soft Matter, vol. 11, no. 5, pp. 856–861, 2015, doi: 10.1039/c4sm02204a.

[35] K. Maghsoudi, E. Vazirinasab, G. Momen, and R. Jafari, “Icephobicity and durability assessment of superhydrophobic surfaces: The role of surface roughness and the ice adhesion measurement technique,” J. Mater. Process. Technol., vol. 288, no. July 2020, p. 116883, 2021, doi: 10.1016/j.jmatprotec.2020.116883.

[36] S. Yang, Q. Xia, L. Zhu, J. Xue, Q. Wang, and Q. Chen, “Research on the icephobic properties of fluoropolymer-based materials,” Appl. Surf. Sci., vol. 257, no. 11, pp. 4956–4962, 2011, doi: 10.1016/j.apsusc.2011.01.003.

[37] I. A. Ryzhkin and V. F. Petrenko, “Physical mechanisms responsible for ice adhesion,” J. Phys. Chem. B, vol. 101, no. 32, pp. 6267–6270, 1997, doi: 10.1021/jp9632145.

[38] L. E. Raraty and D. Tabor, “The Adhesion and Strength Properties of Ice,” in Proceedings of the Royal Society A: Mathematical, Physical and Engineering Sciences, 1957, vol. 245, no. 1241, pp. 184–201, [Online]. Available: http://www.jstor.org/stable/2414705.

[39] L. Makkonen, “Ice adhesion - Theory, measurements and countermeasures,” J. Adhes. Sci. Technol., vol. 26, no. 4–5, pp. 413–445, 2012, doi: 10.1163/016942411X574583.

[40] P. M. Winter et al., Polymer Coatings. 2012.

[41] H. Koivuluoto, E. Hartikainen, and H. Niemelä-Anttonen, “Thermally sprayed coatings: Novel surface engineering strategy towards icephobic solutions,” Materials (Basel)., vol. 13, no. 6, 2020, doi: 10.3390/ma13061434.

[42] V. Donadei, H. Koivuluoto, E. Sarlin, and P. Vuoristo, “Icephobic Behaviour and Thermal Stability of Flame-Sprayed Polyethylene Coating: The Effect of Process Parameters,” J. Therm. Spray Technol., vol. 29, no. 1–2, pp. 241–254, 2020, doi: 10.1007/s11666-019-00947-0.

[43] L. Pawlowski, The Science and Engineering of Thermal Spray Coatings: Second Edition. 2008.

[44] A. Lopera-Valle and A. McDonald, “Application of Flame-Sprayed Coatings as Heating Elements for Polymer-Based Composite Structures,” vol. 24, no. October, pp. 1289–1301, 2015, doi: 10.1007/s11666-015-0302-7.

[45] L. Ajdelsztajn, A. Zúñiga, B. Jodoin, and E. J. Lavernia, “Cold gas dynamic spraying of a high temperature Al alloy,” Surf. Coatings Technol., vol. 201, no. 6, pp. 2109–2116, 2006, doi: 10.1016/j.surfcoat.2005.06.001.

[46] T. B. Bush, Z. Khalkhali, V. Champagne, D. P. Schmidt, and J. P. Rothstein, “Optimization of Cold Spray Deposition of High-Density Polyethylene Powders,” J. Therm. Spray Technol., vol. 26, no. 7, pp. 1548–1564, 2017, doi: 10.1007/s11666-017-0627-5.

[47] K. Ravi, W. L. Sulen, C. Bernard, Y. Ichikawa, and K. Ogawa, “Fabrication of micro-/nano-structured super-hydrophobic fluorinated polymer coatings by cold-spray,” Surf. Coatings Technol., vol. 373, no. February, pp. 17–24, 2019, doi: 10.1016/j.surfcoat.2019.05.078.

[48] Z. Khalkhali and J. P. Rothstein, “Characterization of the cold spray deposition of a wide variety of polymeric powders,” Surf. Coatings Technol., vol. 383, no. September 2019, p. 125251, 2020, doi: 10.1016/j.surfcoat.2019.125251.

[49] W. Lock, S. Kesavan, C. Bernard, Y. Ichikawa, and K. Ogawa, “Deposition Mechanism Analysis of Cold-Sprayed Fluoropolymer Coatings and Its Wettability Evaluation,” J. Therm. Spray Technol., vol. 29, no. 7, pp. 1643–1659, 2020, doi: 10.1007/s11666-020-01059-w.

[50] R. Fernandez and B. Jodoin, “Cold Spray Aluminum–Alumina Cermet Coatings: Effect of Alumina Morphology,” J. Therm. Spray Technol., vol. 28, no. 4, pp. 737–755, 2019, doi: 10.1007/s11666-019-00845-5.

[51] A. Vardelle et al., “The 2016 Thermal Spray Roadmap,” J. Therm. Spray Technol., vol. 25, no. 8, pp. 1376–1440, 2016, doi: 10.1007/s11666-016-0473-x.

[52] A. Papyrin, V. Kosarev, S. Klinkov, V. M. Fomin, and A. Alkhimov, Cold Spray Technology. Elsevier, 2007.

[53] K. Ravi, Y. Ichikawa, K. Ogawa, T. Deplancke, O. Lame, and J. Cavaille, “Mechanistic Study and Characterization of Cold-Sprayed Ultra-High Molecular Weight Polyethylene-Nano-Ceramic Composite Coating,” vol. 25, no. January, pp. 160–169, 2016, doi: 10.1007/s11666-015-0332-1.

[54] K. Ravi, Y. Ichikawa, T. Deplancke, K. Ogawa, O. Lame, and J. Y. Cavaille, “Development of Ultra-High Molecular Weight Polyethylene (UHMWPE) Coating by

Cold Spray Technique," J. Therm. Spray Technol., vol. 24, no. 6, pp. 1015–1025, 2015, doi: 10.1007/s11666-015-0276-5.

[55] C. Liu, L. Ren, R. D. Arnell, and J. Tong, "Abrasive wear behavior of particle reinforced ultrahigh molecular weight polyethylene composites," WEAR, 1999.

[56] E. Kontou and M. Niaounakis, "Thermo-mechanical properties of LLDPE / SiO 2 nanocomposites," vol. 47, pp. 1267–1280, 2006, doi: 10.1016/j.polymer.2005.12.039.

[57] P. Bhimaraj, D. Burris, W. G. Sawyer, C. G. Toney, R. W. Siegel, and L. S. Schadler, "Tribological investigation of the effects of particle size , loading and crystallinity on poly (ethylene) terephthalate nanocomposites," WEAR, vol. 264, pp. 632–637, 2008, doi: 10.1016/j.wear.2007.05.009.

[58] T. Hussain, "Cold Spraying of Titanium: A Review of Bonding Mechanisms, Microstructure and Properties," Key Eng. Mater., vol. 533, pp. 53–90, 2012, doi: 10.4028/www.scientific.net/kem.533.53.

[59] P. Richer, B. Jodoin, L. Ajdelsztajn, and E. J. Lavernia, "Substrate roughness and thickness effects on cold spray nanocrystalline Al-Mg coatings," J. Therm. Spray Technol., vol. 15, no. 2, pp. 246–254, 2006, doi: 10.1361/105996306X108174.

[60] M. Fukumoto et al., "Effect of substrate temperature on deposition behavior of copper particles on substrate surfaces in the cold spray process," J. Therm. Spray Technol., vol. 16, no. 5–6, pp. 643–650, 2007, doi: 10.1007/s11666-007-9121-9.

[61] J. G. Legoux, E. Irissou, and C. Moreau, "Effect of substrate temperature on the formation mechanism of cold-sprayed aluminum, zinc and tin coatings," J. Therm. Spray Technol., vol. 16, no. 5–6, pp. 619–626, 2007, doi: 10.1007/s11666-007-9091-y.

[62] Y. Watanabe, C. Yoshida, K. Atsumi, M. Yamada, and M. Fukumoto, "Influence of Substrate Temperature on Adhesion Strength of Cold-Sprayed Coatings," J. Therm. Spray Technol., vol. 24, no. 1–2, pp. 86–91, 2014, doi: 10.1007/s11666-014-0165-3.

[63] Y. Xu and I. M. Hutchings, "Cold spray deposition of thermoplastic powder," Surf. Coatings Technol., vol. 201, no. 6, pp. 3044–3050, 2006, doi: 10.1016/j.surfcoat.2006.06.016.

[64] G. Benenati and R. Lupoi, "Development of a Deposition Strategy in Cold Spray for Additive Manufacturing to Minimize Residual Stresses," Procedia CIRP, vol. 55, pp. 101–108, 2016, doi: 10.1016/j.procir.2016.08.042.

[65] A. S. Alhulaifi, G. A. Buck, and W. J. Arbegast, "Numerical and experimental investigation of cold spray gas dynamic effects for polymer coating," J. Therm. Spray Technol., vol. 21, no. 5, pp. 852–862, 2012, doi: 10.1007/s11666-012-9743-4.

[66] Z. Wang, S. Cai, W. Chen, R. A. Ali, and K. Jin, "Analysis of Critical Velocity of Cold Spray Based on Machine Learning Method with Feature Selection," J. Therm. Spray Technol., vol. 30, no. 5, pp. 1213–1225, 2021, doi: 10.1007/s11666-021-01198-8.

[67] H. Assadi, F. Gärtner, T. Stoltenhoff, and H. Kreye, “Bonding mechanism in cold gas spraying,” Acta Mater., vol. 51, no. 15, pp. 4379–4394, 2003, doi: 10.1016/S1359-6454(03)00274-X.

[68] F. Raletz, M. Vardelle, and G. Ezo’o, “Critical particle velocity under cold spray conditions,” Surf. Coatings Technol., vol. 201, no. 5, pp. 1942–1947, 2006, doi: 10.1016/j.surfcoat.2006.04.061.

[69] N. K. Singh, K. Z. Uddin, J. Muthulingam, R. Jha, and B. Koohbor, “Analyzing the Effects of Particle Diameter in Cold Spraying of Thermoplastic Polymers,” J. Therm. Spray Technol., vol. 30, no. 5, pp. 1226–1238, 2021, doi: 10.1007/s11666-021-01219-6.

[70] J. Lee, S. Shin, H. J. Kim, and C. Lee, “Effect of gas temperature on critical velocity and deposition characteristics in kinetic spraying,” Appl. Surf. Sci., vol. 253, no. 7, pp. 3512–3520, 2007, doi: 10.1016/j.apsusc.2006.07.061.

[71] C. A. Bernard, H. Takana, O. Lame, K. Ogawa, and J. Y. Cavaillé, “Influence of the Nozzle Inner Geometry on the Particle History During Cold Spray Process,” J. Therm. Spray Technol., 2022, doi: 10.1007/s11666-022-01407-y.

[72] A. G. C. C. Americas, “Adhesive Fluoro-polymers.” 2020.

[73] Emerson, “PTFE and PFA Similarities and Differences,” pp. 1–5, 2017.

[74] D. Tiab and E. C. Donaldson, “Wettability,” in Petrophysics, 3rd ed., 2012, pp. 375–418.

[75] A. Work and Y. Lian, “A critical review of the measurement of ice adhesion to solid substrates,” Prog. Aerosp. Sci., vol. 98, no. March, pp. 1–26, 2018, doi: 10.1016/j.paerosci.2018.03.001.

[76] C. Laforte and A. Beisswenger, “Icephobic Materials Centrifuge Adhesion Test,” no. January 2005, 2018.

[77] M. Bleszynski and E. Clark, “Current Ice Adhesion Testing Methods and the Need for a Standard : A Concise Review,” pp. 117–133, 2021.

[78] S. Yin, M. Meyer, W. Li, H. Liao, and R. Lupoi, “Gas Flow, Particle Acceleration, and Heat Transfer in Cold Spray: A review,” J. Therm. Spray Technol., vol. 25, no. 5, pp. 874–896, 2016, doi: 10.1007/s11666-016-0406-8.

[79] A. Nastic, B. Jodoin, D. Poirier, and J. G. Legoux, “Particle temperature effect in cold spray: A study of soft particle deposition on hard substrate,” Surf. Coatings Technol., vol. 406, no. December 2020, 2021, doi: 10.1016/j.surfcoat.2020.126735.

[80] A. Nastic, “Cold Gas Dynamic Spray Impact : Metallic Bonding Pre- Requisites and Experimental Particle In-Flight Temperature Measurements,” 2021.

[81] J. E. Castillo, Y. Huang, Z. Pan, and J. A. Weibel, “Asymmetric solidification during droplet freezing in the presence of a neighboring droplet,” Int. J. Heat Mass

Transf., vol. 171, p. 121134, Jun. 2021, doi: 10.1016/J.IJHEATMASSTRANSFER.2021.121134.

[82] J. Gong, J. Hou, L. Yang, W. Wu, G. Li, and T. Gao, "Mesoscopic investigation of frost crystal nucleation on cold surface based on the lattice-Boltzmann method †," J. Mech. Sci. Technol., vol. 33, no. 4, pp. 1925–1935, 2019, doi: 10.1007/s12206-019-0343-9.

[83] J. Blake, D. Thompson, D. Raps, and T. Strobl, "Simulating the freezing of supercooled water droplets impacting a cooled substrate," AIAA J., vol. 53, no. 7, pp. 1725–1739, Mar. 2015, doi: 10.2514/1.J053391/ASSET/IMAGES/LARGE/FIGURE14.JPEG.

[84] X. Zhang, X. Liu, X. Wu, and J. Min, "Simulation and experiment on supercooled sessile water droplet freezing with special attention to supercooling and volume expansion effects," Int. J. Heat Mass Transf., vol. 127, pp. 975–985, Dec. 2018, doi: 10.1016/J.IJHEATMASSTRANSFER.2018.07.021.

[85] D. MacDonald, R. Fernández, F. Delloro, and B. Jodoin, "Cold Spraying of Armstrong Process Titanium Powder for Additive Manufacturing," J. Therm. Spray Technol., vol. 26, no. 4, pp. 598–609, 2017, doi: 10.1007/s11666-016-0489-2.

[86] W. Wong, P. Vo, E. Irissou, A. N. Ryabinin, J. G. Legoux, and S. Yue, "Effect of particle morphology and size distribution on cold-sprayed pure titanium coatings," J. Therm. Spray Technol., vol. 22, no. 7, pp. 1140–1153, 2013, doi: 10.1007/s11666-013-9951-6.

[87] V. N. V. Munagala, V. Akinyi, P. Vo, and R. R. Chromik, "Influence of Powder Morphology and Microstructure on the Cold Spray and Mechanical Properties of Ti6Al4V Coatings," J. Therm. Spray Technol., vol. 27, no. 5, pp. 827–842, 2018, doi: 10.1007/s11666-018-0729-8.

[88] D. Barletta and M. Poletto, "Aggregation phenomena in fluidization of cohesive powders assisted by mechanical vibrations," Powder Technol., vol. 225, pp. 93–100, 2012, doi: 10.1016/j.powtec.2012.03.038.

[89] B. Jodoin, "Cold spray nozzle mach number limitation," J. Therm. Spray Technol., vol. 11, no. 4, pp. 496–507, 2002, doi: 10.1361/105996302770348628.

[90] H. Memon, D. S. A. De Focatiis, K. S. Choi, and X. Hou, "Durability enhancement of low ice adhesion polymeric coatings," Prog. Org. Coatings, vol. 151, no. July 2020, p. 106033, 2021, doi: 10.1016/j.porgcoat.2020.106033.

[91] K. Ogawa, Cold spray coatings, vol. 60, no. 5. 2017.

[92] J. Guancheng, "Evaluation Methods and Influencing Factors of Gas Wettability," in Gas Wettability of Reservoir Rock Surfaces with Porous Media, 2018, pp. 29–84.

[93] W. Tang et al., “Dynamic changes of hydrophobic behavior during icing,” Surf. Coatings Technol., vol. 397, no. June, p. 126043, 2020, doi: 10.1016/j.surfcoat.2020.126043.

[94] P. Irajizad, S. Nazi, and H. Ghasemi, “Icephobic surfaces: Definition and figures of merit,” Adv. Colloid Intyerface Sci., vol. 269, pp. 203–218, 2019, doi: 10.1016/j.cis.2019.04.005.

[95] J. Hou, J. Gong, X. Wu, and Q. Huang, “Numerical study on impacting-freezing process of the droplet on a lateral moving cold superhydrophobic surface,” Int. J. Heat Mass Transf., vol. 183, p. 122044, Feb. 2022, doi: 10.1016/J.IJHEATMASSTRANSFER.2021.122044.

[96] M. Song, C. Dang, T. Higashi, and E. Hihara, “Review of experimental data associated with the solidification characteristics of water droplets on a cold plate surface at the early frosting stage,” Energy Build., vol. 223, p. 110103, Sep. 2020, doi: 10.1016/J.ENBUILD.2020.110103.

[97] S. Dash, J. de Ruiter, and K. K. Varanasi, “Photothermal trap utilizing solar illumination for ice mitigation,” Sci. Adv., vol. 4, no. 8, Aug. 2018, doi: 10.1126/SCIADV.AAT0127/SUPPL_FILE/AAT0127_SM.PDF.

[98] L. Oberli, D. Caruso, C. Hall, M. Fabretto, P. J. Murphy, and D. Evans, “Condensation and freezing of droplets on superhydrophobic surfaces,” Adv. Colloid Interface Sci., vol. 210, pp. 47–57, Aug. 2014, doi: 10.1016/J.CIS.2013.10.018.

[99] M. Schremb and C. Tropea, “Solidification of supercooled water in the vicinity of a solid wall,” Phys. Rev. E, vol. 94, p. 52804, 2016, doi: 10.1103/PhysRevE.94.052804.

[100] H. Memon, J. Liu, D. S. A. De Focatiis, K. so Choi, and X. Hou, “Intrinsic dependence of ice adhesion strength on surface roughness,” Surf. Coatings Technol., vol. 385, p. 125382, 2020, doi: 10.1016/j.surfcoat.2020.125382.

[101] H. Sojoudi, M. Wang, N. D. Boscher, G. H. McKinley, and K. K. Gleason, “Durable and scalable icephobic surfaces: Similarities and distinctions from superhydrophobic surfaces,” Soft Matter, vol. 12, no. 7, pp. 1938–1963, 2016, doi: 10.1039/c5sm02295a.

5.2 Metallic Solution

The second icephobic solution investigates the deposition window of aluminum-rich QCs. Optimal spraying conditions were assessed by varying process parameters in a matrix to explore the complete range of low-pressure CS. To overcome QC brittleness, the brittle-to-ductile transition was explored for this QC feedstock by using powder pre-heating. Two pre-heating temperatures, above the documented QC's ductile-to-brittle transition, were examined to achieve ductile particle deformations. Having exhausted all possible avenues of plastically deforming the QC particles with low-pressure CS, retainment of the QC particles was attempted by introducing a more ductile phase and creating a cermet coating. The softer phase acting as a matrix in cermet coatings was added in two specific ratios and the deposited coatings were then studied to observe the retained content of the QC phase. The work performed is the first step in determining the deposition window/strategy of QCs using low-pressure CS, leading to the future development of icephobic coatings.

5.2.1 Parameter Matrix

As a first step in studying the CS deposition of QC materials, a matrix of spraying conditions, as shown in Table 3, was used to explore the full range of the low-pressure cold spray system. The stagnation temperatures and pressures were varied from 690 to 3450 kPa, and 100 to 500 ℃.

Table 3. Spray parameter matrix for QC feedstock

Spray #	Stagnation pressure (kPa)	Stagnation temperature (℃)
1	690	100
2		250
3		500
4	1725	100
5		250
6		500
7	3450	100
8		250
9		500

A total of nine different temperature-pressure combinations were tested using the same traverse speed, powder feeding settings, standoff distance, and number of passes. Details

on the spraying conditions that remained constant during matrix testing are found in Table 4.

Table 4. Constant spray parameters for QC feedstock

Parameter name	Setting
Traverse speed	10 mm/s
Standoff distance	10 mm
Powder feeding wheel size	Medium wheel
Powder feeding wheel angular speed	2 rpm
Powder feeding gas flow rate	12.5 SCFH
Number of passes	1

Nitrogen was used as the propellant gas as it is more economical than alternatives like helium and can be sustainably produced, which is especially important for future large-scale applications. The QC feedstock was propelled onto both aluminum 6061-T6 and stainless-steel 304 substrates, to observe the deposition behavior on hard and soft substrates. No surface preparation methods were used in this work so that particle impact behavior could be isolated and not confused with impacts sustained in a grit blasting treatment.

Among the nine spraying conditions, no visible deposition occurred on any of the substrates. However, embedment of particles could be seen in both the aluminum and stainless-steel substrates in the last parameter combination, namely at 500 ℃ and 3450 kPa. Shown in Figure 71, embedment is observed in both substrate materials, with increased amounts of particles in the aluminum substrate. Aluminum's lower hardness and larger ductility facilitated particle embedment more readily than with the stainless steel. Despite this, all particles seen within the substrates seem to have fragmented into smaller pieces. As shown in Figure 36, QC particles have a spherical morphology in their as-received state. Therefore, based on the cross-sections seen in Figure 71, this confirms that the particles fractured upon impact and only a fraction of the particles embedded in the surface. Examining the stainless-steel substrate in Figure 71 (2b), a full QC particle appears to have

been retained after deposition. However, the particle displays fracturing in multiple locations, demonstrating the brittleness of QC materials.

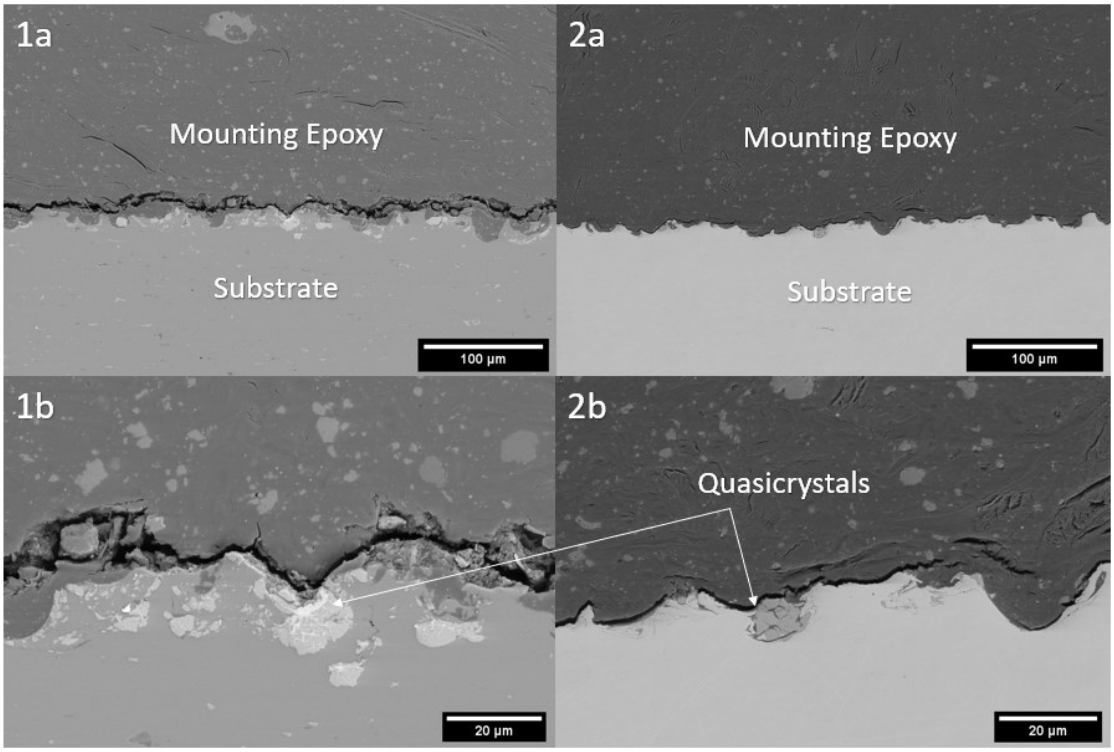

Figure 71. Deposition of room-temperature QC feedstock at 500 °C and 3450 kPa on aluminum (1) and stainless-steel (2) substrates at 250X (a) and 1000X (b) magnification

In CS, it is well known that metallic particles must undergo enough plastic deformation to form metallurgical bonding with the substrate [96], [97]. Obtaining the required plastic deformation is accomplished by reaching what is called the particle critical velocity, which varies by feedstock material and substrate combination [97]. If the particle velocity remains below its critical value, particles will rebound from the substrate leaving behind craters [98]. A similar effect can occur when particles exceed a second, and higher, critical velocity. When particles exceed the second critical velocity they are no longer within what is considered to be the deposition window where bonding will typically occur, and rather severe erosion of the substrate will occur [98]. Nevertheless, since the feedstock material in this work behaves more like a ceramic, the concept of particle critical velocity is not as indicative in the same way it is for metallic feedstock. For this reason, the observed substrate erosion and absence of continuous particle embedment is believed to be the result

of a lack of particle ductility. As the fractured QC particle displays in Figure 71 (2b), overall embedment could not be achieved because particles are too brittle to effectively penetrate into the substrate in a continuous fashion preventing the formation of a complete single layer of QC particles. Then again, it is possible that the substrate also lacks ductility, creating a second barrier for particles to successfully be embedded. Obtaining a softer substrate, potentially through substrate pre-heating, could prevent the brittle failure of particles like QCs and result in the embedment of a first layer of particles. In addition, for a surface phenomenon like icephobicity, a single layer of particles would be sufficient.

5.2.2 Powder Pre-Heating

To overcome the lack of particle ductility and increase the probability of particle embedment, powder pre-heating was used. Despite the processing gas reaching a temperature of 500 ℃ in the final parameter combination, the feedstock material appeared to experience insufficient thermal softening for deposition to occur. Increasing the ductility of very hard materials, such as QCs, by using their brittle-to-ductile transition temperature could serve as a potential solution to plastically deforming particles. The reported brittle-to-ductile transition temperature for QC materials is estimated to be above 600 ℃ [82]. However, reaching a particle temperature above 600 ℃ is not possible with a low-pressure CS system that can only attain stagnation gas temperatures of 500 ℃. In fact, injected particles are not even exposed to temperatures near the stagnation conditions since they are injected after the nozzle throat, where the gas flow is much colder. As such, to attempt thermal softening, pre-heating must be used to increase the particle temperature prior to entering the main gas flow. Powder pre-heating is commonly used in CS to reduce the particle critical velocity by increasing particle temperature [99], [100]. Although, as previously stated, the particle critical velocity is not as relevant for QC feedstock since it does not behave in the same way as other metals, therefore powder pre-heating is being used as a means of overcoming brittleness by increasing ductility.

Two targeted pre-heating temperatures were used in this work. The first temperature is 600 ℃, which is the reported brittle-to-ductile transition temperature for QC materials. The second pre-heating temperature, 700 ℃, is a result of exploring the highest possible temperature provided by the particle pre-heater. Shown in Table 5, and using the equations

provided in section 4.2.2, temperatures and mass flow rates are provided for the gas heater, the feedstock and the resulting pre-heated feedstock.

Table 5. Powder pre-heating temperatures (T) in [℃], and feed rate (FR) in standard cubic feet per hour [SCFH]

	Gas heater		Feedstock Carrier Gas		Pre-heated Feedstock
Spray #	T	FR	T	FR	T
1	800	53	15	15	600
2	900	53	15	12.5	700

Process parameters that remained constant for both pre-heating spray conditions are found in Table 6.

Table 6. Constant spray parameters for pre-heated QC feedstock

Parameter name	Setting
Stagnation Temperature	500 ℃
Stagnation Pressure	3450 kPa
Traverse speed	10 mm/s
Standoff distance	10 mm
Powder feeding wheel size	Medium wheel
Powder feeding wheel angular speed	2 rpm
Number of passes	1

To maintain a high particle velocity for particle embedment, processing parameters of 500 ℃ and 3450 kPa were used in conjunction with powder pre-heating. Much like the room temperature deposition, aluminum and stainless-steel substrates were used to explore substrate ductility, and no surface treatments were used to isolate particle deformation behaviors. Cross-sectional views of substrates with embedded particles, for both pre-heating temperatures, are shown in Figure 72. A very similar behavior as the room-temperature deposition can be observed. Overall, no coating was formed, however there appears to be more embedment than was previously observed without powder pre-heating.

In Figure 72 (1a), for the aluminum substrate and at a pre-heating temperature of 600 ℃, particle cohesion can be observed between two particles. It appears that a QC particle initially embedded into the aluminum substrate and fractured in the process, as can be seen with the radiating fracture lines on the left side of the particle. Subsequently, a second particle seems to have deposited on top of the first one, which is not a behavior that was previously observed without powder pre-heating. Retaining the second particle on top of the first one indicates that potential metallurgical bonds were formed between the two particles. Although an entire coating was not formed, particle cohesion could indicate that particles are beginning to thermally soften and that deposition beyond the first layer could be possible when pre-heating is used. When increasing the powder pre-heating temperature with the same substrate material, shown in Figure 72 (1b), particle deposition does not appear to have improved. This indicates that an increase of 100 ℃ in pre-heating temperature is of minimal significance on particle impact temperature, due to the forced convection experienced by particles in the main gas flow.

For pre-heated particles deposited on stainless-steel substrates, a completely different deformation behavior can be observed than with room temperature feedstock. Shown in Figure 72 (2a and 2b), pre-heated QC particle have deformed and flattened on the substrate surface. Unlike the fractured QC particle that had embedded in the substrate when powder pre-heating was not used, pre-heated QC particles do not show any visible cracking. This suggests that particles impacting the stainless-steel substrate have effectively been softened during the deposition process, however particle cohesion and deposition past a first layer remains unobserved.

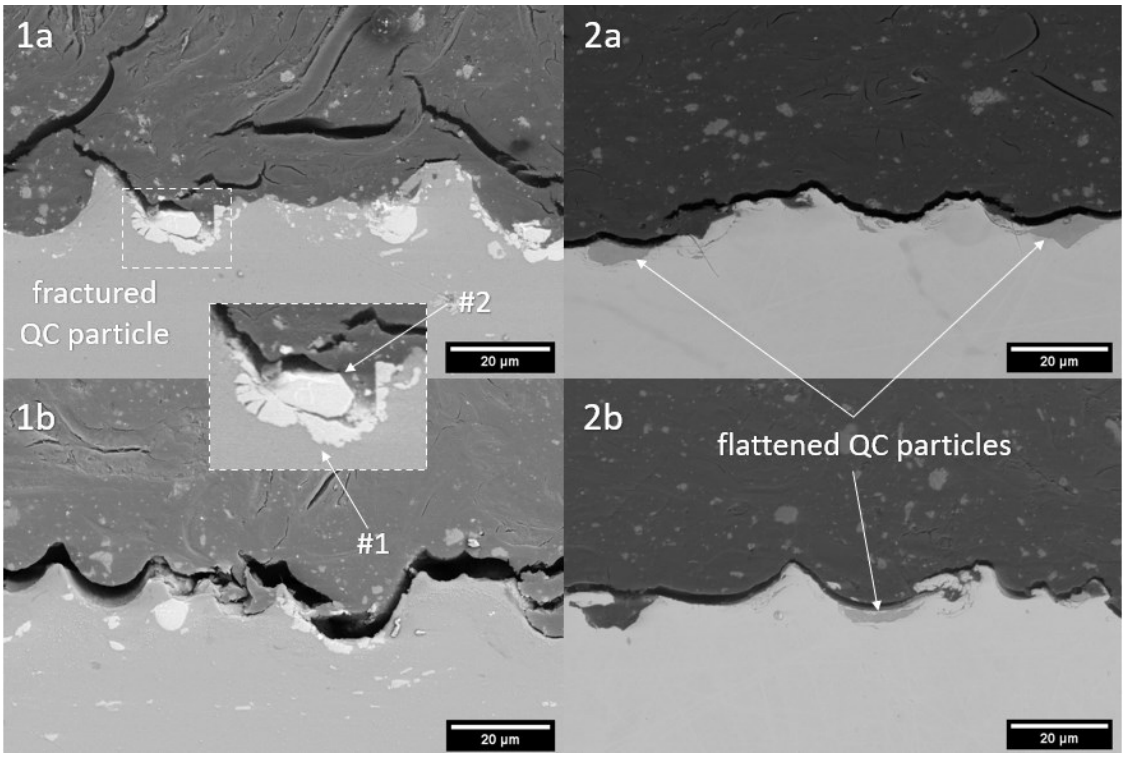

Figure 72. Cross-sectional view of deposited QC feedstock at 500 °C and 3450 kPa on aluminum (1) and stainless-steel (2) substrates, with feedstock preheated to 600 °C (a) and 700 °C (b)

Figure 73 displays the surface of an aluminum substrate after the deposition of pre-heated QC particles. Macroscopically, the surface of the aluminum substrate appears to have QC particles embedded on its surface. However, at the microscopic level, the texturing observed on the substrate's surface is the product of craters left behind by impacting particles. Visual indentations can be seen throughout the full length of the path travelled by the CS nozzle resulting in a severely eroded substrate. A similar behavior has been observed in a study looking at the effect of ceramic content in the deposition of cermet coatings [101]. Their work showed that when the feedstock content was entirely made of ceramic material, much like the QC feedstock used in this work, extensive substrate erosion in the form of craters was observed. Despite minor amounts of particles embedding into the substrate, as shown previously, the bulk of the feedstock material impacting the substrate resulted in erosion.

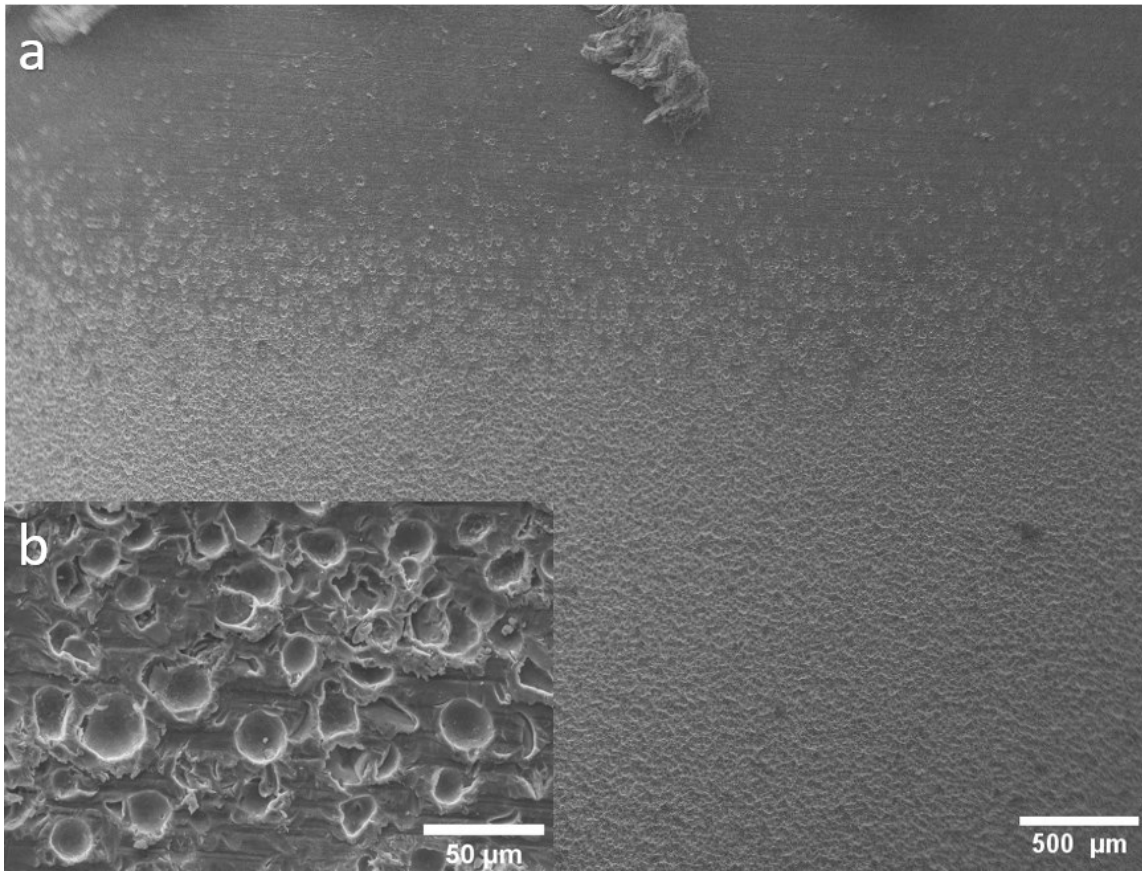

Figure 73. Aluminum substrate top view (a) edge of spray path, (b) magnified view of multiple craters

A magnified view of a single pre-heated QC particle impact on a stainless-steel substrate is shown in Figure 74. Severe substrate deformation can be observed as material jetting on the edges of the crater. Despite the substrate being made of a high strength stainless-steel, this level of plastic deformation further demonstrates the high hardness of the QC feedstock. Based on what is observed in Figure 73 and Figure 74, two possible solutions could be used to produce a functional QC coating, with powder pre-heating. If embedding of QC particles is desired, it is hypothesized that reducing the kinetic energy of particles could result in less rebounding energy, thus retaining particles in the substrate. Therefore, lower processing parameters such as gas pressure or temperature should be used to decrease particle velocity. However, if plastic deformation of particles on the substrate is desired, as is typically observed in metallic cold spray deposition, a higher particle velocity and increased thermal softening would be required. Obtaining a more ductile particle at impact, in addition to a higher particle velocity, could potentially recreate a similar deformation

that is observed with other metallic feedstock materials resulting in bonding to the substrate.

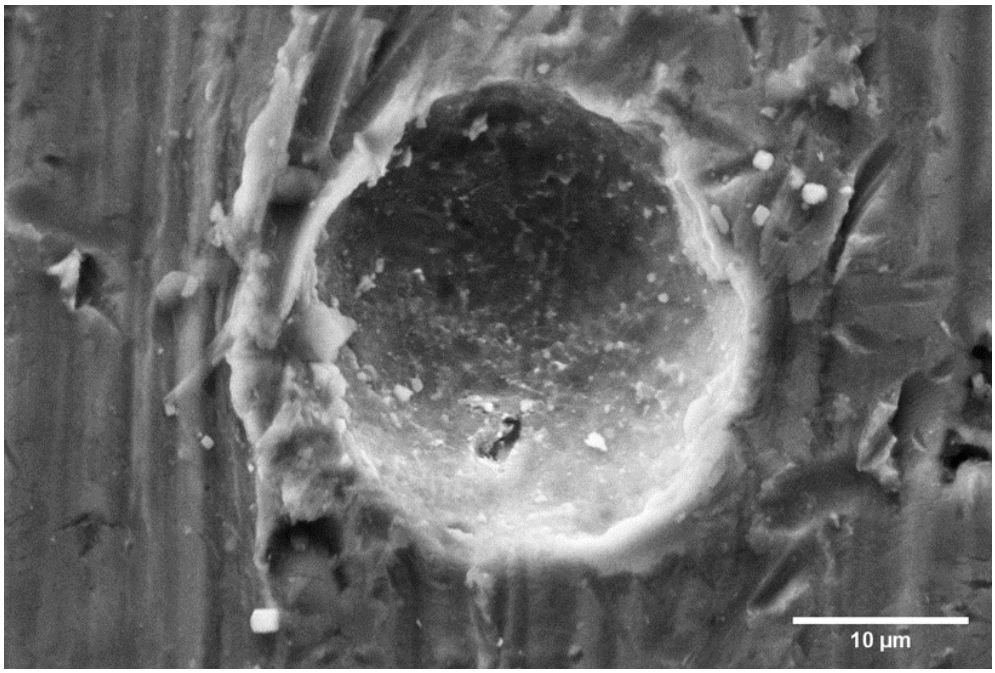

Figure 74. Overview of single particle indentation, showing jetting of the stainless-steel substrate

5.2.3 Cermet Deposition

Depositing hard and brittle materials, such as QCs, has proven to be quite challenging, even with substantial powder preheating. Despite this, many studies have shown that to deposit ceramic-like materials, like QCs, introducing a second more ductile material into the feedstock could help retain the ceramic particles in the final coating [101]–[104]. The combination of ceramics and ductile metals in the same feedstock leads to the creation of a composite ceramic-metal coating (cermets). In cermets, the ceramic material interacts with the ductile metallic phase to increase deposition through impingement leading to coatings with high ceramic wt.% [101]. Once both materials are deposited, only a fraction of the ceramic material is retained in the final composite coating, however this fraction can vary depending on the ceramic content's initial wt.%, powder morphologies and the specific feedstock material combination [101]. Cermet coatings are known for preserving the best properties of both materials leading to increased overall hardness and wear

resistance, from the ceramic phase, while also remaining ductile because of the metallic phase.

While studies have been conducted on determining the optimal feedstock ceramic-metal composition, this study's goal is to retain as much of the QC particles while minimizing how much aluminum is in the final coating. For icephobic applications, it is imperative not to alter the desired surface chemistry of the QC phase, especially when dealing with a surface phenomenon such as ice accretion [101]. As a result, QC content was kept high with two proportions of 90 wt.% QC and 75 wt.% QC. The spray parameters used in the deposition of cermet QC-Al feedstock are shown in Table 7.

Table 7. Spray parameters for cermet QC-Al feedstock

Parameter name	Setting
Stagnation temperature	250 ℃
Stagnation pressure	1725 kPa
Traverse speed	10 mm/s
Standoff distance	10 mm
Powder feeding wheel size	Medium wheel, 240 holes
Powder feeding wheel angular speed	2 rpm
Number of passes	10

The stagnation conditions for pressure and temperature were selected based on parameters typically used in the deposition of aluminum feedstock. With the presence of aluminum in the feedstock, higher parameters previously used with QCs would result in the melting of the aluminum phase and/or potentially clogging of the CS nozzle. Aluminum substrates were selected to avoid any issues related to dissimilar material deposition and because the deposition behavior of aluminum on aluminum is well established in the field.

Figure 75 presents the cross-sections of both cermet coatings deposited with feedstock compositions of 90 wt.% and 75 wt.% QC. The aluminum substrate and aluminum feedstock are represented by the light grey phase, as they are made of identical

compositions, and the QC particles are shown by the white phase. Based on the literature, the optimal deposition ratio for a cermet coating is typically around 30 wt.% ceramic phase, with a decrease in overall deposition when this ratio is increased [105]–[107]. This correlates with the approximate thicknesses obtained in these tests. A thickness of 45 μm was obtained for a feedstock of 90 wt.% QC, and 225 μm was obtained when the feedstock was 75 wt.% QC. Although coating thickness is not a direct indicator of process efficiency, it does suggest that decreasing the content of the QC phase resulted more material being deposited with identical processing conditions.

Coating cross-sections, shown in Figure 75, present a fully dense composition without any visible pores or microcracking around the QC particles. In addition, both coatings demonstrate excellent conformity at the substrate interface, suggesting a good coating adhesion. Despite this, the performance of a cermet coating lies in the ceramic composition of the deposited coating. A coating with low ceramic content will not take full advantage of the ceramic phase, leading mechanical properties being largely influenced by the matrix material. To obtain the ceramic content in deposited coatings, contrast analysis of the coating cross-sectional images was used. This analysis revealed that the coatings produced with a feedstock of 90 wt.% QC have a resulting composition of 12.5 wt.% QC, and coatings produced with a feedstock composition of 75 wt.% QC have a final composition of 9 wt.% QC. Based on these values, both coating cross-sections revealed an average QC retention of 13% of their initial feedstock QC composition. This value is substantially lower than what is reported in the literature for other cermet coatings which normally averages around 50% [105]–[107]. As a result, it is expected that these coatings' icephobic behaviors would not be improved if they were to be compared with a bulk aluminum surface.

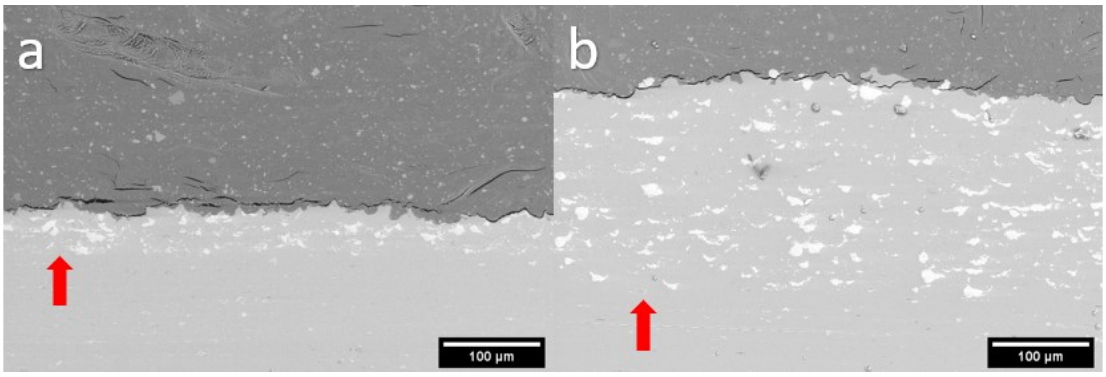

Figure 75. Cross-sectional view of QC-Al cermet coatings with (a) 90 wt.% QC and (b) 75 wt.% QC (red arrow represents substrate-coating interface)

The deposition of cermet coatings has been shown to be influenced by the particle morphology of the feedstock being used [102], [104]. In a study observing the effect of ceramic powder morphology in the production of aluminum-alumina cermet coatings, angular alumina resulted in better deposition than spherical alumina [104]. While testing four different ceramic content proportions, excluding 0 and 100 wt.% of the ceramic phase, the angular ceramic powder consistently outperformed the spherical one. As a result, it is hypothesized that, in addition to decreasing the feedstock's initial ceramic content, using a different QC feedstock morphology could improve the retention of the ceramic phase in deposited coating.

6 CONCLUSIONS AND FUTURE WORK

6.1 Conclusions

The purpose of this research was to explore the manufacturing of two icephobic coating solutions, polymer and metallic, using cold spray and to characterize their icephobic performance. The deposition of both icephobic materials was achieved through specific research objectives, tailored cold spraying solutions based on individual feedstock compositions, and careful analysis of deposited coating properties.

The icephobic polymer solution focused on improving the cold spray deposition of polymer feedstock onto metallic substrates as commercial cold spraying nozzles revealed issues with coating adhesion, porosity levels, and overall deposition. To mitigate these issues, a new nozzle was designed to decrease the particle critical velocity by increasing particle temperature, while also using the same processing parameters. Using CFD analysis, the new nozzle design revealed a higher particle temperature and a higher particle velocity than the commercial nozzle. Experimentally obtained results show that the new nozzle design produces a higher quality coating with thicker deposits and minimal porosity, suggesting that particles reached their critical velocity at impact.

The icephobic performance of the polymer solution was assessed through three different experiments characterizing all aspects of the icing process: 1) hydrophobicity at room temperature, 2) ice nucleation/growth behavior in a cold environment, and 3) ice adhesion properties. At room temperature, the as-sprayed coating demonstrated a superhydrophobic behavior with a static contact angle exceeding 150°, caused by its unique surface features and chemical properties. When exposed to freezing temperatures, the as-sprayed coating revealed its vulnerability to frost formation. The coating's complex surface structure promoted frost formation and subsequent growth, leading single water droplets to have decreased static contact angles and reduced ice growth times. Despite the challenge related to frost formation, modelling of the freezing water droplets showed that it is imperative to achieve a high static contact angle to decrease the solidification time. The final stage of the icing process: ice removal, was executed through macro and micro sized ice adhesion tests. The polymer solution outperformed all reference materials in the macro ice adhesion test through low ice adhesion. However, due to the formation of an artificial Cassie wetting

state, the macro ice adhesion results are not an accurate depiction of real-world applications. For a better representation of ice adhesion performance, micro ice adhesion tests of single droplets were performed. The polymer solution demonstrated that the same frosting effects which impacted droplet solidification created lasting consequences for the micro ice adhesion of single droplets. The increased surface area at the icing interface, due to low static contact angles and the infiltration of water into the coating's surface asperities, created a Wenzel wetting state and led to more realistic ice adhesion data. Through all atmospheric icing tests, the polymer solution demonstrated that its icephobicity is heavily influenced by the development of frost and that its use as an anti-icing coating could be compromised in highly humid environments.

The second icephobic solution, i.e., metallic solution, focused on a single objective to deposit very brittle QC particles onto a metallic substrate using cold spray. Aluminum and stainless-steel substrates were used to observe the effect of substrate hardness and ductility on the deformation and embedment of QC particles. As a first step, a matrix of processing parameters was used to explore the full range of the cold spray system. Results show that when maximum pressure and temperature conditions are used, QC particle embedment can be observed in sample cross-sections. However, for both substrate materials, brittleness of the feedstock material appears to have prevented the deposition of a complete first layer. To mitigate the brittleness of QC particles and promote a ductile particle deformation, powder pre-heating was used before injecting the feedstock into the main gas flow. Pre-heating the feedstock above the documented brittle-to-ductile transition temperature of QCs showed signs of improved particle ductility in sample cross-sections, however no first layer deposition was observed. Results of the aluminum substrate show signs of particles cohesively bonding, however particle brittleness continued to prevail through fracturing. In the stainless-steel substrate, particles deformed without any visible fractures suggesting particles were thermally softened at impact because of the powder pre-heating treatment. The ductile deformation of the QC particles on stainless-steel suggest that powder pre-heating is a step in the right direction, despite the lack of a first layer deposition. An attempt to retain QC particles in a coating was then done through the addition of a softer phase, acting as a matrix, into the feedstock material for the deposition of a cermet coating. Two QC composition ratios of 90 wt.% and 75 wt.% were deposited with aluminum selected as

the matrix material. Obtained results show that approximately 13% of the QC feedstock is retained in deposited coating, resulting in a coating that is primarily composed of the aluminum matrix material. Therefore, these coatings would likely not demonstrate any icephobic properties due to the low QC content.

6.2 Future Work

The results presented in this work provide added knowledge in the field of icephobic coating development using cold spray, however many future studies could be conducted to render these solutions commercially viable. Potential future studies and investigations are listed below.

1. For the application of cold sprayed polymer coatings in industrial settings, improved coating adhesion characteristics should be studied to remove the need for substrate pre-heating. This could allow the application of coatings to large scale surfaces, many of which are subject to atmospheric icing.
2. To improve the accuracy of icephobic testing and to examine all potential real-world conditions, icing wind tunnel testing should be carried out. The use of impacting supercooled water droplets would provide the most realistic icing conditions in a laboratory environment.
3. Due to the degrading icephobic performance of the polymer solution in humid environments, caused by its unique surface roughness and texture, a study should be conducted on how this solution would perform if a polishing process were used to create a smoother surface. This could provide added insight into the viability of this specific polymer material for any future cold sprayed icephobic surface studies.
4. Any future studies requiring the centrifuge adhesion test equipment used in this work should re-evaluate the ice making process and how ice is formed on test surfaces, to avoid the formation of an artificial Cassie state. In addition, since air bubbles caused the Cassie state formation within surface textures, a potential solution could be to place the ice making equipment in a vacuum during the filing of trays with water. This would prevent air bubbles from being trapped at the ice/surface interface prior to the freezing process, however this would result in purely a Wenzel wetting state.

5. To increase the ductility of QC materials, much higher temperatures could be used in the powder pre-heating process. As a result, further thermal softening of the particles would potentially occur leading to ductile particle deformation and a complete first layer acting as a coating. Increasing particle ductility through powder pre-heating has shown to be the best solution to creating full QC coatings.
6. Based on past studies showing that ceramic materials can demonstrate ductile behavior at smaller sample sizes, it is hypothesized that QCs could as well. Therefore, a study could be done on the aerosol deposition of milled QC feedstock. Aerosol deposition occurs in a vacuum which would prevent a bow shock from forming over the substrate, thus allowing particle to reach higher impact velocities. Whereas, milling the QC feedstock would allow the particles to potentially deform in a more ductile manner than was seen in this work.

REFERENCES

[1] F. T. Lynch and A. Khodadoust, “Effects of ice accretions on aircraft aerodynamics,” vol. 37, no. 2001, pp. 669–767, 2002.

[2] M. Farzaneh, *Atmospheric Icing of Power Networks*, vol. 84. 2008.

[3] N. Dalili, A. Edrisy, and R. Carriveau, “A review of surface engineering issues critical to wind turbine performance,” *Renew. Sustain. Energy Rev.*, vol. 13, no. 2, pp. 428–438, 2009, doi: 10.1016/j.rser.2007.11.009.

[4] X. Huang *et al.*, “A survey of icephobic coatings and their potential use in a hybrid coating/active ice protection system for aerospace applications,” *Prog. Aerosp. Sci.*, vol. 105, no. July 2018, pp. 74–97, 2019, doi: 10.1016/j.paerosci.2019.01.002.

[5] J. T. Salisbury, “MICROWAVE DEICING AND ANTI-ICING SYSTEM FOR ARCRAFT,” 5,615,849, 1997.

[6] Z. Goraj, “AN OVERVIEW OF THE DEICING AND ANTIICING TECHNOLOGIES WITH PROSPECTS FOR THE FUTURE,” 2004, pp. 1–11.

[7] O. Parent and A. Ilinca, “Anti-icing and de-icing techniques for wind turbines : Critical review,” *Cold Reg. Sci. Technol.*, vol. 65, no. 1, pp. 88–96, 2011, doi: 10.1016/j.coldregions.2010.01.005.

[8] Y. Shen, X. Wu, J. Tao, C. Zhu, Y. Lai, and Z. Chen, “Icephobic materials: Fundamentals, performance evaluation, and applications,” *Prog. Mater. Sci.*, vol. 103, no. January 2018, pp. 509–557, 2019, doi: 10.1016/j.pmatsci.2019.03.004.

[9] R. Ramachandran, M. Kozhukhova, K. Sobolev, and M. Nosonovsky, “Anti-icing superhydrophobic surfaces: Controlling entropic molecular interactions to design novel icephobic concrete,” *Entropy*, vol. 18, no. 4, 2016, doi: 10.3390/e18040132.

[10] S. Jung, M. Dorrestijn, D. Raps, A. Das, C. M. Megaridis, and D. Poulikakos, “Are superhydrophobic surfaces best for icephobicity?,” *Langmuir*, vol. 27, no. 6, pp. 3059–3066, 2011, doi: 10.1021/la104762g.

[11] R. Pan, H. Zhang, and M. Zhong, “Triple-Scale Superhydrophobic Surface with Excellent Anti-Icing and Icephobic Performance via Ultrafast Laser Hybrid Fabrication,” *ACS Appl. Mater. Interfaces*, vol. 13, no. 1, pp. 1743–1753, 2021, doi: 10.1021/acsami.0c16259.

[12] M. A. Sarshar, C. Swarctz, S. Hunter, J. Simpson, and C. Choi, “Effects of contact angle hysteresis on ice adhesion and growth on superhydrophobic surfaces under dynamic flow conditions,” pp. 427–435, 2013, doi: 10.1007/s00396-012-2753-4.

[13] B. Wang *et al.*, “Heterogeneous ice nucleation and water uptake by field-collected atmospheric particles below 273 K,” vol. 117, pp. 1–15, 2012, doi: 10.1029/2012JD017446.

[14] F. Veronesi, G. Boveri, J. Mora, A. Corozzi, and M. Raimondo, “Icephobic

properties of anti-wetting coatings for aeronautical applications," *Surf. Coat. Technol.*, vol. 421, no. May, 2021.

[15] A. Schetnikov, V. Matiunin, and V. Chernov, "Conical shape of frozen water droplets," *Am. J. Phys.*, vol. 83, no. 1, pp. 36–38, 2015, doi: 10.1119/1.4897499.

[16] L. Makkonen, "Ice adhesion - Theory, measurements and countermeasures," *J. Adhes. Sci. Technol.*, vol. 26, no. 4–5, pp. 413–445, 2012, doi: 10.1163/016942411X574583.

[17] J. Mora, P. García, R. Muelas, and A. Agüero, "Hard quasicrystalline coatings deposited by hvof thermal spray to reduce ice accretion in aero-structures components," *Coatings*, vol. 10, no. 3, 2020, doi: 10.3390/coatings10030290.

[18] K. Golovin, S. P. R. Kobaku, D. H. Lee, E. T. DiLoreto, J. M. Mabry, and A. Tuteja, "Designing durable icephobic surfaces," *Sci. Adv.*, vol. 2, no. 3, 2016, doi: 10.1126/sciadv.1501496.

[19] M. Mohseni, Z. A. Dijvejin, and K. Golovin, "Designing scalable elastomeric anti-fouling coatings: Shear strain dissipation via interfacial cavitation," *J. Colloid Interface Sci.*, vol. 589, pp. 556–567, 2021, doi: 10.1016/j.jcis.2021.01.019.

[20] K. Maghsoudi, E. Vazirinasab, G. Momen, and R. Jafari, "Icephobicity and durability assessment of superhydrophobic surfaces: The role of surface roughness and the ice adhesion measurement technique," *J. Mater. Process. Technol.*, vol. 288, no. July 2020, p. 116883, 2021, doi: 10.1016/j.jmatprotec.2020.116883.

[21] H. Koivuluoto, C. Stenroos, M. Kylmälahti, M. Apostol, J. Kiilakoski, and P. Vuoristo, "Anti-icing Behavior of Thermally Sprayed Polymer Coatings," *J. Therm. Spray Technol.*, vol. 26, no. 1–2, pp. 150–160, 2017, doi: 10.1007/s11666-016-0501-x.

[22] R. Menini and M. Farzaneh, "Elaboration of Al2O3/PTFE icephobic coatings for protecting aluminum surfaces," *Surf. Coatings Technol.*, vol. 203, no. 14, pp. 1941–1946, 2009, doi: 10.1016/j.surfcoat.2009.01.030.

[23] R. Menini, Z. Ghalmi, and M. Farzaneh, "Highly resistant icephobic coatings on aluminum alloys," *Cold Reg. Sci. Technol.*, vol. 65, no. 1, pp. 65–69, 2011, doi: 10.1016/j.coldregions.2010.03.004.

[24] V. Donadei, H. Koivuluoto, E. Sarlin, and P. Vuoristo, "Lubricated icephobic coatings prepared by flame spraying with hybrid feedstock injection," *Surf. Coatings Technol.*, vol. 403, no. July, p. 126396, 2020, doi: 10.1016/j.surfcoat.2020.126396.

[25] S. A. Kulinich, M. Honda, A. L. Zhu, A. G. Rozhin, and X. W. Du, "The icephobic performance of alkyl-grafted aluminum surfaces," *Soft Matter*, vol. 11, no. 5, pp. 856–861, 2015, doi: 10.1039/c4sm02204a.

[26] S. Yang, Q. Xia, L. Zhu, J. Xue, Q. Wang, and Q. Chen, "Research on the icephobic properties of fluoropolymer-based materials," *Appl. Surf. Sci.*, vol. 257, no. 11, pp. 4956–4962, 2011, doi: 10.1016/j.apsusc.2011.01.003.

[27] M. Mohseni, J. Mora, P. Garc, A. Agu, and K. Golovin, "Quasicrystalline Coatings Exhibit Durable Low Interfacial Toughness with Ice," 2021, doi: 10.1021/acsami.1c08740.

[28] P. Juuti *et al.*, "Achieving a slippery, liquid-infused porous surface with anti-icing properties by direct deposition of flame synthesized aerosol nanoparticles on a thermally fragile substrate," *Appl. Phys. Lett.*, vol. 110, no. 16, 2017, doi: 10.1063/1.4981905.

[29] T. Wong *et al.*, "Bioinspired self-repairing slippery surfaces with pressure-stable omniphobicity," *Nature*, vol. 477, no. 7365, pp. 443–447, 2011, doi: 10.1038/nature10447.

[30] Y. Maly and H. Koivuluoto, "Cold Sprayed SLIPS Coatings: A pathway towards process optimization and icepho- bicity," no. May, 2020.

[31] Q. Liu, Y. Yang, M. Huang, Y. Zhou, Y. Liu, and X. Liang, "Durability of a lubricant-infused Electrospray Silicon Rubber surface as an anti-icing coating," *Appl. Surf. Sci.*, vol. 346, pp. 68–76, 2015, doi: 10.1016/j.apsusc.2015.02.051.

[32] L. Zhu, J. Xue, Y. Wang, Q. Chen, J. Ding, and Q. Wang, "Ice-phobic Coatings Based on Silicon-Oil-Infused Polydimethylsiloxane," 2013.

[33] H. A. Stone, "Ice-Phobic Surfaces That Are Wet," no. 8, pp. 6536–6540, 2012, doi: 10.1021/nn303372q.

[34] P. W. Wilson *et al.*, "Inhibition of ice nucleation by slippery liquid-infused porous surfaces (SLIPS)," *Phys. Chem. Chem. Phys.*, vol. 15, no. 2, pp. 581–585, 2013, doi: 10.1039/c2cp43586a.

[35] Y. H. Yeong, C. Wang, K. J. Wynne, and M. C. Gupta, "Oil-Infused Superhydrophobic Silicone Material for Low Ice Adhesion with Long-Term Infusion Stability," 2016, doi: 10.1021/acsami.6b11184.

[36] P. M. Winter *et al.*, *Polymer Coatings*. 2012.

[37] Y. Xu and I. M. Hutchings, "Cold spray deposition of thermoplastic powder," *Surf. Coatings Technol.*, vol. 201, no. 6, pp. 3044–3050, 2006, doi: 10.1016/j.surfcoat.2006.06.016.

[38] W. Lock, S. Kesavan, C. Bernard, Y. Ichikawa, and K. Ogawa, "Deposition Mechanism Analysis of Cold-Sprayed Fluoropolymer Coatings and Its Wettability Evaluation," *J. Therm. Spray Technol.*, vol. 29, no. 7, pp. 1643–1659, 2020, doi: 10.1007/s11666-020-01059-w.

[39] K. Ravi, Y. Ichikawa, T. Deplancke, K. Ogawa, O. Lame, and J. Y. Cavaille, "Development of Ultra-High Molecular Weight Polyethylene (UHMWPE) Coating by Cold Spray Technique," *J. Therm. Spray Technol.*, vol. 24, no. 6, pp. 1015–1025, 2015, doi: 10.1007/s11666-015-0276-5.

[40] K. Ravi, W. L. Sulen, C. Bernard, Y. Ichikawa, and K. Ogawa, "Fabrication of micro-/nano-structured super-hydrophobic fluorinated polymer coatings by cold-

spray," *Surf. Coatings Technol.*, vol. 373, no. February, pp. 17–24, 2019, doi: 10.1016/j.surfcoat.2019.05.078.

[41] A. S. Alhulaifi, G. A. Buck, and W. J. Arbegast, "Numerical and experimental investigation of cold spray gas dynamic effects for polymer coating," *J. Therm. Spray Technol.*, vol. 21, no. 5, pp. 852–862, 2012, doi: 10.1007/s11666-012-9743-4.

[42] K. Golovin, A. Dhyani, M. D. Thouless, and A. Tuteja, "Low Interfacial Toughness Materials for Effective Large - Scale De - Icing," no. 1, pp. 1–15.

[43] W. Wolf *et al.*, "Wear and Corrosion Performance of Al-Cu-Fe- (Cr) Quasicrystalline Coatings Produced by HVOF," *J. Therm. Spray Technol.*, vol. 29, no. 5, pp. 1195–1207, 2020, doi: 10.1007/s11666-020-01053-2.

[44] H. Parsamehr, T. Chen, D. Wang, M. Leu, I. Han, and Z. Xi, "Thermal spray coating of Al-Cu-Fe quasicrystals : dynamic observations and surface properties," no. Lc.

[45] B. Alessandro *et al.*, "Self-lubricating, low friction, wear-resistant Al-based quasicrystalline coatings," *Sci. Technol. Adv. Mater.*, vol. 17, no. 1, pp. 71–79, 2016, doi: 10.1080/14686996.2016.1152563.

[46] F. J. Hermanek, "Wear-resistant Quasicrystalline Coating," US 6,254,699 B1, 2001.

[47] Y. Kang, C. Zhou, S. Gong, and H. Xu, "Corrosion of Al-Cu-Fe-Cr quasicrystalline coating," pp. 3355–3358, 2005, doi: 10.4028/www.scientific.net/MSF.475-479.3355.

[48] A. Vardelle *et al.*, "The 2016 Thermal Spray Roadmap," *J. Therm. Spray Technol.*, vol. 25, no. 8, pp. 1376–1440, 2016, doi: 10.1007/s11666-016-0473-x.

[49] B. Jodoin, "Cold spray nozzle mach number limitation," *J. Therm. Spray Technol.*, vol. 11, no. 4, pp. 496–507, 2002, doi: 10.1361/105996302770348628.

[50] G. Bérubé, M. Yandouzi, A. Zúñiga, L. Ajdelsztajn, J. Villafuerte, and B. Jodoin, "Phase stability of Al-5Fe-V-Si coatings produced by cold gas dynamic spray process using rapidly solidified feedstock materials," *J. Therm. Spray Technol.*, vol. 21, no. 2, pp. 240–254, 2012, doi: 10.1007/s11666-011-9716-z.

[51] T. J. Watson, A. Nardi, A. T. Ernst, I. Cernatescu, B. A. Bedard, and M. Aindow, "Cold spray deposition of an icosahedral-phase-strengthened aluminum alloy coating," *Surf. Coatings Technol.*, vol. 324, pp. 57–63, 2017, doi: 10.1016/j.surfcoat.2017.05.049.

[52] A. G. Kraj and E. L. Bibeau, "Phases of icing on wind turbine blades characterized by ice accumulation," *Renew. Energy*, vol. 35, no. 5, pp. 966–972, 2010, doi: 10.1016/j.renene.2009.09.013.

[53] K. Ip, L. Hartley, K. Solanki, and D. White, "Theoretical and Experimental Study of Scaling Methods for Rotor Blade Ice Accretion Testing," *Pennsylvania State*

Univ., vol. 128, no. 1415, pp. 34–40, 2015, doi: 10.13140/RG.2.1.2585.0485.

[54] R. J. Kind, M. G. Potapczuk, A. Feo, C. Golia, and A. D. Shah, "Experimental and computational simulation of in-flight icing phenomena," *Prog. Aerosp. Sci.*, vol. 34, no. 5–6, pp. 257–345, 1998, doi: 10.1016/S0376-0421(98)80001-8.

[55] Y. Han, J. Palacios, and S. Schmitz, "Scaled ice accretion experiments on a rotating wind turbine blade," *J. Wind Eng. Ind. Aerodyn.*, vol. 109, pp. 55–67, 2012, doi: 10.1016/j.jweia.2012.06.001.

[56] K. Li *et al.*, "Investigating the effects of solid surfaces on Ice nucleation," *Langmuir*, vol. 28, no. 29, pp. 10749–10754, 2012, doi: 10.1021/la3014915.

[57] H. Sojoudi, M. Wang, N. D. Boscher, G. H. McKinley, and K. K. Gleason, "Durable and scalable icephobic surfaces: Similarities and distinctions from superhydrophobic surfaces," *Soft Matter*, vol. 12, no. 7, pp. 1938–1963, 2016, doi: 10.1039/c5sm02295a.

[58] G. Barati, M. Aliofkhazraei, S. Khorsand, S. Sokhanvar, and A. Kaboli, "Science and Engineering of Superhydrophobic Surfaces : Review of Corrosion Resistance , Chemical and Mechanical Stability," *Arab. J. Chem.*, vol. 13, no. 1, pp. 1763–1802, 2020, doi: 10.1016/j.arabjc.2018.01.013.

[59] S. Laurén, "What is contact angle hysteresis?," *Biolin Scientific*, 2018. https://www.biolinscientific.com/blog/what-is-contact-angle-hysteresis (accessed May 27, 2021).

[60] I. A. Ryzhkin and V. F. Petrenko, "Physical mechanisms responsible for ice adhesion," *J. Phys. Chem. B*, vol. 101, no. 32, pp. 6267–6270, 1997, doi: 10.1021/jp9632145.

[61] L.-H. Lees, *Fundamentals of Adhesion*. Plenum Press, 1991.

[62] J. N. Israelachvili, *Van der Waals Forces between Particles and Surfaces*. 2011.

[63] Y. Maly *et al.*, "A survey of icephobic coatings and their potential use in a hybrid coating/active ice protection system for aerospace applications," *Nature*, vol. 15, no. May, pp. 443–447, 2013, doi: 10.1016/j.paerosci.2019.01.002.

[64] "Icing Gear."

[65] A. Gambo, G. Ozgur, and E. Sevkat, "Electrical resistance heating for deicing and snow melting applications : Experimental study," *Cold Reg. Sci. Technol.*, vol. 160, no. February, pp. 128–138, 2019, doi: 10.1016/j.coldregions.2019.02.004.

[66] O. Fakorede, Z. Feger, H. Ibrahim, A. Ilinca, J. Perron, and C. Masson, "Ice protection systems for wind turbines in cold climate : characteristics , comparisons and analysis," *Renew. Sustain. Energy Rev.*, vol. 65, pp. 662–675, 2016, doi: 10.1016/j.rser.2016.06.080.

[67] A. Lopera-Valle and A. McDonald, "Application of Flame-Sprayed Coatings as Heating Elements for Polymer-Based Composite Structures," vol. 24, no. October,

pp. 1289–1301, 2015, doi: 10.1007/s11666-015-0302-7.

[68] D. Tejero-martin, M. Rezvani, T. Hussain, and A. Mcdonald, *Beyond Traditional Coatings : A Review on Thermal-Sprayed Functional and Smart Coatings*, vol. 28, no. 4. Springer US, 2019.

[69] F. Robitaille, M. Yandouzi, S. Hind, and B. Jodoin, "Metallic coating of aerospace carbon / epoxy composites by the pulsed gas dynamic spraying process," *Surf. Coat. Technol.*, vol. 203, no. 19, pp. 2954–2960, 2009, doi: 10.1016/j.surfcoat.2009.03.011.

[70] V. Pommier-budinger, "Analysis of piezoelectric ice protection systems combined with ice - phobic coatings," vol. 6, pp. 1–12.

[71] L. Pawlowski, *The Science and Engineering of Thermal Spray Coatings: Second Edition*. 2008.

[72] M. Karimi, B. Jodoin, and G. Rankin, "Shock-wave-induced spraying: Modeling and physics of a new spray process," *J. Therm. Spray Technol.*, vol. 20, no. 4, pp. 866–881, 2011, doi: 10.1007/s11666-011-9622-4.

[73] P. L. Fauchais, J. V. R. Heberlein, and M. I. Boulos, *Thermal Spray Fundamentals: From Powder to Part*. 2014.

[74] V. Donadei, H. Koivuluoto, E. Sarlin, and P. Vuoristo, "Icephobic Behaviour and Thermal Stability of Flame-Sprayed Polyethylene Coating: The Effect of Process Parameters," *J. Therm. Spray Technol.*, vol. 29, no. 1–2, pp. 241–254, 2020, doi: 10.1007/s11666-019-00947-0.

[75] M. Wang, *Composite coatings for implants and tissue engineering scaffolds*. Woodhead Publishing Limited, 2004.

[76] A. Papyrin, V. Kosarev, S. Klinkov, V. M. Fomin, and A. Alkhimov, *Cold Spray Technology*. Elsevier, 2007.

[77] T. B. Bush, Z. Khalkhali, V. Champagne, D. P. Schmidt, and J. P. Rothstein, "Optimization of Cold Spray Deposition of High-Density Polyethylene Powders," *J. Therm. Spray Technol.*, vol. 26, no. 7, pp. 1548–1564, 2017, doi: 10.1007/s11666-017-0627-5.

[78] N. A. Yefimov, *Powders With Quasicrystalline Structure*, 2nd ed. Elsevier Ltd., 2019.

[79] P. J. Steinhardt, "Quasicrystals: A brief history of the impossible," *Rend. Lincei*, vol. 24, no. SUPPL.1, pp. 85–91, 2013, doi: 10.1007/s12210-012-0203-3.

[80] R. Li, Z. Li, Z. Dong, and K. A. Khor, "A Review of Transmission Electron Microscopy of Quasicrystals - How Are Atoms Arranged," *Crystals*, pp. 1–16, 2016, doi: 10.3390/cryst6090105.

[81] F. Samavat, M. H. Tavakoli, S. Habibi, B. Jaleh, and P. T. Ahmad, "Quasicrystals," *Open J. Phys. Chem.*, vol. 68, no. 2, pp. 7–14, 2012, doi:

10.4236/ojpc.2012.21002.

[82] Y. Zou *et al.*, "Superior room-temperature ductility of typically brittle quasicrystals at small sizes," *Nat. Commun.*, pp. 1–7, 2016, doi: 10.1038/ncomms12261.

[83] F. Turquier, V. D. Cojocaru, M. Stir, R. Nicula, and E. Burkel, "Synthesis of single-phase Al-Cu-Fe quasicrystals using high-energy ball-milling," *J. Non. Cryst. Solids*, vol. 353, no. 32–40, pp. 3417–3420, 2007, doi: 10.1016/j.jnoncrysol.2007.05.092.

[84] S. Q. Fan, G. J. Yang, C. J. Li, G. J. Liu, C. X. Li, and L. Z. Zhang, "Characterization of microstructure of nano-TiO2 coating deposited by vacuum cold spraying," *Proc. Int. Therm. Spray Conf.*, vol. 15, no. December, pp. 513–517, 2006, doi: 10.1361/105996306X146901.

[85] H. Hajipour, A. Abdollah-zadeh, H. Assadi, E. Taheri-Nassaj, and H. Jahed, "Effect of Feedstock Powder Morphology on Cold-Sprayed Titanium Dioxide Coatings," *J. Therm. Spray Technol.*, vol. 27, no. 8, pp. 1542–1550, 2018, doi: 10.1007/s11666-018-0782-3.

[86] G. J. Yang, C. J. Li, F. Han, W. Y. Li, and A. Ohmori, "Low temperature deposition and characterization of TiO 2 photocatalytic film through cold spray," *Appl. Surf. Sci.*, vol. 254, no. 13, pp. 3979–3982, 2008, doi: 10.1016/j.apsusc.2007.12.016.

[87] N. I. Omar, S. Selvami, M. Kaisho, M. Yamada, T. Yasui, and M. Fukumoto, "Deposition of titanium dioxide coating by the cold-spray process on annealed stainless steel substrate," *Coatings*, vol. 10, no. 10, pp. 1–13, Oct. 2020.

[88] A. Work and Y. Lian, "A critical review of the measurement of ice adhesion to solid substrates," *Prog. Aerosp. Sci.*, vol. 98, no. March, pp. 1–26, 2018, doi: 10.1016/j.paerosci.2018.03.001.

[89] C. Laforte and A. Beisswenger, "Icephobic Materials Centrifuge Adhesion Test," no. January 2005, 2018.

[90] K. Itagaki, "Mechanical Ice Release Processes - Self-shedding from high-speed rotors," *CRREL Rep.*, vol. XXX, p. 60, 1983.

[91] A. M. Palacios, J. L. Palacios, and L. Sánchez, "Eliciting a human understandable model of ice adhesion strength for rotor blade leading edge materials from uncertain experimental data," *Expert Syst. Appl.*, vol. 39, no. 11, pp. 10212–10225, 2012, doi: 10.1016/j.eswa.2012.02.155.

[92] M. Bleszynski and E. Clark, "Current Ice Adhesion Testing Methods and the Need for a Standard : A Concise Review," pp. 117–133, 2021.

[93] L. E. Raraty and D. Tabor, "The Adhesion and Strength Properties of Ice," in *Proceedings of the Royal Society A: Mathematical, Physical and Engineering Sciences*, 1957, vol. 245, no. 1241, pp. 184–201, [Online]. Available: http://www.jstor.org/stable/2414705.

[94] H. Assadi, F. Gärtner, T. Stoltenhoff, and H. Kreye, "Bonding mechanism in cold gas spraying," *Acta Mater.*, vol. 51, no. 15, pp. 4379–4394, 2003, doi: 10.1016/S1359-6454(03)00274-X.

[95] D. Tiab and E. C. Donaldson, "Wettability," in *Petrophysics*, 3rd ed., 2012, pp. 375–418.

[96] A. Moridi, S. M. Hassani-Gangaraj, M. Guagliano, and M. Dao, "Cold spray coating: Review of material systems and future perspectives," *Surf. Eng.*, vol. 30, no. 6, pp. 369–395, 2014, doi: 10.1179/1743294414Y.0000000270.

[97] H. Assadi, H. Kreye, F. Gärtner, and T. Klassen, "Cold spraying – A materials perspective," *Acta Mater.*, vol. 116, pp. 382–407, 2016, doi: 10.1016/j.actamat.2016.06.034.

[98] M. Winnicki, "Advanced functional metal-ceramic and ceramic coatings deposited by low-pressure cold spraying: A review," *Coatings*, vol. 11, no. 9, 2021, doi: 10.3390/coatings11091044.

[99] T. Schmidt, F. Gaertner, and H. Kreye, "New developments in cold spray based on higher gas and particle temperatures," *Proc. Int. Therm. Spray Conf.*, vol. 15, no. December, pp. 488–494, 2006, doi: 10.1361/105996306X147144.

[100] T. Schmidt, F. Gärtner, H. Assadi, and H. Kreye, "Development of a generalized parameter window for cold spray deposition," *Acta Mater.*, vol. 54, no. 3, pp. 729–742, Feb. 2006, doi: 10.1016/j.actamat.2005.10.005.

[101] R. Fernandez and B. Jodoin, "Cold Spray Aluminum–Alumina Cermet Coatings: Effect of Alumina Content," *J. Therm. Spray Technol.*, vol. 27, no. 4, pp. 603–623, 2018, doi: 10.1007/s11666-018-0702-6.

[102] R. Fernandez and B. Jodoin, "Effect of Particle Morphology on Cold Spray Deposition of Chromium Carbide-Nickel Chromium Cermet Powders," *J. Therm. Spray Technol.*, vol. 26, no. 6, pp. 1356–1380, 2017, doi: 10.1007/s11666-017-0580-3.

[103] M. Yandouzi, L. Ajdelsztajn, and B. Jodoin, "WC-based composite coatings prepared by the pulsed gas dynamic spraying process: Effect of the feedstock powders," *Surf. Coatings Technol.*, vol. 202, no. 16, pp. 3866–3877, 2008, doi: 10.1016/j.surfcoat.2008.01.036.

[104] R. Fernandez and B. Jodoin, "Cold Spray Aluminum–Alumina Cermet Coatings: Effect of Alumina Morphology," *J. Therm. Spray Technol.*, vol. 28, no. 4, pp. 737–755, 2019, doi: 10.1007/s11666-019-00845-5.

[105] J. M. Shockley, S. Descartes, P. Vo, E. Irissou, and R. R. Chromik, "The influence of Al2O3 particle morphology on the coating formation and dry sliding wear behavior of cold sprayed Al-Al2O3 composites Surface & Coatings Technology The in fl uence of Al 2 O 3 particle morphology on the coating formation and dry sliding we," no. January, 2015, doi: 10.1016/j.surfcoat.2015.01.057.

[106] E. Irissou, J. Legoux, B. Arsenault, and C. Moreau, "Investigation of Al-Al 2 O 3

Cold Spray Coating Formation and Properties," vol. 16, no. December, pp. 661–668, 2007, doi: 10.1007/s11666-007-9086-8.

[107] A. Shkodkin, A. Kashirin, O. Klyuev, and T. Buzdygar, "Metal Particle Stimulation by Surface Abrasive Treatment in Gas Dynamic Spraying," *J. Therm. Spray Technol.*, vol. 15, no. September, pp. 382–386, 2006, doi: 10.1361/105996306X124383.

Appendix – A

The Arduino code used to compute the angular velocity and vibrations produced during the ice adhesion tests:

```
float value=0;
//float rev=0;
//float rpm;
float oldtime=0;
float time;
float timestamp=0;

float const vibspin = A1;
float vibsval;
float vibsfrequency;

float const voltagepin = A2;
float voltageval;
float rpmvolts;
float motorRPM;
float realRPM;

void isr()          //interrupt service routine
{
//rev++;
}

void setup()
{

Serial.begin(57600);
  digitalWrite(2 ,HIGH);// Instead of using a pull up resistor
  attachInterrupt(0,isr,RISING);  //attaching the interrupt

}

void loop()
{
  delay(50);// 0.05 second delay
  detachInterrupt(0);           //detaches the interrupt while calculating
  time=millis()-oldtime;        //finds the time
  //rpm=(rev/time)*60000;         //calculates rpm
  oldtime=millis();             //saves the current time
  //rev=0;
  timestamp = timestamp + 0.05;  // This should solve the time stamp issue, if not chnage back to 1


  vibsval = analogRead(vibspin);
  vibsfrequency = map(vibsval, 205, 1023, 10, 1000);

  voltageval = analogRead(voltagepin);
  motorRPM = map(voltageval, 0, 1023, 0, 3425);
  realRPM = motorRPM*2.0;


 attachInterrupt(0,isr,RISING);
 Serial.print(timestamp);
 Serial.print(",");
 //Serial.print(rpm);
 //Serial.print(",");
 Serial.print(realRPM);
 Serial.print(",");
 Serial.print(vibsfrequency);
 Serial.print(",");
 Serial.println();
```

Appendix – B

The calculations of ice adhesion strength obtained with the Centrifuge Adhesion Test (CAT) did not include the tangential component of the rotation. This method of obtaining the ice adhesion strength of a surface, as seen in the literature, does not typically include tangential components and therefore was not included in this work. The following is a sample calculation of the tangential component added to the ice adhesion strength for an aluminum sample tested in the CAT:

The equation for the tangential ice adhesion strength component, as seen by the ice cube, is the following

$$\tau_{s,t} = \frac{\alpha * r * m}{A}$$

where $\tau_{s,t}$ is the tangential ice adhesion strength (kPa), α is the angular acceleration of the rotor (rad/s), r is the rotor's radius (m), m is the ice cube's mass (kg), and A is the ice cube's area attached to the rotor (m^2).

For a ramp up time of 45 seconds from 0 rad/s to the rotor's maximum rotations of 717 rad/s, the angular acceleration for the rotor is 16 rad/s^2.

Using the same data (seen in section 5.1) for the ice cube's weight, rotor's radius, and ice cube area, the tangential ice adhesion strength is 25 kPa.

For an aluminum sample that had an ice releasing rotational velocity of 370 rad/s, it's radial ice adhesion strength (calculated with the equations presented in section 5.1) is 212 kPa.

From the added 25 kPa, exerted by the tangential component, it accounts for approximately 10% of the total ice adhesion strength. However, the calculation of the tangential component does not include any variable that changes from one test to another and is entirely comprised of constants. As a result, 25 kPa would be added to every result obtained in the CAT. For this reason, it is not worth including the tangential component to the results as the ice adhesion strength data is only being compared with itself by using the adhesion reduction factor (ARF) and not with any other value from the literature. If ice adhesion strength values were to be compared to other ice adhesion strength values, then it would

be necessary to include the tangential component, however for the purposes of this study it was not.